The University of Nottingham
UNITED KINGDOM · CHINA · MALAYSIA

Sumair, Faisal Ahmed (2018) Preparation and characterisation of eutectic nanofluids for heat transfer enhancement in flat plate solar collectors. PhD thesis, University of Nottingham.

Access from the University of Nottingham repository:
http://eprints.nottingham.ac.uk/48390/1/PREPARATION%20AND%20CHARACTERISATION%20OF%20EUTECTIC%20NANOFLUIDS%20FOR%20HEAT%20TRANSFER%20ENHANCEMENT%20IN%20FLAT%20PLATE%20SOLAR%20COLLECTORS.pdf

Copyright and reuse:

The Nottingham ePrints service makes this work by researchers of the University of Nottingham available open access under the following conditions.

This article is made available under the University of Nottingham End User licence and may be reused according to the conditions of the licence. For more details see: http://eprints.nottingham.ac.uk/end_user_agreement.pdf

For more information, please contact eprints@nottingham.ac.uk

PREPARATION AND CHARACTERISATION OF EUTECTIC NANOFLUIDS FOR HEAT TRANSFER ENHANCEMENT IN FLAT PLATE SOLAR COLLECTORS

SUMAIR FAISAL AHMED, **B.Tech. M.Tech.**

Thesis submitted to the University of Nottingham

for the degree of Doctor of Philosophy

JUNE 2017

DEDICATION

To my beloved parents
Mumtaz Begum and Mohd. Shameem Ahmed

My beloved parent-in-law
Abdul Subur Rizwan and Mateen Farooqi

My beloved wife
Amtul Safoora Farooqui

My beloved daughter
Iqra Anabiya Faisal

My beloved son

Abdul Qawi Faisal

Abstract

Use of thermal energy storage (TES) materials in solar collectors is known to be the most effective way of storing thermal energy. The most conventional and traditional heat storage element is water. However, due to low thermal conductivity (TC) in vapor state its applications as a heat storage medium are limited. An alternative option is to utilize organic and inorganic TES materials as they both operate at low and medium temperature ranges. Organic TES materials such as paraffins are non-corrosive and possess high latent heat capacity. On the contrary, inorganic TES materials possess high density and appreciable specific heat capacity (SHC). Due to rapid progress and advancement in nanotechnology, varieties of nanomaterials were dispersed in various base fluid(s) to enhance thermo-physical properties. Here the current status and future development trends of TES materials has been presented. Furthermore, an extensive research on enhancement of TC and SHC of various TES material doped with nanomaterials has been discussed.

Enhancement in heat capacity (HC) and thermal conductivity (TC) with dispersion of graphene (GE) nanoparticles in low temperature molten salt was investigated. Three different nanoparticle concentrations (0.01, 0.05 and 0.1 wt. %) were dispersed in molten salt composed of 5.76% $NaNO_3$, 21.36% KNO_3, 24.84% $Ca(NO_3)_2$, 41.08% $CsNO_3$ and $LiNO_3$ 7.44% by weight. Doping of GE resulted in enhanced HC ranging from 5-13%, whereas, TC showed enhancement up to 2.44%, with respect to GE

concentration. Various theoretical models were tested to predict TC and HC of GE doped molten salt. Maxwell and Hamilton-Crosser TC models show good agreement with experimental results with deviation of ±3% while Nan's TC model over predicted TC value. Conventional HC equation fits well with the experimental data with deviation <14%. Thus, the results obtained show the potential of GE doped molten salt as thermal energy storage (TES) medium in various heat transfer applications.

This work also investigates the rheological and corrosion properties of graphene (GE) dispersed in eutectic salts. It was observed that doping of GE has significantly enhanced the viscosity of base salt. This enhancement in GE dispersed eutectic salt is mainly due to the presence of solid GE sheets and its coagulation in eutectic salts. Various concentrations of GE and temperature ranges were studied here. Eutectic salt dispersed GE behaved as non-Newtonian fluid at 70, 80 and 90 ^{o}C except at 200 ^{o}C, where it behaved as a Newtonian fluid. Viscosity of nanosuspension was predicted using Einstein's equation. Furthermore, corrosion studies using ASTM D130 method were performed to analyse the effects of base fluid on copper and stainless steel (SS304) at elevated temperatures. Fourier transform infrared spectrometer (FTIR) result shows that the presence of all nitrate bonds in synthesized base salt and GE dispersed base salt. X-ray diffraction depicts that the doping of GE in eutectic salt does not alter the crystal structure of nitrate molecules. EDX results confirm that both Cu and SS304 material were corroded. SS304

exhibited constant corrosion with an increase in GE concentration dispersed in eutectic salt, whereas copper exhibited an increase in corrosion rate with an increase in GE concentration.

Kinetic studies have been carried out for molten salt and GE dispersed molten salt. It was concluded that dispersion of GE has not altered decomposition rate of nitrate of ions.

In application, we have fabricated and tested two types of solar collectors, i.e., solar thermal collector and photo-voltaic/thermal collector for TES material. Test was carried out to confirm the thermal performance of both solar collectors under water, base salt and GE dispersed base salt as TES. Results proved that in both types of solar collectors, all three concentrations of GE (0.01, 0.05 and 0.1 wt. %) dispersed base salt were having high thermal performance than water and base salt. Thus, it was concluded that GE dispersed molten salt can be successfully used as TES material in both solar collectors.

List of Publications

- **Ahmed SF**, Khalid M, Rashmi W, Chan A, Shahbaz K. "*Recent progress in solar thermal energy storage using nanomaterials"*. **Renewable and Sustainable Energy Reviews**. 2017;67:450-60.

- **SF Ahmed**, M Khalid, W Rashmi, A Chan, *"Investigation of rheological and corrosion properties of molten salt as thermal energy storage for solar thermal collectors"***, Journal of Materials Science,** 53 (2018) 692-707.

- **SF Ahmed**, M Khalid, W Rashmi, A Chan, *"Progress in solar water heaters and thermal collectors: A review"***,** (accepted) **Renewable and Sustainable Energy Reviews,** 2017.

UNDER REVIEW PAPERS:

- **SF Ahmed**, M Khalid, W Rashmi, A Chan, *"Enhanced thermal properties of low temperature molten salt doped graphene for thermal energy storage",* under review in **International Journal of Thermal Sciences,** 2016.

CONFERENCE AND WORKSHOP ATTENDED:

- **SF Ahmed,** M Khalid, W Rashmi, A Chan, "Enhanced thermal properties of molten salt doped graphene for thermal energy storage", on proceedings of **Energy System Conference 2016,** London, U.K.

ACKNOWLEDGEMENTS

From the beginning to the outset, I am grateful to one God, for his supreme mercy, guidance and grace for accomplishment of this course work. I am also thankful to Prophet Muhammad (Peace be upon him) for his teachings and guidance, which helped in this course work.

With this acknowledgment, I express my gratitude to all those people who have supported & helped me in this dissertation and made for me a worth full experience.

I would like to thank my beloved parents, for their moral support, encouragement and prayer in every day of life.

It's gives immense pleasure to express my sincere gratitude to my supervisor Dr. Mohammad Khalid Siddiqui, for his inspiring encouragement, guidance and constant support throughout the course, which made my work into huge focus of light.

I extend my thanks to Prof. Andy Chan, Dr. Ianatul Khoiroh, Dr. Rashmi Gangasa Walvekar and Prof. Nowshad Amin for their valuable suggestions, unpayable guidance and keen attention for successful accomplishment of my work and dissertation.

I reverently thanks to all technical staff especially to Mr. Ahmad Fareez Mohd Rawi, Ms. Filzah Mohd Fauzi, Ms. Noor Fatihah Suhaime, Ms. Khairani Hasuna, Mr. Siak Chung Wong and Mr. Elyas Rahmat for their

assistance in TGA, DSC, SEM, XRD and thermal conductivity characterization of samples.

I express my thanks to Dr. Abdul Khaliq, Dr. Reza Ketabchi, Dr. Suganti Ramarad, Mr. Anand Bellam, Mr. Ousama and Priyanka Jagadish for their advices, guidance and assistance in every situation.

I wish to express thanks to University of Nottingham for providing a platform to accomplish doctorate degree. I extend my thanks to TA instruments and Perkin Elmer for helping me in carrying out characterization facilities in their laboratories.

Finally, thanks to my wife for her love, patience, encouragement and prayers. I would also wish to thank my brothers and sisters for their constant prayer and moral support. I am very much delightful to have Ms. Iqra Anabiya in this tenure. I am also thankful to my mother-in-law and father-in-law for their constant support and prayers. I extend my thanks to brothers-in-law, sisters-in-law, relatives and friends.

Table of Contents

Abstract ii

List of Publications v

ACKNOWLEDGEMENTS vi

List of Tables xv

List of Figures xvi

Abbreviations xxi

1 INTRODUCTION 1

1.1 Technologies for extracting solar energy 3

1.2 Objectives 10

1.3 Organization of thesis 11

1.4 Findings 12

2 LITERATURE REVIEW 14

2.1 Introduction 15

2.2 Types of Solar Water Heating (SWH) system 15

2.2.1 Active SWH system 16

2.2.2 Passive SWH system 21

2.3 Flat plate collectors 31

2.3.1 Enhancement through design and simulation 32

2.4 Evacuated Tube Collectors 35

2.4.1 Enhancement through design and simulation 35

2.5 Concentrating Collectors 37

2.5.1 Compound Parabolic Collectors (CPC) 37

2.5.2 Parabolic Trough Collectors (PTC) 39

2.5.3 Central receiver system 42

2.6 Thermal energy storage materials 46

2.6.1 Sensible heat storage 46

2.6.2 Chemical heat storage 55

2.6.3 Latent Heat Storage 56

2.7 Theoretical Models for estimating various parameters 66

2.8 Overview of Corrosion property 68

2.9 Summary 69

2.10 Conclusion 70

3 EXPERIMENTAL PROCEDURE 73

3.1 Introduction 74

3.2 Materials 74

4 CHARACTERIZATION TECHNIQUES 80

4.1 Introduction 81

4.2 Differential Scanning Calorimeter (DSC) 81

4.3 Differential Thermogravimetric Analysis (DTGA) 82

4.4 Field Emission Scanning Electron Microscope (FESEM) 83

4.5 Thermal Conductivity.....84

4.6 Hybrid Rheometer 85

4.7 Fourier Transform Infrared (FTIR) 87

4.8 X-ray Diffraction (XRD).....88

4.9 Corrosion test.....89

5 RESULT AND DISCUSSION 90

5.1 Introduction 91

5.2 Graphene.....91

5.3 Differential Scanning Calorimetery.....93

5.3.1 Dispersion of different concentration of GE in molten salt.....94

5.3.2 Dispersion of GE oxide in selected molten salt 95

5.3.3 Dispersion of Aluminum oxide NP in molten salt.....96

5.3.4 Dispersion of multi-walled carbon nanotube in molten salt 97

5.3.5 Theoretical Analysis of HC 98

5.4 Field Emission Scanning Electron Microscope (FESEM) 100

5.4.1 Energy Dispersive X-ray (*EDX*) Analysis 101

5.5 Thermogravimetric Analysis (TGA) 104

5.6 Differential Thermogravimetric Analysis (DTGA).....105

5.7 Thermal Conductivity.....106

5.7.1 Maxwell and Hamilton-Crosser models 107

5.7.2 Nan Model of TC 108

5.8 Viscosity 110

5.8.1 Predicting of viscosity using Einstein model 114

5.9 Fourier Transform Infrared (FTIR) 116

5.10 X-Ray Diffraction (XRD) 117

5.11 Corrosion Analysis 118

5.11.1 Copper 118

5.11.2 SS304 120

5.11.3 SEM analysis on corrosion of copper 121

5.11.4 SEM analysis of Stainless steel 123

5.11.5 EDX analysis of copper 125

5.11.6 EDX analysis of SS304 127

5.11.7 XRD analysis of Copper and SS304 130

5.11.8 High temperature corrosion test 132

5.11.9 EDX analysis of copper 136

5.12 Kinetic studies 145

5.12.1 Decomposition analysis of molten salt and GE dispersed molten salt. 150

6 APPLICATION 152

6.1 Introduction 153

6.2 Fabricating of prototype for TES application.....153

6.3 Daily operating 156

7 CONCLUSIONS.....162

7.1 Introduction 163

7.2 Principal findings.....164

7.3 Limitations……..167

7.4 Challenges……...168

References…….…….169

List of Tables

Table 1-1: Description of various solar thermal collectors. Data compiled from [3, 21, 22, 28] 8

Table 2-1: Recent studies on SWH systems [8, 71] 30

Table 2-2 Molten salts and high temperature oils [118, 119]. 47

Table 2-3 Nanomaterials doped in base fluids for TC enhancement [145]. 53

Table 2-4 Solid-state sensible heat storage materials [118] 55

Table 2-5: List of Standard eutectic behavior HTF [117] 59

Table 2-6: Recently developed eutectic mixture salts with low melting point 61

Table 2-7: Nanomaterials doped in eutectic salts[145] 65

Table 3-1: Mass composition of nitrate salts 77

Table 5-1: Enhanced HC values with various concentrations of GE in base molten salts 93

Table 5-2: List of variables used in Maxwell and Hamilton-Crosser model 108

Table 5-3: Enhanced viscosity values with various concentrations of GE in base molten salts 111

Table 5-4 Error deviation of Einstein's model of viscosity at various temperatures 115

Table 5-5: FTIR frequency assignments 116

Table 5-6: Literature peak of XRD 117

List of Figures

Figure 1-1: Global energy consumption in 2013 [1]. 3

Figure 1-2: SWH systems in top 11 countries from 2005-2015 [6]. 5

Figure 2-1: Schematic diagram of indirect circulation system [35]. 18

Figure 2-2: Schematic diagram of DXSAHP system [44]. 20

Figure 2-3: Schematic diagram of ICS (1) storage tank, (2) heat exchanger, (3) pump, (4) flow sensors, (5) water inlet and (6) water outlet [49]. 22

Figure 2-4: ICS system integrated with 9 fins inside paraffin wax [58]. 25

Figure 2-5: Schematic diagram of thermosyphon systems [61]. 27

Figure 2-6: Flat plate collector (FPC). 32

Figure 2-7: Three different solar collectors. (a) Copper sheet with selective coating and copper tubes. (b) Aluminum sheet with selective coating and aluminum tubes. (c) Aluminum roll-bond with semi-selective coating [82]. 34

Figure 2-8: Optical path of lens walled CPC with air gap [20]. 38

Figure 2-9: Two CPC collectors: (a) 3.06 and (b) 6.03 concentrator ratios. 39

Figure 2-10: Parabolic trough collector. 40

Figure 2-11: Schematic diagram of cavity absorber and concentrator model [95]. 41

Figure 2-12: Central Recevier system. 43

Figure 2-13: Heat pipes in CRS: (a) receiver panel, (b) 2-D receiver panel; (c) basic structure; (d) receiver of CRS [109]. 45

Figure 2-14: Classification of latent heat materials, with phase change solid-liquid [117, 118]. 47

Figure 2-15: TC enhancement as a function of temperature [137]. 51

Figure 2-16: Photograph of Al_2O_3 nanofluid (a) with triton X-100 surfactant and (b) without triton X-100 surfactant [139]. 51

Figure 2-17: Phase change profile of PCM [165]. 57

Figure 2-18: Heat capacity of HITEC salt with different concentration of Sn/SiO_2 NPs [186]. 63

Figure 2-19: SEM image of pure eutectic salt with 60nm SiO_2 NP [189].. 65

Figure 3-1: Flowchart of research activities 76

Figure 3-2: Flow chart for synthesis of low melting point salt doped GE, f-GE, SWCNT, Al_2O_3 NP, Cu NP, MWCNT and fullerene. 78

Figure 3-3: photograph of synthesized base salt along with dispersion of GE concentrations 79

Figure 4-1: DSC of TA instrument……..82

Figure 4-2: Photograph of DTGA of Mettler Toledo……..83

Figure 4-3: FESEM of FEI instrument……..…..84

Figure 4-4: Thermal conductivity setup…….…..……85

Figure 4-5: Rheology measurements using discovery hybrid of TA instrument……..…..86

Figure 4-6: Schematic diagram of hybrid rheometer (a) without sample and (b) with sample. ……..87

Figure 4-5: FTIR instrument of Perkin Elmer…….88

Figure 4-6: X-ray Diffractometer of Bruker……....89

Figure 5-1: (a), (b) and (c): SEM image of multilayered graphene 60nm sheets 92

Figure 5-2: XRD graph of graphene 60nm sheet. 92

Figure 5-3: HC of base salt and mixed with different concentrations of GE94

Figure 5-4: DSC characterization of pure salt and doped with different concentration of GE. 95

Figure 5-5: DSC characterization of pure salt and doped with different concentration of GE oxide. 96

Figure 5-6: DSC characterization of pure salt and doped with various concentrations of Al_2O_3 NP. 97

Figure 5-7: DSC characterization of base salt and doped with various concentrations of MWCNT..... 98

Figure 5-8: Comparison of theoretical and experimental HC with three concentrations of GE (0.01, 0.05 and 0.1 wt. %)..... 99

Figure 5-9: (a), (c), (e), (g) are SEM and (b), (d), (f) and (h) are BSE images of base salt, 0.01 wt. %, 0.05 wt. % and 0.1 wt. % doped, GE respectively. 101

Figure 5-10: (a), (c), (e) and (g) are SEM images, where EDX pattern had scanned. (b), (d), (f) and (h) are EDX pattern of base salt and with different concentrations of GE. 103

Figure 5-11: Normalized TGA curve of pure salt with different concentrations of GE..... 104

Figure 5-12: DTA curve of base salt with different concentrations of GE.105

Figure 5-13: TC of base molten salt with different concentration of GE (0.01, 0.05 and 0.1 wt. %). 106

Figure 5-14: Comparison of experimental TC results with Maxwell and Hamilton-Crosser model with respect to GE concentration at room temperature. 108

Figure 5-15: Comparison of experimental results with Nan's model prediction for 0.01, 0.05 and 0.1 wt. % of GE concentrations at room temperature. 109

Figure 5-16: (a) Viscosity vs Shear rate and Stress vs Shear rate of base salt along with three different concentrations of GE at 70 ^{o}C, (c) & (d) Viscosity vs Shear rate and Stress vs Shear rate of base salt along with three different concentrations of GE at 80 ^{o}C, (e) & (f) Viscosity vs Shear rate and Stress vs Shear rate of base salt along with three different concentrations of GE at 90 ^{o}C and (g) & (h) Viscosity vs Shear rate and Stress vs Shear rate of base salt along with three different concentrations of GE at 200 ^{o}C. 114

Figure 5-17: Comparison of experimental results at various temperatures with Einstein model. Comparison at (a) 70, (b) 80, (c) 90 and (d) 200 ^{o}C.115

Figure 5-18: FTIR spectrum of base salt and GE dispersed base salt. 117

Figure 5-19: XRD graph of base salt and GE dispersed base salt. 118

Figure 5-20: Copper strips before and after the corrosion test; (a) polished copper strip before the corrosion, (b), (c), (d) and (e) copper strip after the corrosion test in base salt, molten salt dispersed 0.01 wt. % GE, molten salt dispersed 0.05 wt. % GE and 0.1 wt. % GE, respectively. 119

Figure 5-21: ASTM copper strip corrosion standards [228]..... 119

Figure 5-22: SS304 strips before and after the corrosion test; (a) polished copper strip, (b), (c), (d) and (e) SS304 strip after corrosion test in base salt, molten salt dispersed 0.01, 0.05 and 0.1 wt. %, respectively. 121

Figure 5-23: Shows SEM analysis of corrosion test on copper strip. Figure 5-23 (a) is morphology of bare copper strip and (b), (c), (d) and (e) are SEM images of copper strips after corrosion test in base salt, molten salt dispersed 0.01, 0.05 and 0.1 wt. %, respectively. 123

Figure 5-24: shows SEM analysis of corrosion test on SS304 strip. Figure 5-24 (a) is morphology of bare SS304 strip and (b), (c), (d) and (e) are SEM images of SS304 strips after corrosion test in base salt, molten salt dispersed 0.01, 0.05 and 0.1 wt. %, respectively. 124

Figure 5-25: (a), (c), (e), (g) and (i) are SEM images, where EDX pattern had scanned. (b), (d) (f) (h) and (j) are EDX pattern of copper strip. (a), (b) are SEM and EDX of bare copper strip. (c), (e), (g) and (i) are SEM images and (b), (d), (f), (h) and (j) are EDX pattern of copper strips after corrosion test with base salt, base salt dispersed with 0.01, 0.05 and 0.1 wt. % GE concentration. 127

Figure 5-26: (a), (c), (e), (g) and (i) are SEM images, where EDX pattern had scanned. (b), (d) (f) (h) and (j) are EDX pattern of SS304 strip. (a), (b) are SEM and EDX of bare SS304 strip. (c), (e), (g) and (i) are SEM images of copper strips after corrosion test with base salt, base salt dispersed with 0.01, 0.05 and 0.1 wt. % GE concentration and (d), (f), (h) and (j) are EDX pattern, respectively. 129

Figure 5-27: shows low temperature corrosion test on copper strip. Cu standard is XRD of bare copper strip and remaining XRD patterns are of Cu strips after corrosion test in base salt, base salt dispersed in 0.01, 0.05 and 0.1 wt. %, respectively. 131

Figure 5-28: shows low temperature corrosion test on SS304 strip. SS standard is XRD of bare SS304 strip and remaining XRD patterns are of SS strips after corrosion test in base salt, base salt dispersed in 0.01, 0.05 and 0.1 wt. %, respectively. 132

Figure 5-29: Snapshot of copper strips after corrosion test; (a), (b), (c) and (d) are copper strips after high temperature corrosion test in base salt, eutectic salt dispersed 0.01, 0.05 and 0.1 wt. % GE, respectively..... 133

Figure 5-30: Snapshot of SS304 strips after corrosion test; (a), (b), (c) and (d) are copper strips after high temperature corrosion test in base salt, eutectic salt dispersed 0.01, 0.05 and 0.1 wt. % GE, respectively..... 134

Figure 5-31: shows SEM analysis of corrosion test on copper strip. Figure 5-31 (a) is morphology of bare copper strip and (b), (c), (d) and (e) are SEM images of copper strips after corrosion test in base salt, eutectic salt dispersed 0.01, 0.05 and 0.1 wt. %, respectively. 135

Figure 5-32: (a), (c), (e), (g) and (i) are SEM images, where EDX pattern had scanned. (b), (d) (f) (h) and (j) are EDX pattern of copper strip. (a), (b) are SEM and EDX of bare copper strip. (c), (e), (g) and (i) are SEM images of copper strips after corrosion test with base salt, base salt dispersed with 0.01, 0.05 and 0.1 wt. % GE concentration and (d), (f), (h) and (j) are EDX pattern, respectively. 138

Figure 5-33: shows high temperature corrosion test on copper strip. Cu standard is XRD of bare copper strip and remaining XRD patterns are of Cu strips after corrosion test in base salt, base salt dispersed in 0.01, 0.05 and 0.1 wt. %, respectively. 140

Figure 5-34: shows SEM analysis of corrosion test on SS304 strip. (a) is morphology of bare SS304 strip and (b), (c), (d) and (e) are SEM images of SS304 strips after corrosion test in base salt, eutectic salt dispersed 0.01, 0.05 and 0.1 wt. %, respectively. 141

Figure 5-35: (a), (c), (e), (g) and (i) are SEM images, where EDX pattern had scanned. (b), (d) (f) (h) and (j) are EDX pattern of SS304 strip. (a), (b) are SEM and EDX of bare SS304 strip. (c), (e), (g) and (i) are SEM images of copper strips after corrosion test with base salt, base salt dispersed with 0.01, 0.05 and 0.1 wt. % GE concentration and (d), (f), (h) and (j) are EDX pattern, respectively. 144

Figure 5-36: shows high temperature corrosion test on SS304 strip. SS standard is XRD of bare SS304 strip and remaining XRD patterns are of SS strips after corrosion test in base salt, base salt dispersed in 0.01, 0.05 and 0.1 wt. %, respectively. 145

Figure 5-37: Activation energy calculation for of base salt at three different heating rates i.e., 5, 10, 15 ^{o}C..... 147

Figure 5-38: Activation energy calculation for 0.01 wt. % GE dispersed in base salt at three different heating rates i.e., 5, 10, 15 ^{o}C. 148

Figure 5-39: Activation energy calculation for 0.05 wt. % GE dispersed in base salt at three different heating rates i.e., 5, 10, 15 ^{o}C. 149

Figure 5-40: Activation energy calculation for 0.1 wt. % GE dispersed in base salt at three different heating rates i.e., 5, 10, 15 ^{o}C. 150

Figure 6-1: Manufacturing of solar thermal collector using Cu sheets and tubes 153

Figure 6-2: Manufacturing of solar thermal collector using stainless steel 304..... 154

Figure 6-3: Snapshot of PV/thermal and thermal collector. 155

Figure 6-4: Rare view of PV/thermal and thermal collector..... 155

Figure 6-5: Solar thermal collector after black coating 156

Figure 6-6: Variation of water temperature in thermal and PV/thermal collector..... 157

Figure 6-7: Variation of base fluid temperature in thermal and PV/Thermal collector..... 158

Figure 6-8: Temperature variation of base salt + 0.01 wt. % GE in thermal and PV/Thermal collector 159

Figure 6-9: Variation of base salt + 0.05 wt. % GE in thermal and PV/Thermal Collector 160

Figure 6-10: Variation of base salt + 0.1 wt. % GE in thermal and PV/Thermal collector 161

Abbreviations

TES	Thermal Energy Storage
SWH	Solar Water Heating
PCM	Phase Change Material
DXSAHP	Direct Expansion Solar Assisted Heat Pump
HTF	Heat Transfer Fluid
PV	Photo-Voltaic
PV/T	Photo-Voltaic / Thermal
EG	Ethylene Glycol
NP	Nano Particle
CPSC	Concentrating Parabolic Solar Collector
CNT	Carbon Nano Tube
MWCNT	Multi Walled Carbon Nano Tube
f-MWCNT	Functionalized Multi Walled Carbon Nano Tube
SWCNH	Single Walled Carbon Nano Horn
ExG	Expanded Graphite
FPC	Flat Plate Collector
TG	Thermo Gravimetric
COP	Coefficient of Performance
CRS	Central Receiver System
DSC	Differential Scanning Calorimetry
TC	Thermal Conductivity
SHC	Specific Heat Capacity
LHS	Latent heat storage
HX	Heat Exchanger
HTF	Heat Transfer Fluid
ETC	Evacuated Tube Collector
DX-SAHPWH	Direct Expansion Solar Assisted Heat Pump Water heater
CPC	Compound Parabolic Collector
ICS	Integral Collector Storage
PTC	Parabolic Trough Collector
FPSC	Flat Plate Solar Collector
FESEM	Field Emission Scanning Electron Microscope
DTGA	Differential Thermogravimetric Analysis
EDAX	Energy Dispersive X-ray Analysis
ETFE	Ethylene Tetra Fluro Ethylene
CFD	Computational Fluid Dynamics
FEM	Finite Element Method
TE	Thermal Efficiency

CHAPTER – 1

INTRODUCTION

Utilisation of energy has a key role in the development of the human society. Among other energy sources, electricity is a vital part of maintaining a successful society, and has been a concept, which has catalyzed the evolution of society on many levels. According to U.S. energy consumption 2016, global electrical energy needs continues to grow and about 90% of energy production is through fossil fuels as shown in Figure 1-1 [1]. Renewable energies such as wind, solar, biofuels and geothermal etc. accounts for 10% of global energy needs. In order to preserve natural resources and environment, one-third of the world's energy by 2050 will need to come from solar, wind, and other renewable resources.

Therefore, developments in the renewable energy has attracted attention of many researchers, with a view to find an alternative form of sustainable energy [2]. Renewable resources are widely available, environmentally friendly and cause little or almost no pollution. However, the biggest challenge of using renewable resources is that it depends on atmospheric conditions, geographical location, economics and safety considerations [3].

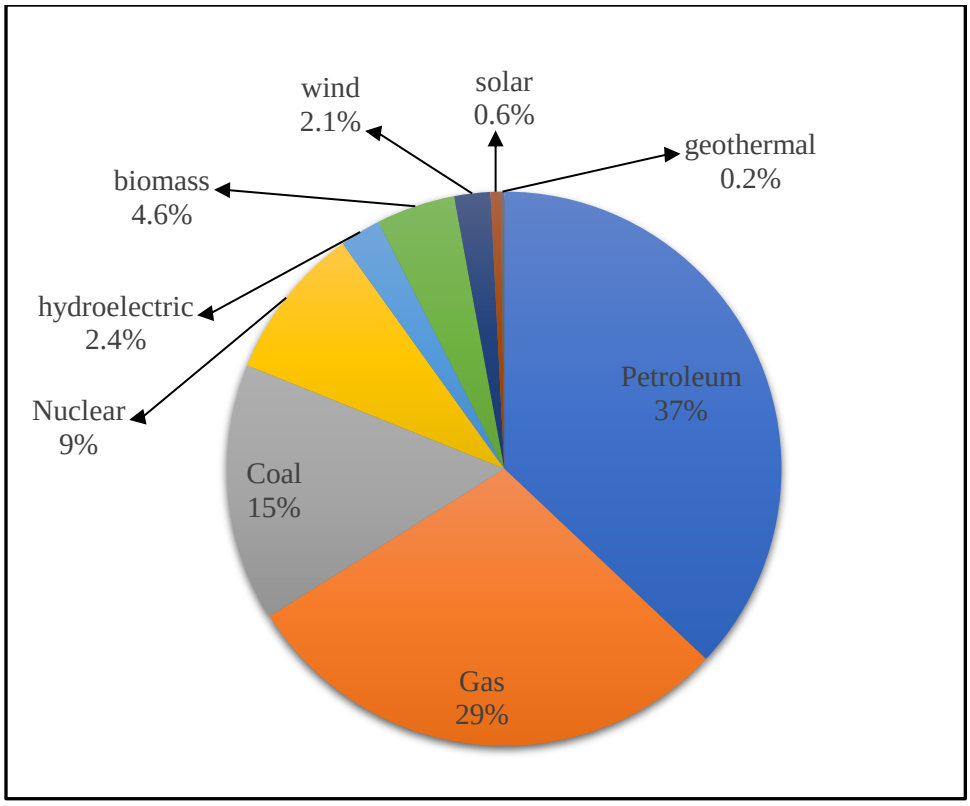

Figure 1-1: Global energy consumption in 2016 [1].

1.1 Technologies for extracting solar energy

One of the efficient ways to utilize solar energy is to make use of solar collectors. Solar collectors convert solar energy into internal heat energy of the system or of fluid. There are three types of solar collector technologies: i) photo-voltaic (PV) collector, ii) solar thermal collector and iii) photo-voltaic / thermal (PV/T) collector [4]. PV collector converts solar radiation into electricity by using semiconductor materials such as Si, SiO2, GaAs and CuS etc. The electrical energy produce by PV collector can be used for variety of applications. PV/T collector is a hybrid of PV and thermal collector. It will gain heat of solar radiation and convert

into electricity and thermal energy (using materials such as Al, Cu and polyethylene napthalate).

For solar thermal collector, solar energy is transferred as heat energy to working fluids such as water and ethylene glycol (EG) etc. [5]. Solar thermal collectors are significantly improving in terms of industrial and domestic applications. Solar water heating (SWH) system is one of the best examples for thermal collectors and its application. Figure 1-2 shows SWH system usage in top 11 countries with rest of the world [6]. According to renewable energy policy report 2016, the data was collected between years 2005 to 2014, since the beginning China is leading in SWH technology. Only Turkey and India are the largest SWH technology users excluding China in Asia. SWH system has matured over the years after years of innovation. A detailed study on different designs of SWH has been described elsewhere [7, 8]. A reduced cost of SWH will be helpful for the society [9].

Generally, water is being used as thermal storage element in SWH systems for household applications. However, the main drawbacks of water are low operating temperature, small duration of TES and optimum thermal conductivity (TC). Research has been carried out to enhance the TC of water, by doping of nanomaterials to use in solar collectors [10].

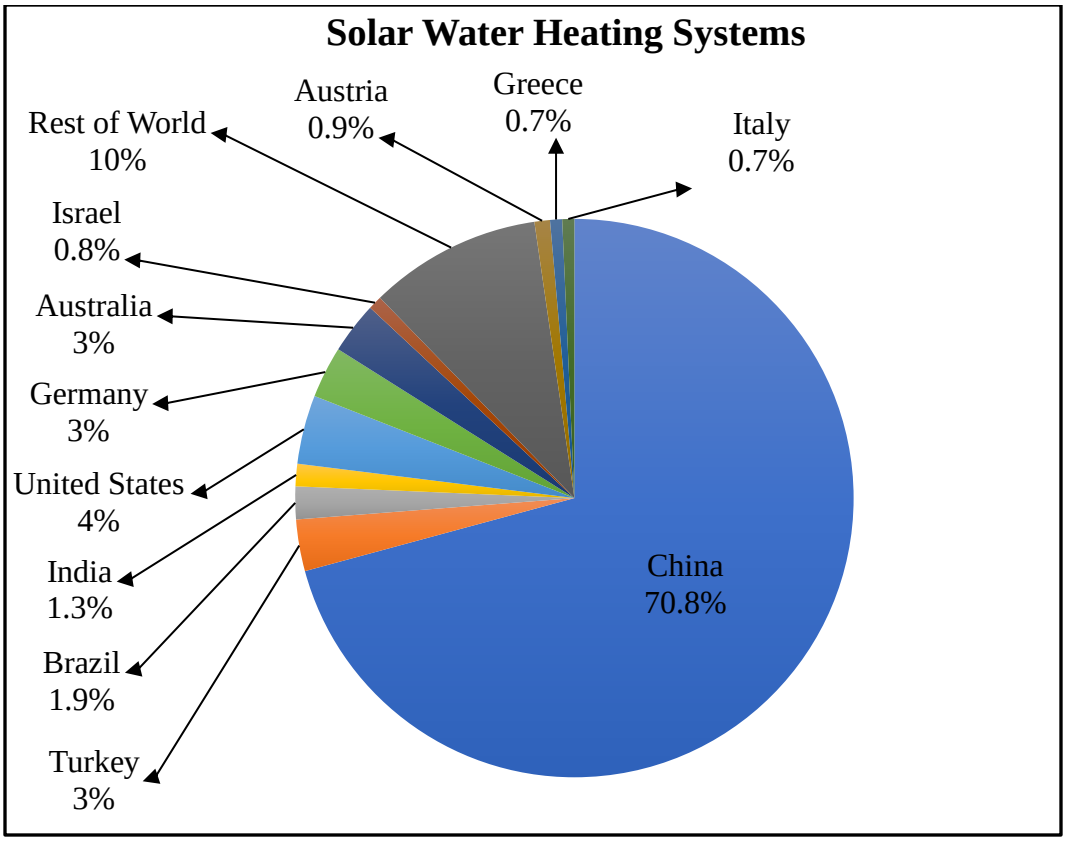

Figure 1-2: SWH systems in top 11 countries from 2005-2015 [6].

Some researchers used ionic liquids such as EG, 1-butyl-3-methylimidazolium hexaflurophosphate and 1-hexyl-3-methylimidazolium tetrafluoroborate etc. as HTF in solar collector [11, 12]. Ionic liquids are having advantages of high operating temperature range, TC and SHC. During the past four decades phase change materials (PCM) are also used as HTFs. PCM are mainly divided in organic (such as paraffins, ketones and fatty acids etc.) and inorganic materials (such as nitrates, carbonates and hydroxides etc.). To store solar thermal energy for long duration, one should utilise PCM. Advances in nanotechnology led to the synthesis of novel nanoparticle which improves performance of base fluids, paraffin

and molten salts [13]. Several investigations conducted to increase TC of base fluids, paraffin and molten salts through doping on nanomaterials [14, 15].

Solar thermal collectors are generally divided into non-concentrating and concentrating thermal collectors as given in Table 1-1. Some of the examples of non-concentrating thermal collectors are (i) flat plate collectors (FPC) and (ii) evacuated tube collectors (ETC). Examples of concentrating thermal collectors are (i) compound parabolic collector, (ii) parabolic trough collector, (iii) linear fresnel collector and (iv) central receiving system.

FPCs are inexpensive, easily available and low maintenance. FPCs are mostly preferred, where low temperature applications (example: bathing) are required. Manufacturing various type of FPC solar absorber to have properties of high transmittance and low reflectance to solar radiation has been described by G. Colangelo et al. [16]. Researchers showed great interest to enhance thermal performance of solar collectors through both simulation and experimental studies. Materials used for manufacturing of FPC and ETC are widely discussed by Alghoul et al. [17]. A compound parabolic collector (CPC) consists of two curved segments identical with two parabolas. It was invented in 1974, since then many improvements in design and performance has been made [18]. To minimise thermal, optical losses, cost and others parameters, many novel designs have been put forward [19, 20]. Parabolic trough collector (PTC) consists of several

parabolic reflectors to focus solar radiation on absorber tube which is filled with heat transfer fluid (HTF) or water depending on application [21]. In central receiver system (CRS), solar radiations are focused on a single point on top of a tower through mirrored reflectors. CRS or power tower consists of three subsystems, i.e., (i) heliostat, (ii) central receiver and (iii) HTF. Latest research and development of designs, enhancement, experiment and commercialization of CRS and its subsystems have been discussed by Behar et al. [22]. Many software techniques are used for tracing of solar radiation on concentrating solar collectors. Some of them are Monte Carlo ray trace method, SOLTRACE, FIAT-LUX, TracPro and etc, [23-25]. In order to balance the rapid increase in global energy consumption, we need to utilise renewable energy. The sun radiates 380 $YW.s^{-1}$ (1 Y = 10^{24}) of energy [3]. Many power plants have been constructed for utilization of solar energy. For example, andasols and arenales power plants of Spain produces approximate energy of 158 GWh/yr using parabolic trough collector technologies [26, 27]. All parabolic trough collectors use 2-tank indirect heat exchange mechanism. In the first tank, heat transfer fluid (HTF) such as eutectic molten salt was used and after melting, it flows from collectors to heat exchanger tank.

Table 1-1: Description of various solar thermal collectors. Data compiled from [3, 21, 22, 28]

Collector type	Description	Concentrating (Y/N)	Cost	Land occupancy	Operating temperature (^oC)	Solar collector ratio	Tracking	Focus	Capacity (MW)
Flat plate	Flat absorber plate in an insulation box covered with transparent material	N	Low	-	30-80	1	Stationary	-	-
Evacuated tube	Array of two concentric tubes. Inner tube having vacuum and coated with selective absorber. Outer tub can be of transparent material	N	Low	-	50-100	1	Stationary	-	-
Compound parabolic	Two parabolic sheets to focus solar radiation on a absorber tube	Y	Low	-	60-240	1-5	Stationary	Line	-
Parabolic trough	Parabolic sheet to focus on a absorber tube	Y	Low	Large	20-400	15-45	One axis	Line	10-300
Linear Fresnel reflector	Array of mirrors to focus solar radiation on one point	Y	Very low	Medium	50-300	10-40	One axis	Line	10-200
Central receiver system	Heliostats are used to redirect solar radiation on to a high tower	Y	High	Medium	300-565	150-1500	Two axis	Point	10-200
Multi dish	Small parabolic dishes to focus solar radiation at one point	Y	Very high	Small	120-1500	100-1000	Two axis	Point	0.01-0.025

In the second tank, water was used to produce steam which is used to drive the turbine. Thus, by effectively utilising HTF, we can reduce the dependence on fossil fuels to produce electricity. HTF also functions as thermal energy storage (TES) material and store energy for long duration of time. Molten salts are TES material that includes salts of hydrates, nitrates, carbonates and their eutectic mixtures. Molten salts possess high thermal cycling stability; they are inexpensive and widely available. On the contrary, molten salts are slightly corrosive in nature and have low thermo-physical properties like TC.

In solar thermal plants, viscosity is one of the most important parameter for proper operation of plant. For instance, the molten salt with low viscosity requires less power to pump. In order to save energy, it is required to work using low viscosity TES material. Study of corrosion properties of metal containing TES material is also very vital. Corrosion effects can alter TES composition, reduction in thermal efficiency of piping system and TES material. For this reason, detailed experimental investigations on effect of viscosity and corrosion properties are needed to study [29].

1.2 Objectives

This work focuses on six objectives (i) Selection of low melting point molten salt, (ii) Enhancing thermal properties of selected molten salt, (iii) thermal stability, (iv) thermal cycling behavior, (v) Rheological studies and (vi) Corrosion behavior. Novelty of this work is to dope GE nanoparticles in the selected molten salt. The eutectic mixture was selected due to the following reasons (i) low melting point of 65 ^{o}C, (ii) high thermal stability > 500 ^{o}C and (iii) HC >1.18 J/g. ^{o}C. Nanomaterials dispersed molten salt was characterized to know the thermal mechanisms and thermal energy storage of the synthesized nanosuspension.

The synthesized molten salts have the potential to be used as TES material in flat plate solar collector. Flat plate solar collector (FPSC) is widely used for production of hot water for daily usage. By integrating TES material into FPSC, solar energy collected during peak time of solar radiation can be utilized for hot water production during the late evening in the summer and early evening in the winter. Consequently, mentioned molten salt can also be used in parabolic or central receiving system due to its high thermal stability >500 ^{o}C.

1.3 Organization of thesis

The thesis is categorized into five different chapters. Chapter I provides introduction to various renewable energies, types of solar collector and TES materials. A brief literature of nanomaterials dispersed in various base fluids was provided. In addition to this, rheology and corrosion was also provided.

Chapter II presents selection of TES and nanomaterials. Predicting of various properties of nanosuspensions, were also compressed. Some of the models studied are (i) thermal equilibrium equation – HC, (ii) Maxwell, Hamilton-Crosser and Nan's models – TC and (iii) Einstein's model – Viscosity.

Chapter III presents synthesis procedure of base salt and nanomaterials dispersed base salt. Syntheses were performed on various types of base salt, nanomaterials and mass concentrations.

Chapter IV presents various characterization techniques used for measurement of HC, TC, viscosity, thermal analysis and corrosion analysis.

Chapter V presents application of flat plate solar thermal collector and PV/thermal collector using base salt and GE dispersed base salt. Results of base salt and GE dispersed base salt were also compared with water.

Final chapter provides conclusion of results obtained through characterizations and application part.

1.4 Findings

This work contributes to nanofluids as follows:

(a) Thermo-physical properties of base fluid and nanosuspensions were investigated for heat transfer applications.

(b) Thermo-physical properties of nanosuspensions were predicted using theoretical models.

(c) Rheological properties of base salt and nanosuspensions were studied and compared with theoretical models.

(d) Corrosion behavior of base salt and nanosuspensions were also studied here.

(e) Practically applied base salt and GE dispersed base salt to flat plate solar thermal collector and PV/thermal collector – application studies.

(f) Application studies confirmed that GE dispersed base salt can be applied to domestic water heating systems. This makes GE dispersed base salt makes as potential solution for domestic water heating systems.

Research has been done to use molten salt as TES material only for high temperature applications. For high temperature applications, high melting point molten salt has been used such as Solar, Hitec and Hitec XL salts

having melting point at 220 ^{o}C, 142 ^{o}C and 140 ^{o}C, respectively. Novelty of this research is that nobody has used low temperature melting point molten salt with high thermal stability. This makes selected molten salt to be used in both low and high temperature applications. In addition to this, we have enhanced thermal properties of molten salt by doping GE. This makes energy stored per unit volume has been enhanced.

CHAPTER – 2

LITERATURE REVIEW

2.1 Introduction

This chapter gives an overview on different designs of SWH system and solar thermal collectors including non-concentrating and concentrating are discussed in detail. This chapter also gives details of recent advancement and modifications made in enhancing the performance of thermal collectors. Special attention is given to discuss the design and geometric modifications. An overview on current status in the development of TES materials is also being presented. Molten salts as TES materials has been discussed in detail as they operate at both low and medium temperature range, possess high density and good specific heat capacity (SHC). On the other hand, organic materials such as paraffins can be used as TES for low and medium temperature applications. Due to rapid progress and advancement in nanotechnology, an extensive research to enhance TC of base fluids, ionic liquids, paraffins and SHC of molten salts using nanomaterials has been widely discussed.

2.2 Types of Solar Water Heating (SWH) system

Solar collector is one which converts solar energy into internal heat energy of the system or of fluid. Thermal energy can be stored in HX for use at night and/or cloudy days. Fernandez and Dieste [9] developed an economical solar thermal collector for low and medium temperature applications. Solar water heating (SWH) system includes solar thermal

collectors and storage tank. There are two types of SWH system: 1) active SWH system and 2) passive SWH system [30].

2.2.1 Active SWH system

In an active SWH system, pumps and other components (valves and electronic controllers) are required for proper operation. Exchange of fluid is actively done from the storage tank to the collector and vice versa. Comakli et al. [31] showed that for economic and efficient SWH system, size of FPC area and storage tank need to be optimised. It was reported that for Turkey's atmospheric conditions, the ratio of storage tank to FPC area were between 50 to 70 L/m^2 for usable water temperature between 45 to 60 ^oC. Simulation analysis of active SWH system with water to water and water to air HXs was performed by Badescu [32]. It was concluded that the amount of solar energy used for hot water preparation using water to water HX was 10 times more than space heating using water to air HX. An active SWH system which is further classified into i) direct circulation system and ii) indirect circulation system. These systems are further discussed in the following sections.

2.2.1.1 Direct Circulation system

In this type of system, solar energy is directly transferred to water which is circulated through the collector to the storage tank. No antifreeze solution or heat exchanger (HX) is used because water is directly heated and utilised for household purpose. Many researchers have studied forced

circulation in direct circulation system and the details of the findings are reported in section 2.2.1.1.1 below.

2.2.1.1.1 Enhancement through design and simulation

Chong et al. studied on forced circulation SWH system with V-trough collector and the proposed prototype, resulted in high optical efficiency of 74.05%. Besides high optical efficiency, the proposed prototype was of low cost and good thermal efficiency. Li et al. [33] developed a heat transfer model to validate forced circulation SWH system. This model was made by using buoyancy equation of natural and forced circulation. The developed model was in good agreement with the experimental results with <5% deviation. Walker et al. [34] carried out simulation studies on designed ETC for SWH system and predicted the heat transfer efficiency of SWH system was 34% in Philadelphia. Simulation studies were carried out by estimating annual thermal energy and thermal efficiency of the system.

2.2.1.2 Indirect circulation system

This system is mainly used, where the climatic condition reaches the freezing point of water and thermal energy need to be stored for use at night. Antifreeze solution circulates through the collector and transfers the heat to the HX tank through pump. Another pump circulates water from HX to storage tank as shown in Figure 2-1. Antifreeze solution through

the collector and to HX is kept in a closed loop. However, drawback about this system is that it loses thermal energy due to convection in HX tank.

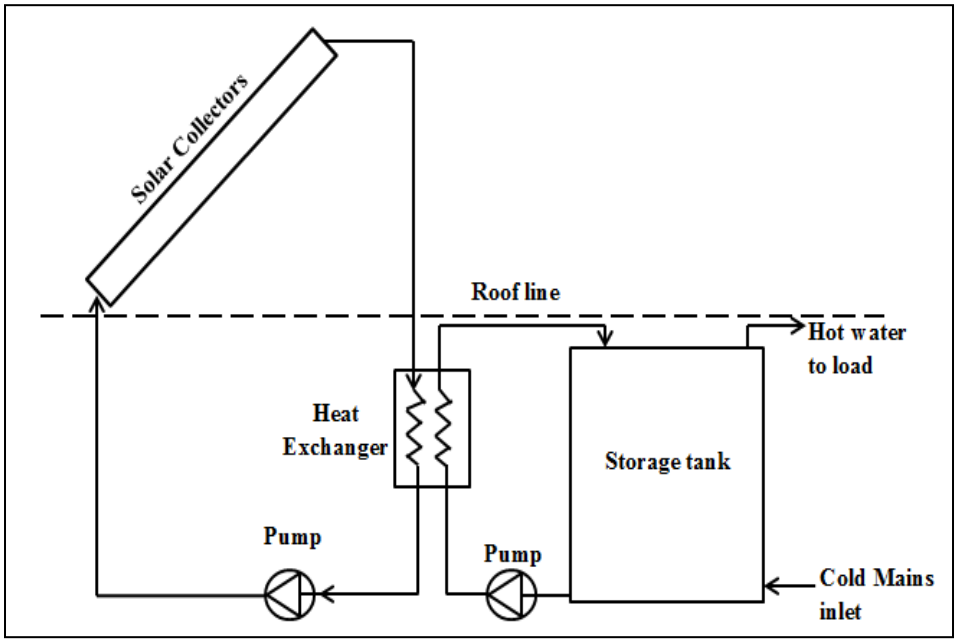

Figure 2-1: Schematic diagram of indirect circulation system [35].

2.2.1.2.1 Enhancement through design and simulation

Numerous experimental and theoretical studies have been reported on solar assisted heat pumps in indirect circulation system [36, 37]. Experimental performance of direct expansion solar-assisted heat pump water heater (DX-SAHPWH) was conducted by Li et al. [38]. DX-SAHPWH was assembled using direct expansion collector, hermetic compressor, thermostatic expansion valve and water. It was observed that the coefficient of performance (COP) of DX-SAHPWH system was 6.61. It was also observed that an average solar radiation intensity of 955 W/m^2

is required to heat 150 L of water from 13.4 °C to 50.5 °C. Chaturvedi et al. [39] investigated thermal performance of a direct expansion solar assisted heat pump (DXSAHP). The proposed system consists of solar collector, compressor and water. It was found that the experimental results of DXSAHP were in good agreement with theoretical results. They also found COP within range of 2.5-4. Chyng et al. [40] investigated COP of integral-type solar assisted heat pump through both experimental and simulation studies. Simulation was done using formulae of Rankine cycle and performance of thermosyphon loop. Simulation studies were in good agreement with experimental results. They obtained that the COP within the range of 1.7-2.5.

Apart from enhancing performance of indirect circulation system through various designs, many researchers investigated on various geographic locations too [41]. Hawlader et al. [42] investigated COP and thermal efficiency on solar assisted heat pump dryer and water heater in Singapore. The proposed system mainly consists of variable-speed compressor, collector, storage tank, condenser, blower, dry and dehumidifier. Simulation studies were carried out using FORTRAN language. They obtained that COP and thermal efficiency as 6.0 and 0.77, respectively. Simulation results were also in good agreement with experimental results. Kuang et al. [43] carried experimental and simulation studies on DXSAHP in Shanghai, China. FORTRAN program was developed to predict thermal performance of the system. They

obtained COP and collector efficiency ranging from 4-6 and 40-60%, respectively. Predicted COP was obtained as 2.5, the discrepancy between experimental and theoretical results was due to latent heat gain from the surroundings.

Apart from using water as HTF in indirect circulation system, research has been carried out on refrigerants as HTF. Molinaroli et al. [44] carried out numerical analysis to investigate the characteristics of a DXSAHP for space heating purpose using R-407C as working fluid as shown in Figure 2-2. It was concluded that the COP of heat pump was influenced by ambient temperature, solar radiation and independent of solar field surface. Thermal performance of DXSAHP using various refrigerants was analyzed by Gorozabel Chata et al. [45]. The compared refrigerants were R-12, chloro-fluorocarbon, R-22 and R-134A.

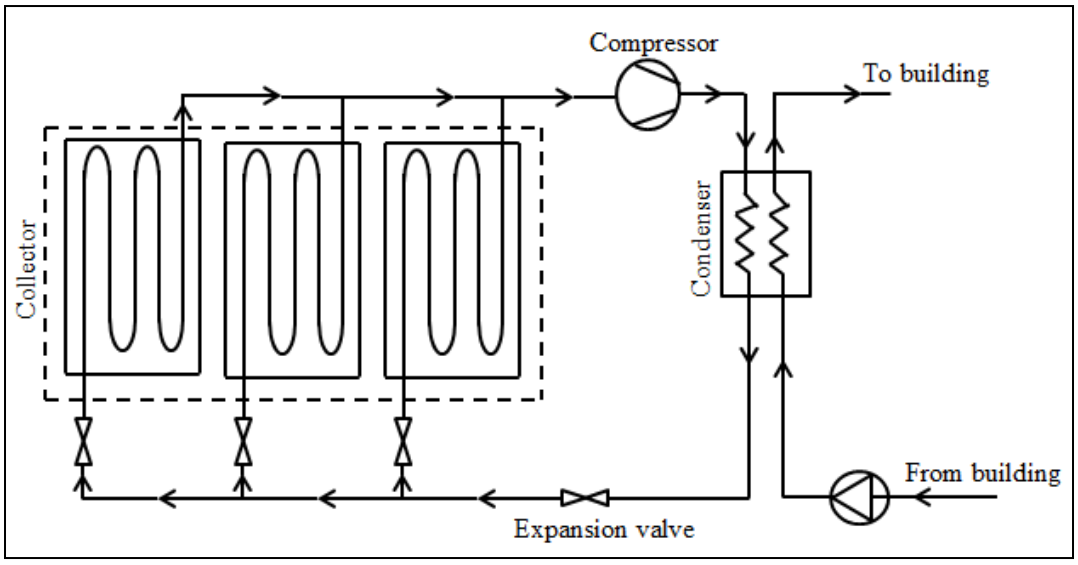

Figure 2-2: Schematic diagram of DXSAHP system [44].

It was concluded that highest COP obtained through R-12 refrigerant. This is because R-12 has high critical temperature compared to R-22 and R-134A. Moreno et al. [46] developed a theoretical model for investigating thermal performance of DXSAHP system using R-134A refrigerant. They obtained that the COP of DXSAHP system was within range of 1.7-2.9 and theoretical COP was within range of 1.85-3.1. Thus, they concluded that the theoretical model successfully validates experimental values and was within the accuracy of <20%. However, author suggests that it is essential to improve the thermal performance of direct circulation system as COP is quiet low than other systems. New designs of direct circulation system can be tried for enhancing COP.

2.2.2 Passive SWH system

Unlike in active system, pumps and other accessories are not required for its operation. This system will be operated using water pressure and solar radiation. The thermal efficiency of both active and passive SWH system based on annual operation in South Korea was investigated by Lee and Sharma [47]. Experimental results show that ethylene glycol as HTF in active SWH system is good for cold climate countries due to its antifreeze properties. Passive SWH system are further divided into two types: i) integral collector-storage systems and ii) thermosyphon systems. These two systems are further discussed in the following sections.

2.2.2.1 Integral Collector Storage (ICS) system

Simplest design of integral collector storage (ICS) system is shown in Figure 2-3. When hot water is drawn from ICS system by opening faucet, simultaneously cold-water flows in and fills in the ICS system. However, the main drawback of ICS system is that it is only suitable for mild and warmer climates. Precautions were taken to combat freezing in winter and heat loss at night such as surface coating, insulating materials and covering the collector glazing at night. Even if an ICS system is drained for winter and only used for 6-7 months during summer period, it can still have a significant impact on annual energy cost. Since, the installation cost is much lower than other SWH systems [48].

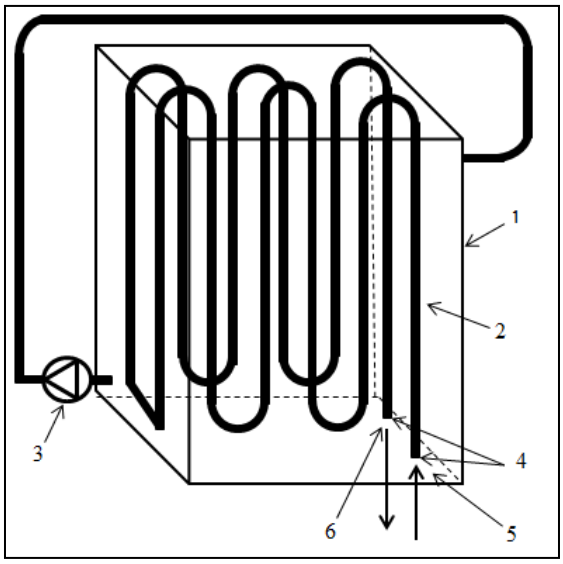

Figure 2-3: Schematic diagram of ICS (1) storage tank, (2) heat exchanger, (3) pump, (4) flow sensors, (5) water inlet and (6) water outlet [49].

2.2.2.1.1 Enhancement through design and simulation

Thermal diode mechanism is transfer of thermal energy from vapor to liquid state and vice versa. Souliotis et al. [50] designed a ICS SWH system consisting of two concentric cylinders, which were horizontally placed inside a truncated asymmetric CPC. It was partially filled with small amount of water. It permits the phase change at low pressure and temperature creating a thermal diode mechanism. It was further showed that the thermal diode mechanism plays a significant role in effective operation of ICS system. It was concluded that the designed ICS system has high thermal performance than flat plate thermosiphonic unit and thermal losses are close to flat plate thermosiphonic unit. Mohamad [51] also constructed ICS collector with thermal diode mechanism. Theoretical analysis shows the thermal diode mechanism has a significant effect on reducing heat losses of the system during nighttime.

Designing of efficient ICS system is one of the major factors in improving performance/efficiency of the system. Many researchers have explored various designs of ICS that are reported here. Goetzberger and Rommel [52] designed and evaluated the efficiency of an ICS system and compared with efficiencies of thermosyphon system, FPC and vacuum tube collectors. It was concluded that the efficiency of designed ICS was higher than thermosyphon system & FPC but lower than vacuum tube collectors. Comparison of designed ICS system with other systems was evaluated based on three parameters. They are (i) demand of water was 160 L/day,

(ii) water to be in between 8-50 ^{o}C and (iii) collector area to be 1 m^2. Besides efficiency, the designed ICS system was less expensive than conventional domestic hot water system. Schmidt and Goetzberger [53] developed a new ICS system by placing single tube absorber in front of solar collector and covering glass coated with polycarbonate materialhighly transparent polycarbonate insulation material. Results showed that thermal performance of new ICS system was much higher than conventional domestic hot water system and was identical to thermal performance of vacuum tube collectors. Polycarbonate coating on glass reduces heat losses of ICS sytem. Kalogirou [54] designed a new ICS system and calculated its experimental and simulation performance. Simulation studies are carried out using BASIC language. It was found that the optical efficiency of designed ICS system was 57% and simulation studies result having deviation of <5.1%. Symth et al. [55] designed various vessels for water storage in ICS system. It was found that storage vessel with two-third area inner perforated of 3 mm holes provides good thermal storage. Perforation was done to enhance thermal retention property of the vessel. With this design, they found that the thermal energy can be saved up to 30% and prevents heat loss up to 20% compared to normal water storage vessel in ICS system. Helal et al. [56] designed and studied thermal efficiency of ICS system. Main aim of the designed ICS system is to provide hot water for a family of 4 persons. Designed ICS system consisted of three compound parabolic reflectors with horizontal

storage tank at the center. They obtained thermal efficiency higher than 64%. Theoretical studies showed that ICS water temperature depends on CPC geometry, length and aperture area.

Apart from enhancing efficiency of ICS system through various designs, several researches have been carried out by using phase change material (PCM). Canbazoglu et al. [57] designed ICS water storage system with two sections. In the first section, they placed PCM (sodium thiosulfate pentahydrate) and water in second section. With this modified design the water tank temperature increased with solar radiation intensity. After the sun set, storage tank temperature remained constant at 45 ^{o}C for 10 hour due to the natural property of PCM to store heat. Reddy [58] designed, modelled and analyzed water storage mechanism in ICS system. He used transparent thin insulation layer between water storage and paraffin wax.

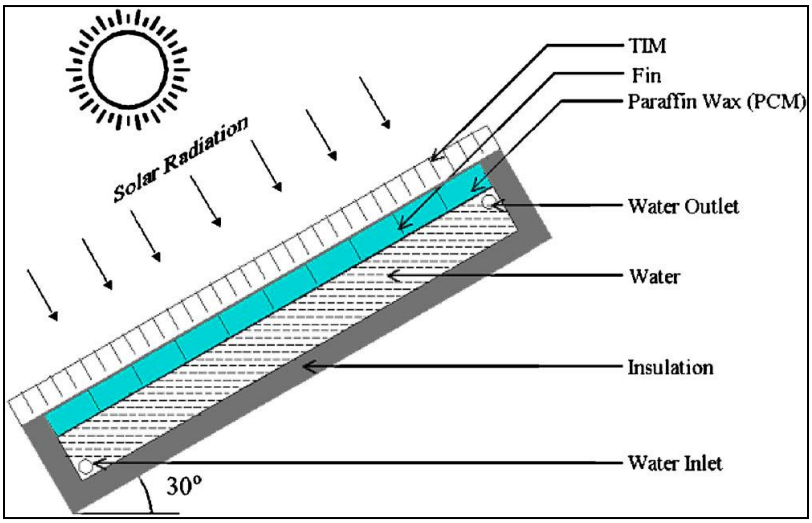

Figure 2-4: ICS system integrated with 9 fins inside paraffin wax [58].

He compared the performance of 4, 9, 12 fins which were made in the storage section of paraffin wax as shown in Figure 2-4. By these designs, it was found that the storage section of paraffin wax with 9 fins are optimum for maximum enhanced heat transfer and minimum thermal energy losses of the system.Chaabane et al. [59] used two types of PCM; RT42-graphite and mystric acid in ICS system for water heating. It was observed that both PCMs showed enhanced thermal performance compared to water. RT42-graphite showed enhanced thermal performance for longer period of time than mystric acid. This is due to thermal conductivity of RT42-graphite (5 W/m.K) is higher than myristic acid (0.19 W/m.K).

2.2.2.2 Thermosyphon system

Thermosyphon SWH system uses sunlight to strike tubes and fins within the collector box in which water or fluid is circulating. The heated fluid transfers thermal energy from solar collector to the storage tank through a process called ‘Thermosyphon’. Thermosyphon is a natural convection process in which density difference causes fluid flow within the system. The inlet and outlet of the collectors are plumbed together to form a loop. Advantages of thermosyphon SWH system are simple, efficient, unaffected by utility blackout and pumps heat through a pipe without external power [60]. Disadvantages of thermosyphon SWH system includes strict guidelines of plumbing and to avoid bubble blocks.

2.2.2.2.1 Enhancement through design and simulation

For solar collectors, one of the important parameters is climatic condition which determines production of hot water. Chuawittayawuth and Kumar [61] theoretically and experimentally analyzed the temperatures of thermosyphon system under different sky conditions. Schematic diagram of thermosyphon system is shown in Figure 2-5. It was found that the temperature of thermosyphon system was higher for clear sky compared to other sky conditions. Temperature of thermosyphon system was uniform for partially cloudy and cloudy skies.

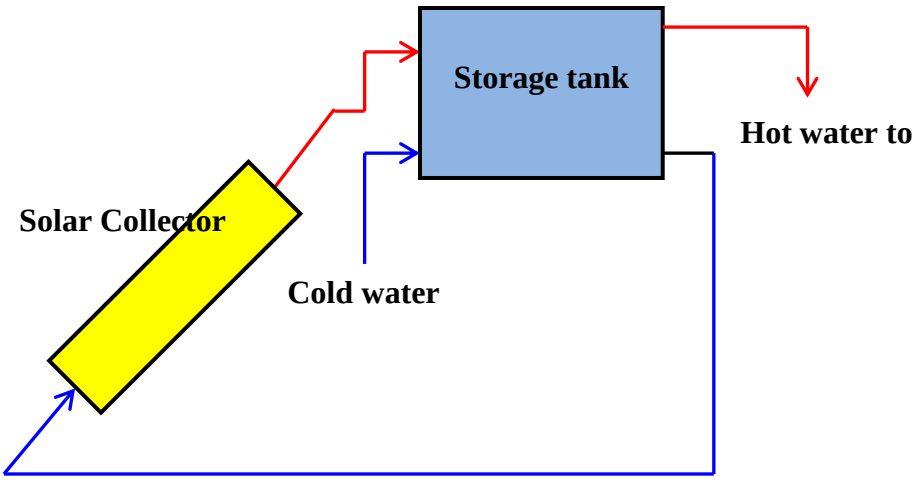

Figure 2-5: Schematic diagram of thermosyphon systems [61].

Huang et al. [62] evaluated thermal performance of thermosyphon SWH system with a mantle HX for its applicability in China. Their experimental result shows that thermal performance of thermosyphon SWH system with mantle HX was lower than that of normal thermosyphon SWH system, but higher than that of glass evacuated tube SWH system. This is due to loss of heat energy due to convection with the addition of mantle HX to

thermosyphon SWH system. Efficiency of thermosyphon SWH system with a mantle HX got decreased but not lesser than glass evacuated tube SWH system.

Apart from using working fluid as water, many researchers have also used refrigerants for investigating enhanced performance of thermosyphon SWH system. Esen and Esen [63] constructed a two phase thermosyphon system and investigated thermal performance of the system using three refrigerants R410A, R-134a and R407C. It was found that the refrigerant R410A with highest collection efficiency of 50.84% than 48.72% and 49.43% for R-134a and R407C, respectively. Yamaguchi et al. [64] designed a thermosyphon system in which they used working fluid as supercritical CO_2. This CO_2 absorb heat through solar radiation and heat was dissipated in heat exchanger to water. With this proposed design collector efficiency obtained was 66.6%.

Numerous works on simulation and performance enhancement of thermosyphon SWH system has been carried out and some of them are presented here. The two-phase thermosyphon SWH system was discussed experimentally and theoretically by Chien et al. [65]. It was found that the simulation and experimental results are within an average error deviation of ±6%. To improve thermal performance, two strategies were used: (i) double fin tubes and (ii) nano particles. Budihardjo and Morrison [66] carried out experimental and simulation studies of water in glass evacuated tube SWH system and flat plate SWH system. Their study came

into conclusion that the performance of 30 tubes in evacuated tube SWH system was lower than two flat plate SWH system of 3.7 m^2 due to increase in heat transfer area.

There exists lot of research works related to design of thermosyphon system and few of them are discussed here. Chen et al. [67] designed a new two-phase thermosyphon system. It consists of solar collector, internal parallel fins, double pipe HX and storage tank. It was found that the proposed design has 18% higher thermal efficiency compared to the other SWH systems. Arab et al. [68] investigated heat transfer efficiency of extra-long pulsating heat pipe in a thermosyphon SWH system. The system was also tested with three different filling ratios (30%, 50% and 70%) of water. Thermal efficiency was increasing with respect to filling ratio of water and the highest thermal efficiency recorded was 53.79% at 70% filling ratio. Redpath et al. [69] compared efficiencies of both thermosyphon and forced circulation mechanisms in a heat pipe evacuated tube SWH system. They obtained that the efficiency of thermosyphon heat transfer mechanics was 5.1% lesser than forced circulation mechanism. However, the study also concluded that the cost can be reduced by using thermosyphon circulation instead of forced circulation mechanism. Redpath et al. [70] in another study installed thermosyphon heat pipe evacuated SWH system at three different locations. It was reported that terraced dwelling thermosyphon heat pipe evacuated SWH system has

more annual solar fraction than semi-detached and dwellings. Table 2-1 provides recent studies on various types of SWH systems.

Table 2-1: Recent studies on SWH systems [8, 71]

System	Reference	Study		Collector	Working fluid	Thermal efficiency (η) / COP / optical efficiency	Analysis
		Simulation	Experimental				
Direct circulation system	Li et al. [33]	√	√	ETC	Water	-	-
	Walker et al. [34]	√		Evacuated tube heat pipe	Water	η=34%	Low cost and high efficiency
	Chong et al. [72]	√	√	V-trough reflector	Water	Optical η=74.05%	Low cost and high efficiency
Indirect circulation system	Chaturvedi et al. [39]	√	√	Flat plate with tubes	R-12	COP=2.5-4.0	High COP
	Hawlader et al. [42]	√	√	Evaporator collector	Air	COP=6.0, η=0.77	High COP and efficiency
	Chyng et al. [40]	√	√	Tube-in-sheet type	R-134a	COP=1.7-2.5	High COP
	Kuang et al. [43]	√	√	FPC	R-22	COP=4-6, η =0.4-0.6	High COP and efficiency
	Li et al. [38]	√		Aluminum plate	R-22	COP=5.25, η=1.08	High COP, cost and efficiency
	Hepbasli [73]	√		FPC	Water-antifreeze mixture	COP=0.201	Low COP
ICS system	Mohamad [51]	√	√	FPC storage	Water	η=50%	High efficiency
	Goetzberger and Rommel [52]		√	Built-in-storage	Water	η=26-35%	High efficiency and low cost
	Kalogirou [54]	√	√	CPC	Water	η=65%	High efficiency and low cost
	Helal et al. [56]	√	√	CPC	Water	η=64%	High efficiency
	Smyth et al. [55]	√	√	Built-in-storage	Water	IOP	Low cost
	Reddy [58]		√	Built-in-storage	Water	IOP	-
	Canbazoglu et al. [57]		√	Built-in-storage	Water	IOP	High cost
	Tripanagnostospoulos and Souliotis [74]		√	CPC	Water	IOP	Low cost and improved efficiency
	Tripanagnostospoulo	√	√	CPC	Water	IOP	Low cost

	s et al. [75]						and improved efficiency
Thermosyphon system	Esen and Esen [63]		√	FPC	R-134a	η=48.72%	High efficiency
			√		R-407C	η=49.43%	High efficiency
			√		R-410A	η=50.84%	High efficiency
	Chien et al. [65]	√	√	FPC	Alcohol	η=82%	High efficiency
	Chen et al. [67]	√	√	FPC	Alcohol	η=63%	High efficiency
	Arab et al. [68]		√	FPC	Water	η=54%	High efficiency
	Ng et al. [76]		√	Evacuated tube heat pipe	Water	η=59-66%	High efficiency
	Redpath et al. [69]	√	√	Evacuated tube heat pipe	Water	IOP	Low cost
	Budihardjo and Morrison [66]	√	√	ETC	Water	IOP	-

*IOP=Investigated other parameters

2.3 Flat plate collectors

Flat plate collectors (FPC) are fixed at one point and does not require tracking of solar irradiation and working fluid is circulated as a heat transfer material [77]. A FPC consists of heat absorbing plate with coating, copper tubes, enclosure along with insulation, and glazing sheet as shown in Figure 2-6. To avoid complexities of using equipment (like sensor) for analysis, authors suggested making use of software techniques such as computational fluid dynamics (CFD) or finite element method (FEM). These software techniques also help us to analyze temperature distribution in collector and water [78].

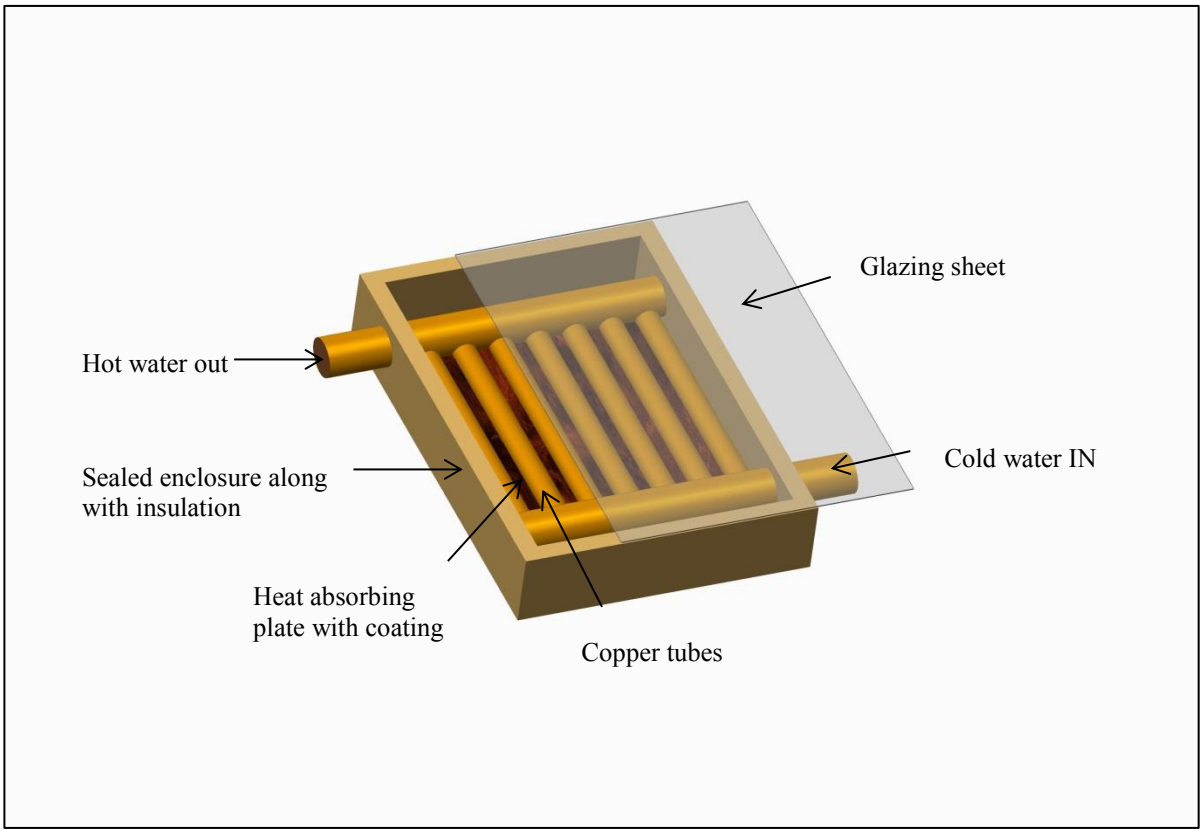

Figure 2-6: Flat plate collector (FPC).

2.3.1 Enhancement through design and simulation

Volumes of research were carried out for enhancing performance of FPC through various designs; few of them are presented here. Chen et al. [79] studied thermal efficiencies of FPC with and without ethylene tetrafluro ethylene (ETFE) foil. ETFE material was selected as it is having high (~95%) light transmittance property. It was found that ETFE foil between glaze cover and working fluid showed enhanced efficiency compared to

without ETFE foil, when the average working temperature of the fluid was more than 30 ^{o}C. Further, when the fluid temperature was more than 60 ^{o}C then collector with ETFE foil has approximately 10% higher thermal performance than the collector without ETFE foil. Garcia et al. [80] successfully inserted copper wire coil within the flow tubes in solar water collectors for enhancing thermal efficiency. Wire-coil insertion shows an average enhancement in thermal efficiency of 31% at $0.25\dot{m}_R$, 15% at $0.40\dot{m}_R$. At $0.60\dot{m}_R$, $\dot{m}_R$ and $1.2\dot{m}_R$ ($\dot{m}_R$ mass flow rate =144 Kg/h), the average enhancement in thermal efficiency was 16%, 15% and 14%, respectively.

Efficiency of FPC also depends on flow rate of working fluid. Fan and Furbo [81] investigated both theoretical and experimental analyses on flow and temperature distribution in a 12.53 m^2 FPC using CFD. It was concluded that the three forces are dominating the flow distribution in the collector panel namely: (i) pressure drop in strips, (ii) inertial and frictional pressure changes in manifolds and (iii) buoyancy effect. It was measured and analyzed that the smaller pressure drops in the strips; then the buoyancy effect will be higher. If pressure drops in strips is smaller than the buoyancy pressure, then it may physically damage the collector. To avoid the boiling problems in collector panel, it was recommended that collector volume flow rate should be more than 6 lit/min.

Higher performance of FPC can be obtained through coating on absorber plate, were presented here. Del Col et al. [82] experimentally

characterized the performance of three different types of FPC as shown in Figure 2-7. They are (i) copper sheet with selective coating (black coating) and copper tubes, (ii) aluminum sheet with selective (black) coating and aluminum tubes and (iii) aluminum roll-bond with semi-selective (black) coating. It was concluded that aluminum roll bond collector with semi-black coating was having higher thermal efficiency than the copper collector with same black paint. It was also more efficient than the aluminum collector with selective coating. The enhancement in thermal performance of aluminum roll-bond with semi-selective coating was due to high number of channels in the absorber.

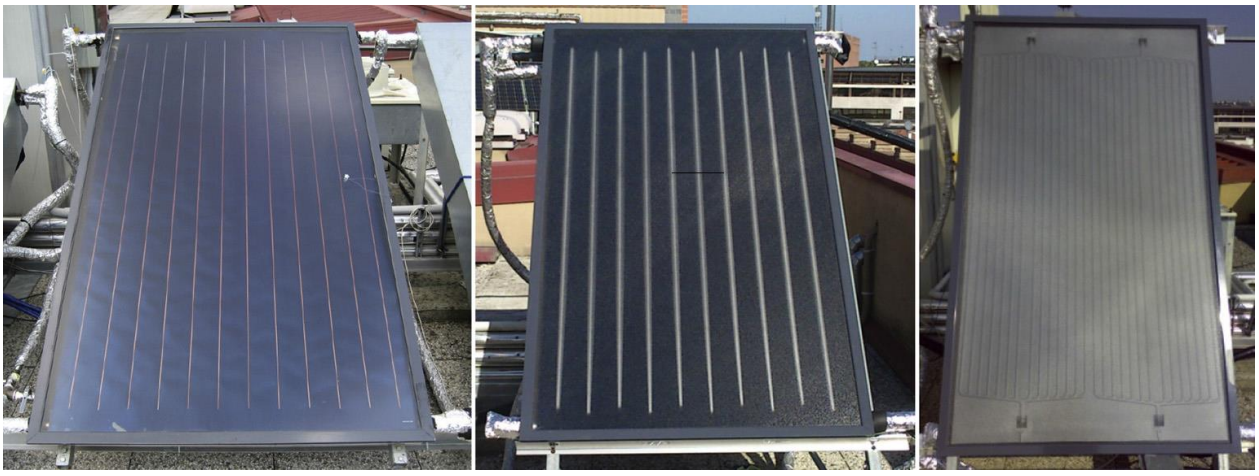

(a) (b) (c)

Figure 2-7: Three different solar collectors. (a) Copper sheet with selective coating and copper tubes. (b) Aluminum sheet with selective coating and aluminum tubes. (c) Aluminum roll-bond with semi-selective coating [82].

Comparison of two double glazed glass cover with tin doped indium oxide and aluminum doped zinc oxide was investigated by Giovannetti et al.

[83]. It was concluded that the tin doped indium oxide has low emissivity and high transmittance than aluminum doped zinc oxide glass cover. This is because of tin doped indium oxide has high transmittance and low emissivity than aluminum doped zinc oxide. For manufacturing of FPC, generally, copper material will be selected for heat pipes and plates, due to its high heat conductivity property. However, other materials can be used depending on the application or base fluid.

2.4 Evacuated Tube Collectors

Evacuated tube collectors (ETC) consist of a series of glass or metal strips with absorber pipe inside each tube. Absorber pipes contain flow of water or fluid for transporting heat [77]. ETC exhibits better thermal performance than FPC, particularly in high temperature operation [84]. The low manufacturing cost and high thermal performance of the fluid-in-glass collector gives it a wide market.

2.4.1 Enhancement through design and simulation

Numerous researches have been performed to enhance the efficiency of ETC through various techniques. Some of the techniques are (i) designs, (ii) fins, (ii) tilt angles and (iv) coating. Efficiency of ETC is mainly dependent on thermal and optical efficiency. An improved procedure of optical efficiency for ETC was presented by Zambolin and Del [85]. CPC reflectors were used in specific geometry behind ETC. This reflector solely affects the optical efficiency of the collector. Reflectors enhanced

the optical efficiency by 0.274 (66% higher) in near normal incident angle conditions. It was showed that extended multiple regression formula best fit to their experimental results. Liang et al. [86] compared thermal efficiencies of water filled evacuated U-tube and copper fin evacuated U-tube. It was found that when heat transmission component reaches 10 W/m.K, then thermal efficiency of water filled U-tube evacuated tube is similar to thermal efficiency of copper fin evacuated U-tube. It was also found that when thermal conductivity of heat transmission components reaches 100 W/m.K, thermal performance of water filled U-tube evacuated tube was 12% higher than copper fin evacuated U-tube. The reason is that the higher the heat transmission, the greater will be the heat conduction between evacuated tube and the working fluid. Tang et al. [87] carried out experiments with two different tilt angles from the horizon, one inclined at 22^{o} and another at 46^{o}. It was found that collector tilt-angle of evacuated tube SWH system has no significant influence on solar heat gain of the system. But to get maximum heat gain, collector should be kept at an angle in such a way that it should get maximum solar radiation. Among non-concentrating solar thermal collector, ETC has high thermal efficiency, less expensive and long time performance [88]. Authors suggest besides selection of tube material; tilt angle is also an important parameter for ETC performance.

2.5 Concentrating Collectors

2.5.1 Compound Parabolic Collectors (CPC)

Flat plate and evacuated collectors are usually for temperature in between 30-200 ^{o}C [3]. To attain higher temperature, solar irradiance collection should be maximized. CPC are non-imaging reflectors which will concentrate the incident radiation to the absorber tube.

2.5.1.1 Enhancement through design and simulation

Kaiyan et al. [19] designed novel CPC which consist of multiple curved surfaces. It was concluded that with the proposed design, light was concentrating on a single point, which was analyzed through light ray tracing simulation technique. Recently, Guiqiang et al. [20] designed lens walled CPC with air gap. Firstly, normal CPC was bent inwards by 3^{o} inclination. Later, the original lens was coated with dielectric material on back side. Coated lens and CPC were joined by leaving some air gap, as shown in Figure 2-8. When incident angle was less than critical angle then total internal reflection took place, and reflected on CPC through dielectric material. The proposed design enhances optical efficiency and total internal reflection of CPC. Li et al. [89] developed and compared two truncated CPC by combining CPC with U-shape evacuated tube. Two CPC were designed with two different concentration ratio of 3.06 and 6.03 as shown in Figure 2-9. Main aim of the design is to minimize geometrical volume with unaltered optical efficiency. It was found that the optical

efficiency of 0.74 and 0.70 and thermal efficiency of 51% and 54% for 3.06 and 6.03 CPC, respectively. It was concluded that the heat loss of two CPC was identical and theoretical model was validated for both system. Gudhekar et al. [90] designed a lower cost CPC by reducing aperture area and mirror area. They obtained thermal efficiency of designed CPC was up to 71%. Theoretical formulae for calculating optical and thermal performance of CPC were described by Rabl [91]. Authors suggest to opt for lens walled CPC with air gap due to its higher thermal and optical efficiency compared to other CPC.

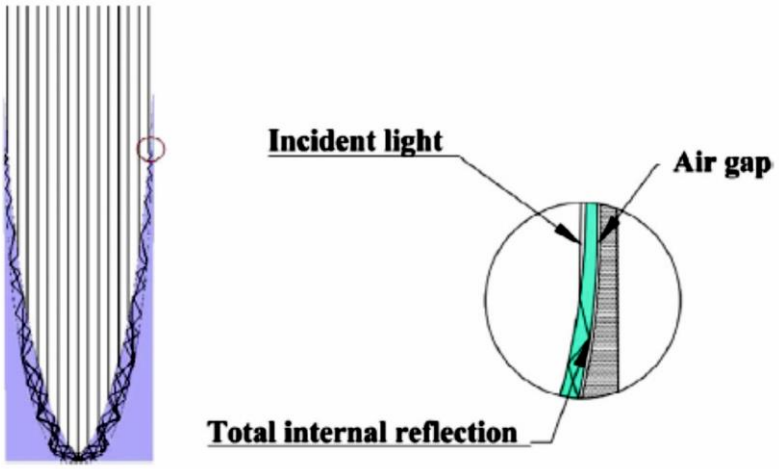

Figure 2-8: Optical path of lens walled CPC with air gap [20].

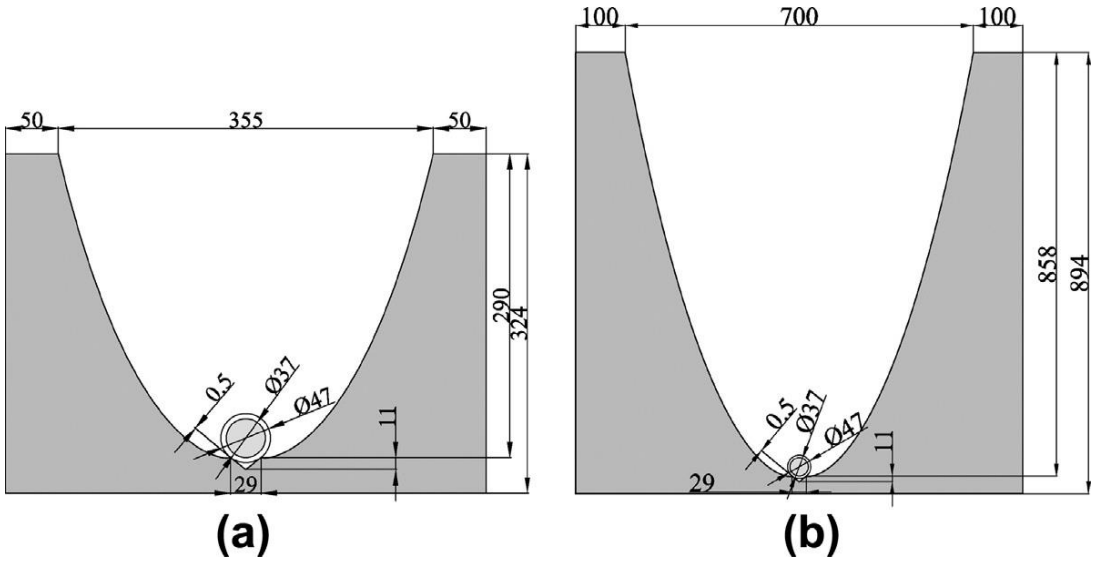

Figure 2-9: Two CPC collectors: (a) 3.06 and (b) 6.03 concentrator ratios.

2.5.2 Parabolic Trough Collectors (PTC)

Main purpose of PTC was to focus the solar radiation onto the surface of black coated absorber tube placed in the focal line, as shown in Figure 2-10. Practical design parameters for PTC were to use highly efficient material with low cost, easily transportable and good performance for a period of around 30 years [92]. First parabolic ultimate trough collectors used in solar energy generating systems–I, had an aperture area of 120 m^2 and aperture width of 2.5 m [93].

Enhancement through design and simulation

Amelio et al. [94] evaluated thermal performance of an integrated solar combined cycle (ISCC) plant with PTC. ISCC plant was made up of two sections: (i) air from outside was taken in, compressed and sent to linear

parabolic collector, where it was again heated up to 580 ^{o}C. Then, air was sent to combustion chamber which was operated by natural gas, such that the temperature reaches to 1200 ^{o}C. (ii) Heat recovery steam generator and turbine. By using this technique, efficiency of producing electricity by combined fossil fuel and ISCC system was improved from 51.4 to 60.9 %.

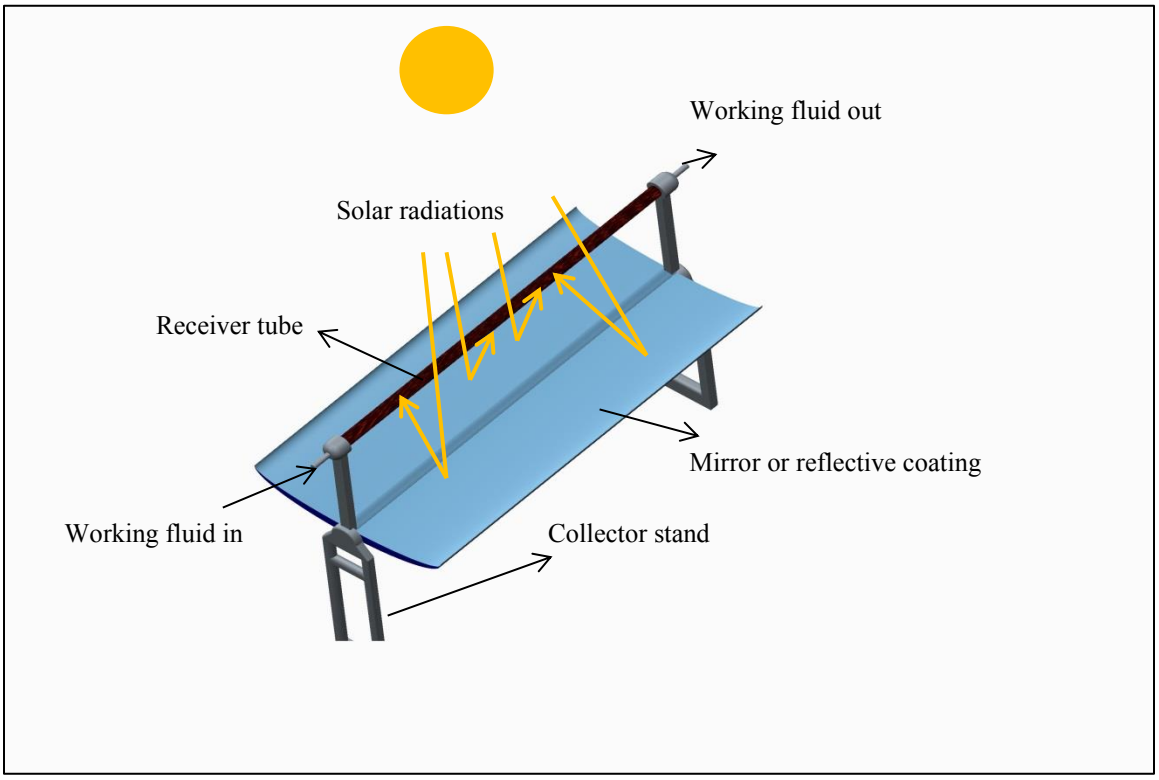

Figure 2-10: Parabolic trough collector.

Xiao et al. [95] developed V-cavity absorber with rectangular fins in PTC as shown in Figure 2-11. Optical performance of absorber was analyzed by Monte-Carlo ray tracing method (MCRTM). It was found that the average outlet temperature of HTF got increased from 109.8 ^{o}C to 110.9 ^{o}C and the temperature of surface heating decreased from 136.2 ^{o}C to

121.5 ^{o}C. Thus, by using V-cavity absorber with rectangular fins in PTC shows enhancement in heat transfer and decrease in heat loss. Comparison of PTC and linear fresnel collector (FC) was conducted by Cau and Cocco [96]. It was compared based on two parameters land and optical efficiency. If land availability is limiting factor then linear FC are preferred (about 55-60 kWh/y per m^2 based on FC vs 45-55 kWh/y per m^2

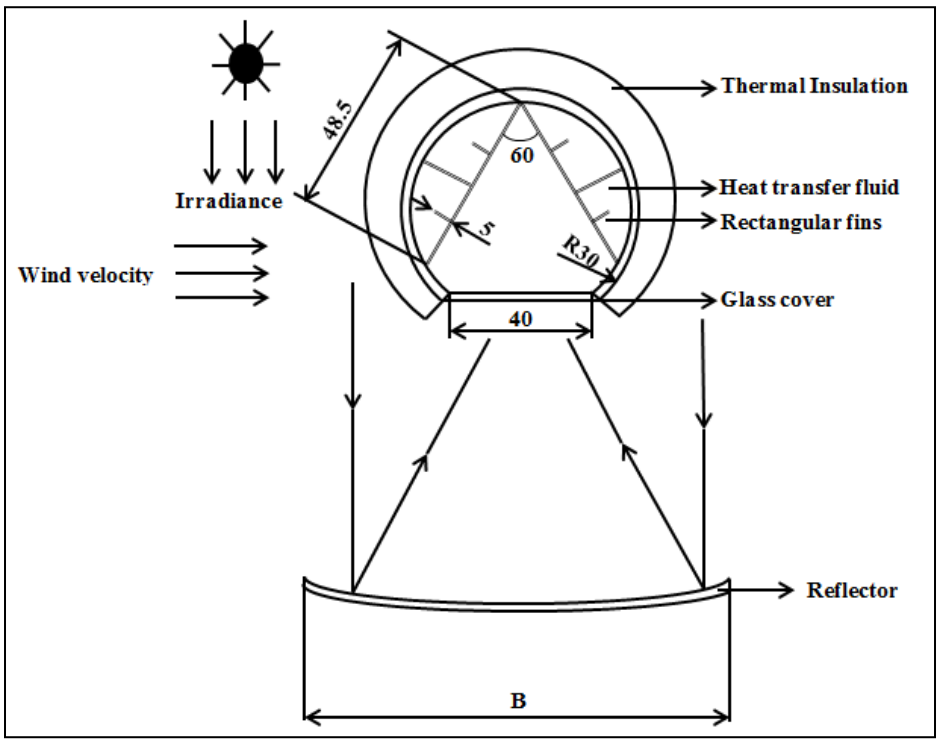

Figure 2-11: Schematic diagram of cavity absorber and concentrator model [95].

based on PTC). If owing to efficiency, PTC gives better values of energy (about 10.5-11% PTC vs. 7.6-8.1% FC). Giostri et al.[97] also compared PTC versus FC and found similar results as that of Cau and Cocco [96].

Investigation of wind flow analysis of PTC through CFD under real working conditions was analyzed by Hachicha et al. [98]. Lüpfert et al. [99] listed out optical performance analysis techniques for prototype evaluation of PTC. Some of the software tools that can be used in PTC are summarized here. Photogrammetric investigation was used to trace geometric properties of mirrors, modules and collector assemblies. High density photogrammetry data was used for ray-tracing studies on optical efficiency. It was also seen that flux mapping was the fastest method to check flux distribution on PTC in operating conditions. These techniques can be used to increase the collector quality during manufacturing and operation for the solar fields. Authors suggest to go for ray-tracing studies before practically implementing any design of PTC.

2.5.3 Central receiver system

In central receiver system (CRS), the solar radiation is redirected by two-axis tracking mirrored collector called heliostats. Solar energy is concentrated at a focal point on the top of a tower, where solar energy gets transferred to high temperature HTF by radiative/convective mechanism, shown in Figure 2-12. Operational temperature range of CRS is from 150-2000 ^{o}C with a minimum of 100 heliostats [3]. Several HTFs such as nitrate salts, liquid sodium, superheated steam and air were tested by European projects at Plataforma Solar de Almeria in Spain and in USA

[100]. Blackmon [101] conducted parametric analysis of heliostat cost per unit area. It was concluded that parametric analysis technique reduces cost of heliostats that includes (i) in-field wiring (ii) electronic cost (iii) field area of heliostat. Coelho et al. [102] worked on atmospheric air volumetric CRS, which shows better thermal performance and good economic indicator. Liquid sodium has low melting point (97.7 ^{o}C) and high boiling point (873 ^{o}C) which is a higher range of operational temperature [103]. But, it is expensive. Several designs have been put forward to obtain high temperature of CRS [104-107].

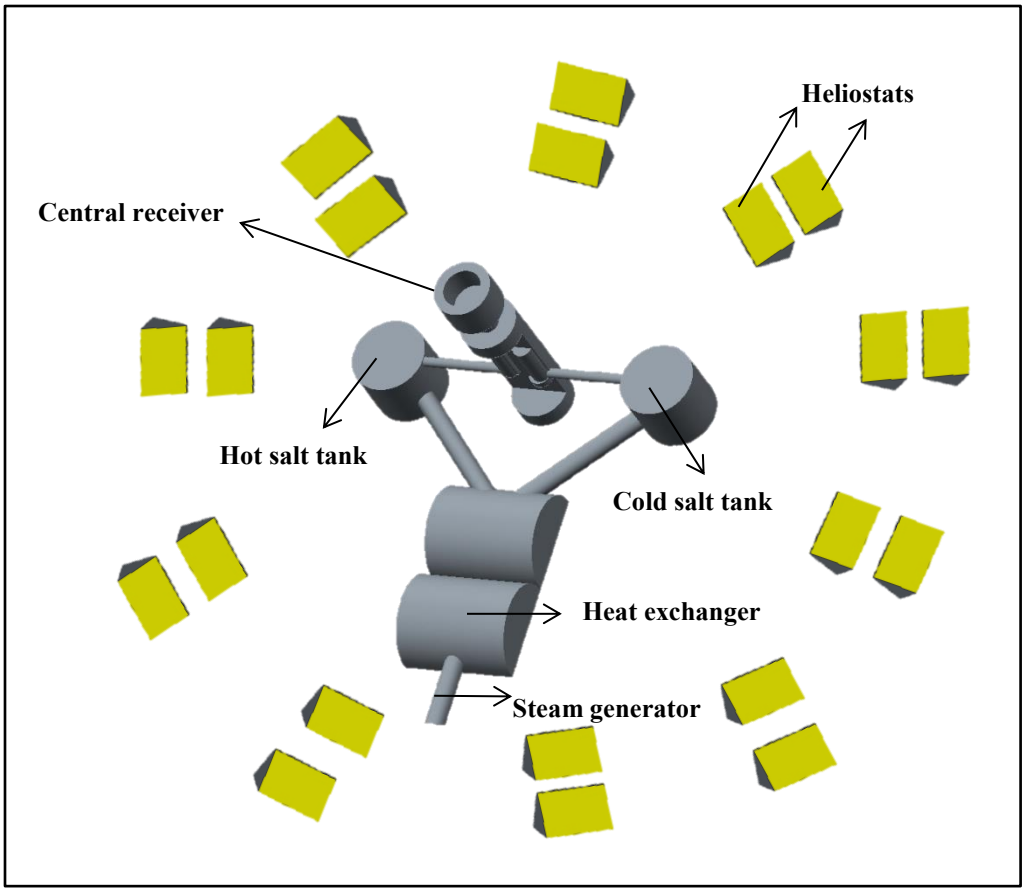

Figure 2-12: Central receiver system.

2.5.3.1 Enhancement through design and simulation

Abu-Hamdeh and Alnefaie [108] designed and constructed CRS for its applicability in Saudi Arabia. They used solar salt (60% $NaNO_3$ and 40% KNO_3) as HTF. It was found that the thermal power of water was measured as 11.26 kW. Percentage of error in thermal power was found to be as 5.3%. Liao and Faghri [109] proposed new concept of heat pipes in CRS as shown in Figure 2-13. The proposed design minimizes freezing of molten salt and enhances operating time of CRS. The CRS efficiency increases with increase in solar energy and decreases with flow passes. By the proposed design, they obtained thermal efficiency as 88.5%. Almsater et al. [110] worked on performance enhancement for CRS using heat pipes with fins. They found an enhancement of 106% in thermal energy storage in charging process than heat pipes without fins. This enhancement is because of fins, which extends thermal conductivity directly to the working fluid and also increases heat transfer area. Garcia et al. [111] listed out different types of modeling tools such as codes for receiver modeling, heliostat field layout for optimization and transient analysis which are necessary for design and analysis of CRS. Software tools for optimizing of CRS design are UHC-RCELL, (WIN) DELSOL and HFLCAL. Performance analysis of CRS through softwares can be done using MIR-VAL, UHC-NS or IH, FIAT-LUX and SOLTRACE techniques.

For performance enhancement of CRS many factors need to consider such as HTF, receiver design and heat exchanger. Ho and Iverson [112] discussed various receiver designs for performance enhancement of CRS. Berenguel et al. [113] developed and implemented an automatic offset correction system for heliostat field of CRS. By using offset correction technique, exact distance to be placed between heliostats and power tower can be known. Authors suggest going through software analysis (SOLTRACE, FIAT-LUX and etc.,) before going for installation.

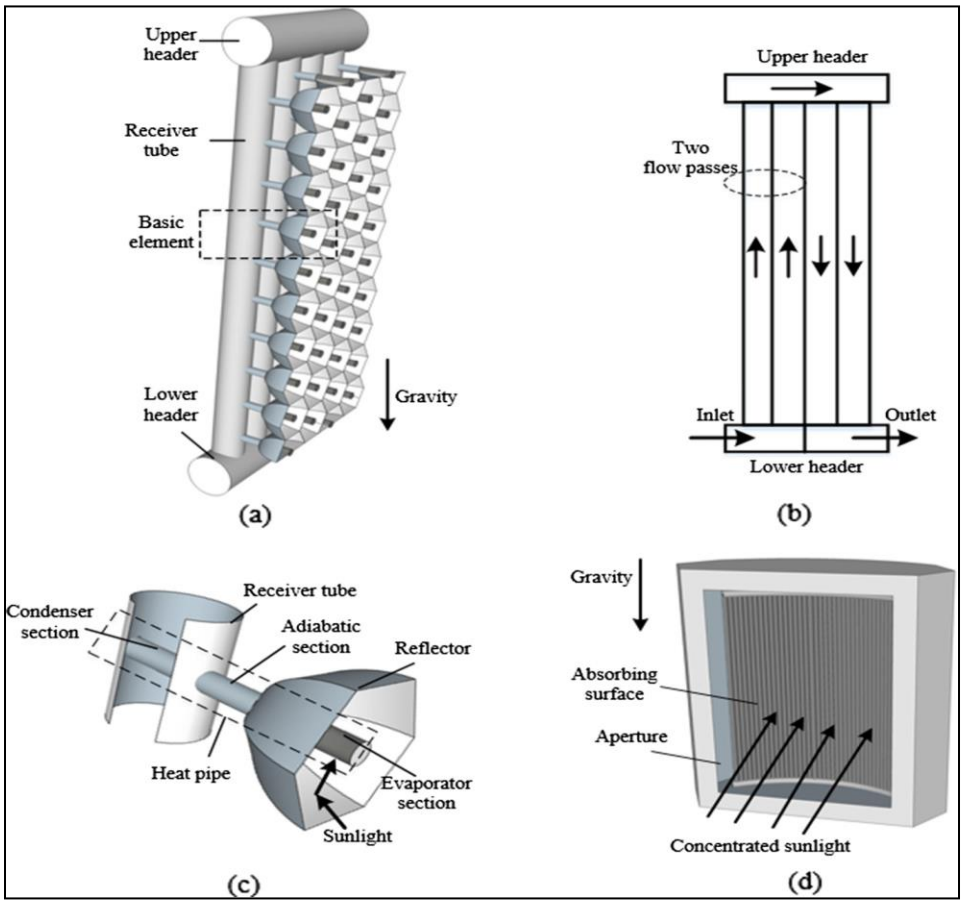

Figure 2-13: Heat pipes in CRS: (a) receiver panel, (b) 2-D receiver panel; (c) basic structure; (d) receiver of CRS [109].

2.6 Thermal energy storage materials

Thermal energy collected by solar collectors needs to be efficiently stored. Solar energy is available only during the day and its application requires efficient TES materials. So the excess thermal energy collected during day time may be stored for later use during the night [114]. The main important factors for TES material are (i) High thermal storage capacity, (ii) Low cost and low thermal energy loss (iii) High TC and (iv) Eco-friendly [115]. Classification of the substances used for TES is shown in Figure 2-14. The basic types of TES techniques are (i) Sensible heat storage, (ii) Latent heat storage and (iii) Chemical heat storage are described below.

2.6.1 Sensible heat storage

Sensible heat storage materials are capable of storing thermal energy without undergoing phase change of the storage medium. Charging of sensible heat storage system can be done through renewable source of energies such as solar energy. When energy demand increases, then thermal energy can be recovered from the storage system. So, it should have high SHC, high density, long term stability under thermal cycling, unaffected by contaminant and should have low cost [116]. Main characteristics of standard and most commonly used sensible heat storage materials are listed in Table 2-2. Sensible heat storage is divided into two types: i) Liquid storage media and ii) Solid storage media.

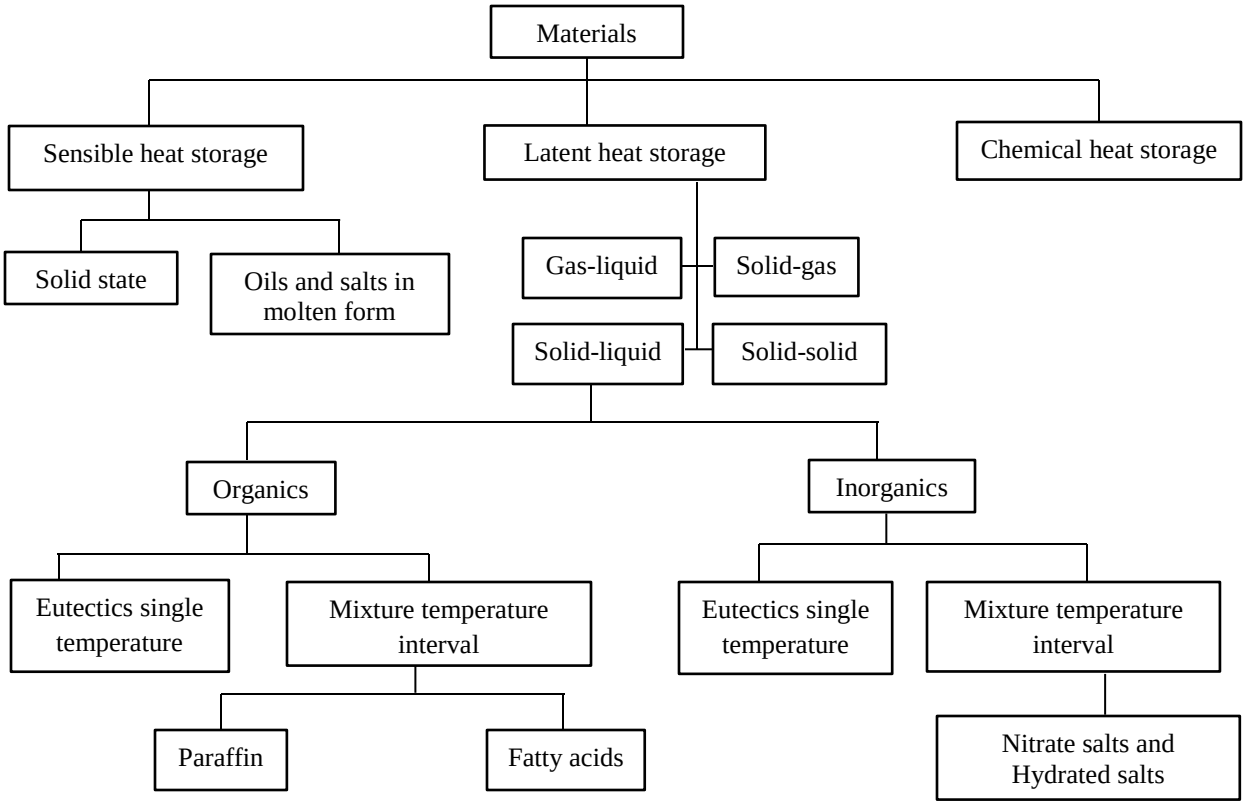

Figure 2-14: Classification of latent heat materials, with phase change solid-liquid [117, 118].

Table 2-2 Molten salts and high temperature oils [118, 119].

Storage materials	**Temperature range (°C)**	**Density (kg/m^3)**	**TC (W/(mK))**	**Specific heat (kJ/kg°C))**
Water	25-90	1000	0.58	4.2
Mineral oil	200-300	770	0.12	2.6
Synthetic oil	250-350	900	0.11	2.3
Silicone oil	300-400	900	0.10	2.1
Nitrite salts	250-450	1825	0.57	1.5
Liquid sodium	270-530	850	71.0	1.3
Nitrate salts	265-565	1870	0.52	1.6
Carbonate salts	450-850	2100	2.0	1.8

2.6.1.1 Liquid storage media

Water is the best storage medium at low temperature range of 25-90 ^{o}C. It is inexpensive, easily available and having higher specific heat [30, 120]. It can be directly used for washing, bathing and commonly used as heat transport media for thermal energy. When water is heated up to 90 ^{o}C, then it will store 81.7 kWh of energy. However, the main drawback of water as heat storage media is low TC in vapor state. Water storage tanks are made up of a wide variety of materials like steel, aluminum, reinforced concrete and fiber glass [121]. The other substitute for water are petroleum based oils, liquid sodium and molten salts. Masuda et al. [122] investigated enhancement in TC of nanofluids by dispersing Al_2O_3 nanoparticles of diameter 13 nm in water. They found that with dispersing 3 and 4.3 vol. % Al_2O_3 nanoparticles in water, TC got enhanced by 20% and 32.4%. Badran and Jubran [123] investigated thermal efficiency (TE) of flat plate collector (FPC) with oil as base fluid. It was concluded that TE of FPC with oil was 15–19 % lesser than normal water FPC. However, TE with flow of oil is 4–9 % higher than stagnant oil in FPC. Oils are temperature and age dependent and will start to degrade as the temperature increases beyond its limiting point. If oil vaporizes in closed container then air tightening will occur, which has to be avoided and oils are quite expensive than water [124]. With the advent of nano materials, it became possible to tailor thermal properties of liquid storage media is also presented and discussed.

2.6.1.1.1 Nanomaterials in liquid storage media

Nanofluid is a class of HTF obtained by dispersing nano-sized particles, fibers and tubes in the conventional base fluids such as water, EG and engine oil, etc. It was proposed by Choi [125] in 1995. Over the past few years, there has been great research interest in exploring the TC enhancement, effectiveness and feasibility of using nanofluid in various applications including as HTF. Effect of nano materials on TC depends on various parameters such as particle size, shape, material, volume fraction, type of fluid and temperature. An overview of all these parameters has been discussed by Philip and Shima [126] and Rashmi et al. [127]. In addition to these parameters Philip and Shima [126] also studied on effect of additives, acidity, sonication and aggregation of nano particle (NP) materials. Various TC measurement models were proposed depending on size and shapes [128-137].

Wang et al. [138] experimentally prepared stable graphene/1-hexyl-3-methylimidazolium tetrafluoroborate (GE/[HMIM][BF_4]) and multi walled carbon nanotube (MWCNT)/[HMIM][BF_4] ionanofluids and measured TC at various concentration ratios as shown in

Figure 2-15. It was found that by doping of 0.06% wt. GE, an enhancement of TC by 15.5% at 25 ^oC and 18.6% at 65 ^oC than the pure [HMIM][BF_4]. TC Enhancement may be due to high TC and Brownian motion of GE and MWCNT. Batmunkh et al. [139] prepared nanofluid by

doping of TiO_2 NP in water with three different concentrations: (i) 1 wt. %, (ii) 2 wt. % and (iii) 3 wt. % and then they mixed individually in three different solutions of 0.5 wt. % Ag NP. They obtained TC enhancement of nanofluid 0.5 wt. % Ag NP with concentration 1 wt. % TiO_2 from 601.4 to 609.5 mW/m.K, 2 wt. % TiO_2 from 606.6 to 611.3 mW/m.K and 3 wt. % TiO_2 from 608.9 to 615.7 mW/m.K at ambient temperature. The reason for TC enhancement is due to Ag NP possesses high TC and TiO_2 NP possesses temperature dependent TC. Applications of nanofluid for flat plate solar collector was experimentally investigated by Yousefi et al. [140] using Al_2O_3 NP. By dispersing 0.2 wt. % of Al_2O_3 NP in water, it was found that increase in TE by 28.3% compared to pure water. In another experiment, they added 0.021 wt. % triton X-100 to the mixture of 0.2 wt. % of Al_2O_3 NP and water as shown in Figure 2-16. It was concluded that there is increased in TE by 15.63% in triton X-100. In both cases, increase in TE is due to uniform dispersion of Al_2O_3 NP in the solution. Similarly, Yousefi et al. [141] made another attempt for increasing TE of FPC by addition of MWCNT. It was found that there is decrease in TE of FPC with the addition of 0.2 wt. % MWCNT in water. However, an increase in TE with the addition of 0.4 wt. % MWCNT was achieved. Yousefi et al. [142] also worked on TE of FPC with variation of pH in MWCNT dispersed in water by the addition of triton X-100 additive.

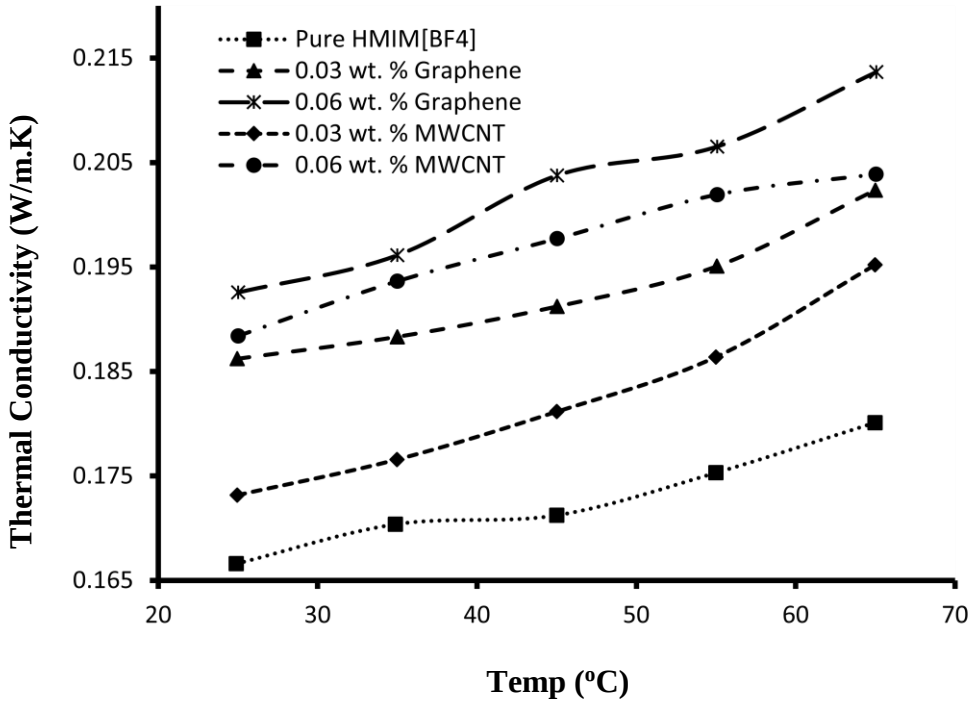

Figure 2-15: TC enhancement as a function of temperature [138].

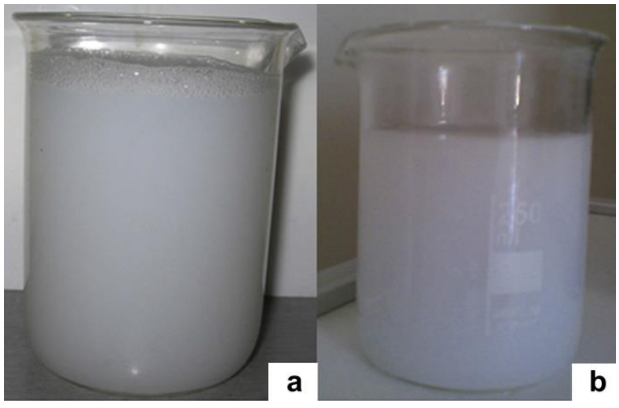

Figure 2-16: Photograph of Al_2O_3 nanofluid (a) with triton X-100 surfactant and (b) without triton X-100 surfactant [140].

It was concluded that the TE of FPC increased either with increasing of pH or with decreasing pH to values above and below neutral pH of nanofluid. At low pH values, less aggregation of MWCNT occur thus making a uniform dispersion solution. At high pH values, MWCNT forms highly stable colloidal solution.

Khullar et al. [143] experimentally and computationally compared the results of conventional concentrating parabolic solar collector (CPSC) and NP containing CPSC by maintaining similar external conditions. They doped 0.05% vol. fraction Al NP in therminol VP-1 and observed that nanofluid CPSC has 5-10% higher efficiency than conventional CPSC. Otanicar et al. [144] also reported improvement in TE of solar collector by doping of graphite NP, CNTs and Ag NP in water. Sani et al. [145] reported that enhancement of TE and reducing of cost by using EG as base fluid in solar thermal collector. They separately dispersed single walled carbon nanohorns (SWCNH) in EG and water and compared properties of both nanofluids. It was concluded that SWCNH in EG has more efficiency, cost effective and eco-friendly than water based SWCNH.

Das et al. [137] observed three important factors for TC enhancement in nanofluid: (i) smaller size of CuO NP posseses higher TC enhancement at same concentration, (ii) enhancement in TC by 2 to 4 folds with increase in temperature and (iii) TC increases with increasing concentration of Al_2O_3 NP. The behavior of increased TC for high concentration of NP in nanofluids may be due to average TC of solid particles and liquid solution.

Enhanced TC for increased operating temperature may be due increased stochastic motion of NP. Table 2-3 gives list of nanomaterials doped in base fluids for TC enhancement. Based on the reported literature, it was concluded that the doping of nanomaterials in base fluid(s) increases thermo-physical properties of base fluid especially TC.

Table 2-3 Nanomaterials doped in base fluids for TC enhancement [146].

Compound	**Melting Point (°C)**	**Nanomaterials**	**Increased TC efficiency**	**Reference**
Water	At 4 °C	5 vol.% CuO NP	60%	Eastman et al. [147]
[HMIM]BF_4	NA*	Graphene	15.5% at 25°C	Wang et al. [138]
	NA*		18.6% at 65°C	
Water	At 4 °C	3 vol.% Al_2O_3 NP	6.7%	Colangelo et al. [148]
Water	At 4 °C	0.1 g/l SWCNH	10%	Sani et al. [149]
Water		4.3 wt.% Al_2O_3 NP	32%	Masuda et al. [122]
		4.3 wt.% TiO_2 NP	11%	
Glycol	At 25 °C At 55 °C	0.5% mass fraction CNTs 4.0% mass fraction CNTs	18% 25.4%	Meng et al. [150]
[C_4mim][NTf_2]	At 25 °C	1 wt.% of MWCNT	35.54%	Nieto de Castro et al. [151]
[C_4mim][CF_3SO_3]	At 25 °C	1 wt. % MWCNT	9.44%	
[C_6mim][NTf_2]	At 25 °C	1 wt. % MWCNT	6.81%	
[C_8mim][NTf_2]	At 25 °C	1 wt. % MWCNT	6.62%	
[C_4mim][BF_4]	At 25 °C	1 wt. % MWCNT	6.13%	
70 vol. % de-ionized water – 30 vol.% ethylene glycol	At 40 °C	0.45 vol.% MWCNT	19.73%	Kumaresan and Velraj [152]
TiO_2–$BaCl_2$–H_2O	At 5 °C	1.13 vol. % TiO_2 NP	12.76%	He et al. [153]
[Bmim][PF_6]	At 33 °C	1.02×10^{-3} % vol. fraction Au NP	13.1%	Wang [154]
[C_4mim][NTf_2]	At 25 °C	1 wt. % Al_2O_3 NP	~6%	Paul et al. [10]
[C_4mpyrr][NTf_2])	At 25°C	1 wt. % Al_2O_3 NP	~5%	
silicone oil	At 60 °C	0.07 wt. % Functionalized graphene. GO with ethanol	18.9%	Ma et al. [155]
oil(LD320, heavy alkylbenzene)	NA*	1.36 vol. % graphite	36%	Wang et al. [156]
oil(LD320, heavy alkylbenzene)	NA*	0.68 vol. % graphite	11%	
DI water	At 4 °C	1 wt. % MWCNTs and 10 wt. % PMMA microencapsulated paraffin wax	8%	Zhang and Zhao [157]

*NA – Not Available

2.6.1.2 Solid Storage media

Solid TES materials such as sand, bricks, concrete, and rock etc., are used for both low and high temperature applications. The advantages of solid storage materials are inexpensive; it will not boil, freeze and also does not get leaked. However, the disadvantages are heat and moisture leads to microbial activity and requires high volume for storing thermal energy. Taheri et al. [158] immersed black colored sands in water. They designed solar collector in such a way that sand is prevented by galvanized plate in a way that sand will not get sunk in water. With this design, they got TE more than 70% with long life, less expensive and large storage capacity per volume. Effect of concrete size on TES was investigated by Adeyanju [159]. It was concluded that small concrete bed size of 0.065 m diameter has highest TES capacity. This is because of high pressure drop of hot air and low porosity. Ziada and Abdel Rahim [160] investigated and compared thermal analysis of various single layer and multilayer packed bed systems. It was concluded that multilayer with rock-steel-rock storage medium has highest thermal storage capacity followed by rock bed. Some of the standard solid heat storage materials are given in Table 2-4. However, the thermal properties of various solid storage media depend on various parameters such as size, shape, porosity and material.

Table 2-4 Solid-state sensible heat storage materials [118].

Storage materials	Temperature range (°C)	Density (kg/m^3)	TC (W/ mK)	Specific heat (kJ/kg°C)
Sand-rock minerals	200-300	1700	1.0	1.30
Reinforced concrete	200-400	2200	1.5	0.85
Cast iron	200-400	7200	37.0	0.56
NaCl	200-500	2160	7.0	0.85
Cast steel	200-700	7800	40.0	0.60
Silica fire bricks	200-700	1820	1.5	1.00
Magnesia fire bricks	200-1200	3000	5.0	1.15

2.6.2 Chemical heat storage

Energy can be stored in a chemical reaction, which can occur in both forward and reverse directions [4]. Endothermic energy can be used to form a product. Energy stored in a product can be regained by exothermic reaction under specific conditions. Thermochemical energy can be roughly presented as the following sequence.

1. During charging

$$A + B + thermal\ energy \rightarrow C + D \qquad \textbf{Eq. 2-1}$$

2. Reactants can store thermal energy for long duration
3. During discharging

$$C + D \rightarrow A + B + thermal\ energy \qquad \textbf{Eq. 2-2}$$

One of the simple examples is dissociation of Fe_3O_4. Steinfeld et al. [161] demonstrated that solar energy is sufficient to break Fe_3O_4 to

FeO and releases energy. When FeO reaches storage tank, comes in contact with H_2O at low temperature it will again form Fe_3O_4.

$$Fe_3O_4 + thermal\ energy \rightarrow 3FeO + \frac{1}{2}O_2 \qquad \textbf{Eq. 2-3}$$

Thermochemical looping of Fe_3O_4/FeO redox system was studied by Abanades et al. [162]

$$3FeO + H_2O \rightarrow Fe_3O_4 + H_2 \qquad \textbf{Eq. 2-4}$$

Xiao et al. [163] worked on numerous types of solar chemical reactors such as ZnO/Zn, Fe_3O_4/FeO, SnO_2/SnO, CeO_2/Ce_2O_3, GeO_2/GeO and MgO/Mg. However, chemical heat storage has not been extensively explored due to the limitations such as long term reversibility reaction, durability, chemical stability and complicated reactor for chemical reactions.

2.6.3 Latent Heat Storage

Latent heat storage (LHS) has attracted a large number of researchers, since it provides several advantages compared to liquid and solid storage media. Generally, LHS has low capital cost, higher storage density and low energy losses to the surroundings. However, the main drawbacks of LHS materials are corrosive to metallic walls and their phase segregation could result in supercooling [164]. Hasnain [119] described that LHS system must possess three basic things. They are a) solid-liquid phase change in the required temperature range, b) Storage containment system and c) Heat exchange mechanism for energy transfer. Development of

latent heat TES system involves two essential subjects: phase change materials (PCM) and heat exchanger. PCM storage systems have the advantage that they operate with small temperature differences between charging and discharging as shown in Figure 2-17.

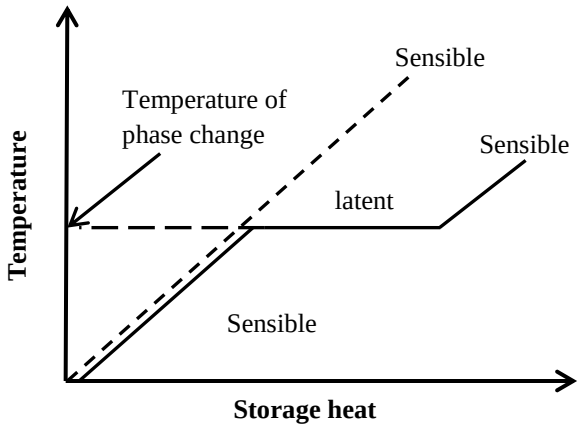

Figure 2-17: Phase change profile of PCM [165].

2.6.3.1 Phase Change Materials (PCM)

There are various phase transitions taking place during material heating. They are solid-liquid, liquid-vapor and solid-solid phase transition. PCM to be used as energy storage material must possess high TC, large latent heat of fusion, thermal cycling stability, high SHC and cost [166]. PCM materials that have been studied during the last 20 years are hydrated salts, paraffin waxes, fatty acids and eutectics of organic and inorganic compounds [117]. Depending on the application, PCMs should be selected. A detailed review on organic and inorganic PCM with low/high melting point, TC, phase segregation and cost is done by Farid et al. [167]

The amount of energy stored in a PCM while undergoing solid-liquid phase change is given [168] by;

$$Q = m\int_{T_i}^{T_m} mC_p dT + ma_m \Delta H_m + m\int_{T_m}^{T_f} mC_p dT \qquad \textbf{Eq. 2-5}$$

Where m is mass of PCM, Cp is SHC of solid and liquid transitions respectively, a_m is fraction melted, ΔH_m is enthalpy, Ti, T_m and T_f are initial, melting and final temperatures of PCM. In inorganic and organic PCM, we have discussed about molten salts and paraffins.

2.6.3.1.1 Molten salts

Solar thermal plants, which depends on solar energy to produce steam or electricity uses molten salt as HTF or TES. These plant uses nitrate based melts that operate at temperature below 550 ^oC [169]. Eutectic behavior is common in binary mixture of salts and can be even more dramatic with higher order mixtures. Main advantages of inorganic eutectic mixtures are high latent heat capacity, high TC, non-flammable and commercially available. However, the disadvantages of inorganic eutectic mixtures are corrosive, supercooling and phase segregation [164]. An example of a simple binary salt is mixture of $NaNO_3$ and KNO_3. $NaNO_3$ melting point is at 307^oC and KNO_3 melting point is at 337 ^oC. The mixture of 46 mol. % $NaNO_3$ and 54 mol. % KNO_3 has eutectic point at 222 ^oC which exhibits reduced melting point. Moreover, presence of water molecules in

eutectic mixture (see Table 2-5) will not affect the chemical stability. Some of the standard eutectic HTFs is given in Table 2-5.

Table 2-5: List of Standard eutectic behavior HTF [117].

Standard HTF	Molar Composition (mol)	Melting point (°C)	Density (Kg/m^3) at 300°C	Viscosity (cP) at 300°C	SHC (J/Kg.K) at 300°C	TC (W/mK)
HITEC XL	7% $NaNO_3$, 45% KNO_3 & 48% $CaNO_3$	140	1992	6.37	1447	0.519(at 300°C)
HITEC Salt	7% $NaNO_3$, 53% KNO_3 & 40% $NaNO_2$	142	1640	3.16	1560	0.61 (at 350°C)
Solar Salt	60% $NaNO_3$ & 40% KNO_3	240	1899	3.26	1495	0.536
Dowtherm A	Diphenyl Biphenyl Oxide	12	815	0.2	2319	0.098479 (at 304°C)

Coscia et al. [170] derived mathematical model for predicting eutectic behavior of binary and ternary salts. They developed mathematical model using Gibbs free energy in MATLAB and compared with the experimental results from DSC. The results show the mathematical model and experimental results were in good agreement.

Raade and Padowitz [171] explored over 5000 mixtures of inorganic salts to produce a novel mixture having low melting point and high thermal stability. They used 250 mg salt mixture of quantity: 18.6 mg of $LiNO_3$, 14.4 mg of $NaNO_3$, 54.3 mg of KNO_3, 102.7 mg of $CsNO_3$, and 62.1 mg of $Ca(NO_3)_2.4H_2O$. This mixture of salt exhibits unique eutectic behavior resulting in a low melting point of 65 °C and thermal stability limit over 500 °C. Such mixture can be used in different types of solar collectors and other high temperature process.

Gheribi et al. [172] proposed a model based on thermo-physical properties of salts for prediction of TC of molten salts. The proposed model is in good agreement with experimental data of nitrates, carbonates, halides, sulfates and hydroxides. However, the proposed model showed low predictive accuracy of 20%. Foong et al. [173] studied thermal behavior of solar salt using COMSOL multiphysics software. They showed variation of TC at constant heat radiation of 10 kW/m^2 on number of fins. In their report, it was concluded that with increase in number of fins, there is decrease in melting time of solar salt.

Daolin and Tianlong [174] prepared three novel inorganic PCMs for TES: (i) PCM-A composite having 50% anhydrous $CaCl_2$ and 50% doubly deionized water, to this solution 5% $Mg(NO_3)_2.6H_2O$ is added and stirred till the solution becomes homogeneous. PCM-A with phase change temperature of 22.6 ^oC and latent heat value of more than 160 kJ/kg, (ii) PCM-B composite comprises of 61.2% $Mg(NO_3)_2.6H_2O$ mixed with 38.8% NH_4NO_3 with phase change temperature of 44.8 ^oC and latent heat values of about 155 kJ/Kg and (iii) PCM-C having 86% $Mg(NO_3)_2.6H_2O$ blended 14% blended $LiNO_3$ with phase change temperature of 72.1^oC with latent heat values of more than 165 kJ/Kg.

Gomez et al. [175] varied the composition of $NaNO_3$, KNO_3 and $Ca(NO_3)_2$ to obtain low melting point molten salt. They showed that best composition having low solidification point would be 36 wt. % $Ca(NO_3)_2$, 16 wt. % $NaNO_3$ and 48 wt. % KNO_3. DSC test showed the ternary salt

having eutectic behavior of around 100 ºC. Several published papers have described about low melting point of eutectic mixture as shown is Table 2-6. With the addition of nano materials in molten salts, SHC of molten salts got enhanced are also discussed.

Table 2-6: Recently developed eutectic mixture salts with low melting point

Salts	Percentage of composition	Melting point (ºC)	Thermal stability (ºC)	Reference
$Ca(NO_3)_2$, $NaNO_3$, KNO_3	36–16–48 wt. %	100	>500	Gomez et al. [175]
$LiNO_3$, $NaNO_3$, KNO_3, $CsNO_3$, $Ca(NO_3)_2.4H_2O$	18.6–14.4–54.3–102.7–62.1 mg	65	500	Raade and Padowitz [171]
Li+, K+, and Na+ with a 0.56 ratio of nitrate/nitrite	30–50–20 mol. %	72	500	Cordaro et al. [176]
$CaCl_2$ solution–DI water mixed with $Mg(NO_3)_2.6H_2O$	50 %–50 %–5 vol. %	22.6	NA*	Gao and Deng [174]
$Mg(NO_3)_2.6H_2O$, NH_4NO_3	61.2 – 38.8 mass %	44.8	NA*	Gao and Deng [174]
$Mg(NO_3)_2.6H_2O$, $LiNO_3$	86 % – 14 mass %	72.1	NA*	Gao and Deng [174]
Li_2CO_3, Na_2CO_3, K_2CO_3	32.1–33.4–34.5 wt. %	405	NA*	Olivares et al. [177]
KNO_3:$NaNO_3$:$LiNO_3$:$Ca(NO_3)_2.4H_2O$	mass ratio 5:2:1:2	84.3	NA*	Ren et al. [178]
	5:1:1:2	79.0	NA*	Ren et al. [178]
	6:1:2:2	85.4	NA*	Ren et al. [178]
	5:1:2:2	82.2	NA*	Ren et al. [178]
	6:1:1:2	80.4	NA*	Ren et al. [178]
$LiNO_3$, KCl	1:1 molar ratio	170	NA*	Huang et al. [179]
$LiNO_3$, $NaNO_3$, KNO_3, $NaNO_2$	17.5–14.2–50.5 –17.8 wt. %	119.17 (392.17K)	NA*	Wang et al. [180]
KNO3, $Ca(NO_3)_2$, $LiNO_3$	67.2–19.3–13.5 wt. %	78,	542	Zhao and Wu [181]
	64.8–24.8–10.4 wt. %	80,	542	Zhao and Wu [181]
	63.7–27.3–9.0 wt. %	76	542	Zhao and Wu [181]

*NA – Not Available

2.6.3.1.1.1 Nanomaterials in Molten Salts

As discussed in section 2.6.1.1.1, the addition of nanomaterials will enhance thermo-physical properties of base fluids. Nanomaterials are promising materials that can increase TC and SHC of molten salts as it has successfully increased TC of base fluids as listed in Table 2-3. However, very few works have been reported on doping of nanomaterials in molten salts. Table 2-7 summarizes increase in SHC with addition of nanomaterials when compared to SHC of pure molten salts. In Table 2-7, all the authors measured SHC of nanomaterial doped molten salts when they are in molten state. Only Jo and Banerjee [182] measured SHC both in solid state and in molten state. Shin and Banerjee [183] proposed three models for higher SHC. Model-I was proposed by taking theoretical model of Wang et al. [184] and Wang et al. [185], showed enhanced SHC because of high surface area or energy of NPs. Model – II: enhanced SHC is due to interactions between NP and molten salts. Model – III: the layer of semi-solid molecules is expected to have higher SHC due to the reduced inter-molecular spacing and semi-solid behavior of that layer. Besides working on enhanced SHC, Jo and Banerjee [182] also worked on methods of synthesizing nanograhite for enhancement of specific heat. It was concluded that besides the uniformity of NP dispersion, synthesis method having short duration for dehydration will have higher level of enhanced SHC.

Lai et al. [186] and Ho and Pan [187] both used HITEC salt. Lai et al. [186] doped three different weight concentration of Sn/SiO_2 core shell NP. They are 1 wt. %, 3 wt. % and 5 wt. % and observed highest heat capacity enhancement of 30% at 5 wt. % of Sn/SiO_2 core shell NP as shown in Figure 2-18. The increase in heat capacity is possibly due to release of high latent heat of Sn NPs at melting point. Ho and Pan [187] experimentally investigated maximum SHC enhancement with optimum concentration of Al_2O_3 NP in HITEC salt. They obtained highest SHC enhancement of 19.9% by doping 0.063 wt. % of Al_2O_3 NP. The possible reason for decrease in SHC with increase in concentration may be due to negative effect on SHC of Al_2O_3 NP.

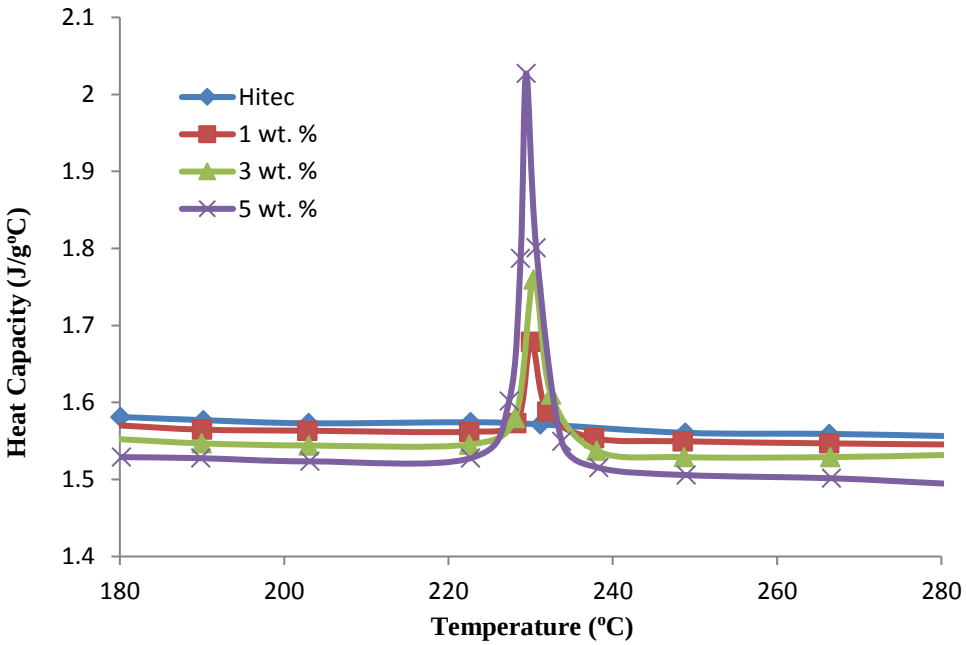

Figure 2-18: Heat capacity of HITEC salt with different concentration of Sn/SiO_2 NPs [186].

Tiznobaik and Shin [188] and Jo & Banerjee [182] both used Li_2CO_3:K_2CO_3 (62:38 molar ratio) eutectic mixture doped with different nanomaterials. By doping SiO_2 NP in Li_2CO_3:K_2CO_3 (62:38 molar ratio), Tiznobaik and Shin [188] obtained specific heat enhancement of 25% and by doping graphite NP Jo and Banerjee [182] observed 57% SHC enhancement, respectively. Dudda and Shin [189] reported an increase in SHC with increasing size of SiO_2 NP in solar salt. They doped four different sizes of SiO_2 NP by maintaining identical concentration of 1 wt. % in solar salt. They are 5 nm, 10 nm, 30 nm and 60nm and obtained SHC enhancement of 8%, 12%, 19% and 27% respectively. This is possibly due to increase of surface area and uniform distribution of SiO_2 NP. The scanning electron microscope (SEM) image of solar salt dispersed with 60 nm SiO_2 NP as shown in Figure 2-19, which shows a uniform distribution of SiO_2 NP. Another attempt was made by Andreu-Cabedo et al. [190] for increasing SHC of solar salt by doping 1 wt. % SiO_2 NP and they observed SHC enhancement by 25.03%. This discrepancy of result with other researchers in SHC enhancement may due to size of SiO_2 NP.

Chieruzzi et al. [191] doped various NP in solar salt such as SiO_2, Al_2O_3 TiO_2 and a mixture of SiO_2-Al_2O_3 with 3 different concentrations (0.5, 1.0 and 1.5 wt. %). From above mixtures, the highest SHC enhancement was observed by using mixture of SiO_2-Al_2O_3 NP of 1 wt. %. Further, it was reported that SHC enhancement of 57% (solid phase) and 22% (liquid phase). It was also observed there is decrease in melting point by more

than 8 ^{o}C. This enhancement may be due to formation of nano layer of SiO_2-Al_2O_3 NP. Still the research on doping of nanomaterials in molten salts is in infancy stage, more work has to be done on: i) Effect of nanomaterial, NP size, shape, concentration of nanomaterial, types of molten salts and operating temperature for enhancing SHC, ii) Long term stability of nanomaterials and iii) Compatibility with piping elements.

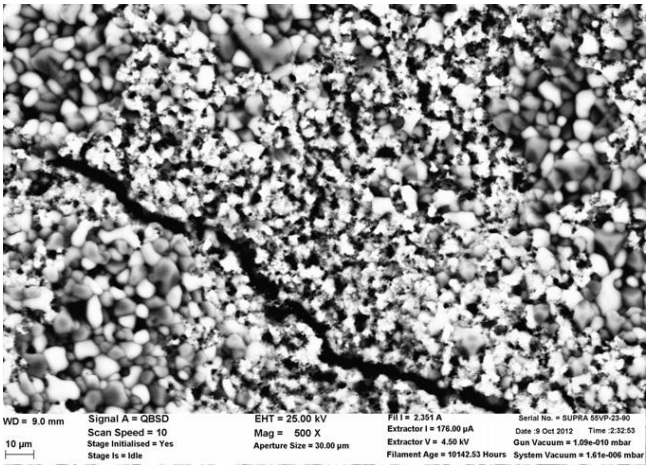

Figure 2-19: SEM image of pure eutectic salt with 60nm SiO_2 NP [189]

Table 2-7: Nanomaterials doped in eutectic salts [146].

Author and Reference	**Eutectic salts**	**Type of Nanomaterials used**	**Size of nanomaterial**	**Amount of Nanomaterial used**	**SHC enhancement**
Tiznobaik and Shin [188]	Li_2CO_3:K_2CO_3 (62:38 molar ratio)	Silica	~5nm	1 wt. %	25%
Lai et al. [186]	HITEC Salt	Sn/SiO_2 core shell NP	NA*	5% wt.	30%
Shin and Banerjee [183]	68.490 mg $BaCl_2$, 24.784 mg NaCl, 79.206 mg CaCl, 25.520 mg LiCl and 2 mg SiO_2	Silica	~20-30 nm	1% mass conc.	14.5%
Dudda and	Solar salt	Silica	5nm	1 wt. %	8%

Shin [189]			10nm	1 wt. %	12%
			30nm	1 wt. %	19%
			60nm	1 wt. %	27%
Ho and Pan [187]	HITEC Salt	Al_2O_3	<50nm	0.063 wt. %	19.9%
Jo and Banerjee [182]	Li_2CO_3:K_2CO_3 (62:38 molar ratio)	Graphite NP	NA*	0.1 wt. %	40% solid phase 57% liquid phase
Chieruzzi et al. [191]	Solar salt	SiO_2-Al_2O_3	NA*	1.0 wt. %	57% solid phase 22% liquid phase
Andreu-cabedo et al. [190]	Solar salt	Silica	NA*	1.0 wt. %	25.03%

NA* – Not Available

2.7 Theoretical Models for estimating various parameters

There are few theoretical models proposed for enhanced HC. Critical analysis of HC models was performed by Khanafer et al. [192]. Various models have been presented for predicting HC of nanofluids [193]. Theoretical model described in Eq. 2-6 is based on thermal equilibrium equation between particle and base fluid [194].

$$C_{p,nf} = \frac{\rho_{np}\phi_{np}C_{p,np}+\rho_f\phi_f C_{p,f}}{\rho_{np}\phi_{np}+\rho_f\phi_f} \quad \textbf{Eq. 2-5}$$

Where ρ_{np} and ρ_f are densities of nanoparticle and base fluid. ϕ_{np} and ϕ_f are volume fractions of nanoparticle and base fluid while $C_{p,nf}$, $C_{p,f}$ and $C_{p,np}$ are HC of nanofluid, base fluid and nanoparticle, respectively.

Dispersion of 5 vol. % CuO nanoparticle in water enhances TC by 60% [147]. Another study reports 0.5% mass fraction of carbon nanotube (CNT) dispersed in glycol shows 18% enhancement in TC [150]. Many theories have been proposed to explain this anomalous enhancement in TC

such as Brownian motion, nanoparticle clustering, uniform dispersion, liquid layer around nanoparticles and so on [195, 196]. Theoretical analysis for predicting enhanced TC has been done here by using Maxwell, Hamilton-Crosser and Nan's models.

$$k_{eff} = \frac{K_p + 2K_b + 2(K_p - K_b)\phi}{K_p + 2K_b - (K_p - K_b)\phi} K_b$$

Eq. 2-6 and

$$K_{eff} = \frac{K_p + (n_s - 1)K_f - (n_s - 1)\phi(K_f - K_p)}{K_p + (n_s - 1)K_f + \phi(K_f - K_p)} \mathbf{Kf} \qquad \text{Eq. 2-7}$$

represents Maxwell and Hamilton-Crosser model.

$$k_{eff} = \frac{K_p + 2K_b + 2(K_p - K_b)\phi}{K_p + 2K_b - (K_p - K_b)\phi} K_b \qquad \textbf{Eq. 2-6}$$

Where K_p and K_b are TC of nanoparticle and base fluid, respectively. ϕ is volume fraction of nanoparticle and K_{eff} is effective TC [197]. Hamilton-Crosser model is a traditional model for predicting TC of heterogeneous solutions [128].

$$K_{eff} = \frac{K_p + (n_s - 1)K_f - (n_s - 1)\phi(K_f - K_p)}{K_p + (n_s - 1)K_f + \phi(K_f - K_p)} K_f \qquad \textbf{Eq. 2-7}$$

Where K_p, K_f and K_{eff} are TC of nanoparticle, base fluid and effective, respectively. n_s is shape factor and ϕ is nanoparticle volume fraction.

In analyzing thermal behavior of heterogeneous solution, Nan et al. [133] developed new model for measuring effective TC of nanofluids as shown in Eq. 2-9 and Eq. 2-10.

$$K_{eff} = \frac{3+\phi[2\beta_{11}(1-L_{11})+\beta_{33}(1-L_{33})]}{3-\phi(2\beta_{11}L_{11}+\beta_{33}L_{33})} \quad \textbf{Eq. 2-8}$$

$$\beta_{ii} = \frac{K_p-K_{bf}}{K_{bf}+L_{ii}(K_p-K_{bf})} \quad \textbf{Eq. 2-9}$$

Where K_{eff} is effective TC. L_{ii} is aspect ratio of GE and K_p and K_{bf} represents TC of nanoparticle and base fluid, respectively.

Various theoretical models for predicting enhanced viscosity with dispersion of nano materials in base fluid was presented by Sundar et al. [198]. Einstein has developed a viscosity correlation as given in Eq. 2-11.

$$\mu_{nf} = \mu_{bf}(1 + 2.5\phi) \quad \textbf{Eq. 2-10}$$

Where ϕ is concentration of nano material and μ_{nf}, μ_{bf} are viscosities of nano fluid and base fluid, respectively [199]. Here Einstein's theoretical model of viscosity was selected for predicting of experimental results as the equation takes into consideration of base fluid viscosity and particle concentration.

2.8 Overview of Corrosion property

It is also very important to know the chemical interactions between molten salt and piping system. As molten salt might corrode the metal in which it is flowing. Thus, decrease in lifetime of containing material. Also, molten salt gets contaminated with corroded material which will affect its thermal properties. Soleimani et al. [200] performed corrosion resistance test on two ferritic steels, two austenitic steels and SS347H and Nickel alloy

IN625 in solar salt. Corrosion test was conducted in a furnace at 600 ^{o}C. All samples were immersed in binary salt with immersion time of 5000 h. Corrosion behavior were observed by recording weight loss of all steel samples. It was concluded that among all samples, IN625 showed best corrosion resistant property than other alloys. Fuzieah subari et al. [201] investigated corrosion property of SS316L on 15 different compositions of NaCl, KNO_3, $LiNO_3$ and $NaNO_3$. It was concluded that corrosion of SS316L in molten salt solution is due to presence of NaCl. Kruizenga [202] investigated corrosion test of solar salt on stainless steels specifically on 321SS and 347SS grades. It was concluded that corrosion rate is mainly dependent on temperature, because of Arrhenius behavior of containing material. They found that 347SS grade gets corroded 30-40% less than 321SS. This is due to spallation of corrosion in 321SS grade. Federsel et al. [203] investigated corrosion of steel 1.4541 using HITEC salt (7 wt. % $NaNO_3$, 53 wt. % KNO_3 and 40 wt. % $NaNO_2$) mixed with Cl < 100 ppm. It was concluded that low chloride concentration plays an important role in decreasing corrosivity of steel.

2.9 Summary

Previous studies clearly demonstrates the enhancement in thermo-physical properties with dispersion of nanomaterials in medium-high temperatures molten salt [204]. Andreu-cabedo et al. [190] dispersed silica (1 wt. %)

nanoparticles in solar salt (60 wt. % $NaNO_3$ and 40 wt. % KNO_3) and reported 25.03% enhancement in specific HC. Li et al. [186] obtained 30% enhancement in specific HC using HITEC salt (7 wt. % $NaNO_3$, 40 wt. % $NaNO_2$ and 53 wt. % KNO_3) by dispersing Sn/SiO_2 (5 wt. %) core shell nanoparticle. Jo and Banerjee [182] claimed 40% (solid phase) & 57% (liquid phase) enhanced specific HC by dispersing GE (0.1 wt. %) in binary carbonate salts (62:38 Li_2CO_3:K_2CO_3 by molar ratio). Thus, it is very evident that by dispersing nanomaterials in molten salts, thermal energy per unit volume can be increased significantly.

Ahmed et al. [146] reported that enhancement in thermal properties are obtained by dispersing nanomaterials in molten salt. These properties are significantly dependent on viscosity of TES material. Therefore, development of TES material requires in-depth investigation of its properties that account for its entire enhancement. It is obvious that enhancement in viscosity depends on many factors such as (i) type of nanomaterials, (ii) size, (iii) shape, (iv) concentration, (v) base fluid, (vi) pH, (vii) temperature and (viii) shear rate [198, 205, 206].

2.10 Conclusion

Based on the study, some of the important criteria are identified for enhancement of thermal properties by doping on nanomaterials in TES materials:

(a) TC depends on various parameters such as particle size, shape, material, volume fraction, type of fluid and temperature.

(b) Surfactants, additives and pH manipulation contribute significantly towards the stability of NP in base fluids and hence leading to higher TC of TES material.

(c) PCMs offer an alternative solution in TES by using a similar heat transfer infrastructure. Experimental studies showed that with the optimum amount of NP, PCMs have the potential of providing a more efficient means of storage.

(d) SHC enhancement with trace amounts of NP was observed in different TES materials. However, the results were not conclusive as the doping of nanomaterials in TES is still in its infancy stage and future work should focus considering: i) Effect of nanomaterial, NP size, shape, concentration of nanomaterial, types of TES and operating temperature for enhancing SHC, ii) Long term stability of nanomaterials and iii) Compatibility with construction material.

(e) Experimental and numerical studies for solar collectors showed that in some cases, the efficiency could increase remarkably by using TES material doped with NP. It was suggested that the TES material doped with varying volume fractions of NP should be tested to find the optimum volume fraction.

(f) Many theories and mechanisms were proposed for enhanced thermo-physical properties of NP doped in TES. Moreover, due to inconsistency and discrepancies in the reported data, it is required to conduct more experiments to study all the factors responsible for enhancement in thermo-physical properties of TES materials with addition of NP. there are many challenges (or reasons for the inconsistency) associated with NP such as agglomeration, time-dependent segregation, degradation, optimum concentration and cost with TES materials in large scale applications.

CHAPTER – 3

EXPERIMENTAL PROCEDURE

3.1 Introduction

In this chapter, various materials and methodology used has been stated. Sample preparation of molten salt and nanosuspension has been discussed in flow chart. Figure 3-1 gives schematic representation of sample preparation and characterization used.

3.2 Materials

Nitrate salts ($NaNO_3$, KNO_3, $LiNO_3$, $CsNO_3$ and $CaNO_3.4H_2O$) were procured from Sigma Aldrich, Germany. Flow chart of research activity is given in Figure 3-1. Multilayered GE sheets of size 60 nm and MWCNT were purchased from graphene supermarket, USA. Al_2O_3 NP was purchased from Sigma Aldrich, Germany. Each salt was mixed in appropriate ratio to synthesize ~10 gm of molten salt as shown in Table 3-1 below [207]. The resultant eutectic molten salt was dissolved in 50 ml of deionized water with continuous stirring until all the salts gets completely dissolved. Various different concentrations of solutions were prepared by mixing different wt. % of GE, GE oxide, Al_2O_3 and etc. They are 0.01, 0.05, 0.1, 1, 3 and 5 wt. %. For 10 gms of eutectic mixture, 0.001, 0.005, 0.01, 0.1, 0.3 and 0.5 gms of nanomaterials for 0.01, 0.05, 0.1, 1, 3, and 5 wt. %, respectively were dispersed.

Functionalization of Graphene: The graphene powders were first functionalized using Simplified Hummer's method. A total net mass of 0.8 g of graphene was weighed and was added into a solution of containing

strong oxidizing agent namely sulphuric acid, H_2SO_4 and phosphoric acid, H_3PO_4. The acids were prepared at a ratio of 4:1 whereby 320 ml of sulphuric acid and 80 ml of phosphoric acid was measured. As soon as the graphene was added into the acid, 18 gm of potassium permanganate ($KMnO_4$) were gradually added into the mixture. The mixture was left to stir for 3 days. The oxidization process comes to a halt when the addition of 300 ml of deionized water and 50 ml of hydrogen peroxide, H_2O_2. Upon adding hydrogen peroxide, the brown suspension turns bright yellow. Next with a ratio of 1:10 hydrochloric acid, HCl and deionized water were added into the suspension. The suspension was the filtered using filter paper to isolate the paste samples from the remaining solution. The paste collected from the filter paper was then dissolved in deionized water. The suspension was washed for 5 – 7 times until its pH value becomes 7. To ease this step a few drops of sodium hydroxide, NaOH was added to fasten the neutralization process. The suspension was further filtered and the paste on the filter paper was collected and was kept in a petri dish. Finally, the collected sample was put into an oven operating at 60°C until the sample becomes completely dry.

Flow Chart of Research Activities

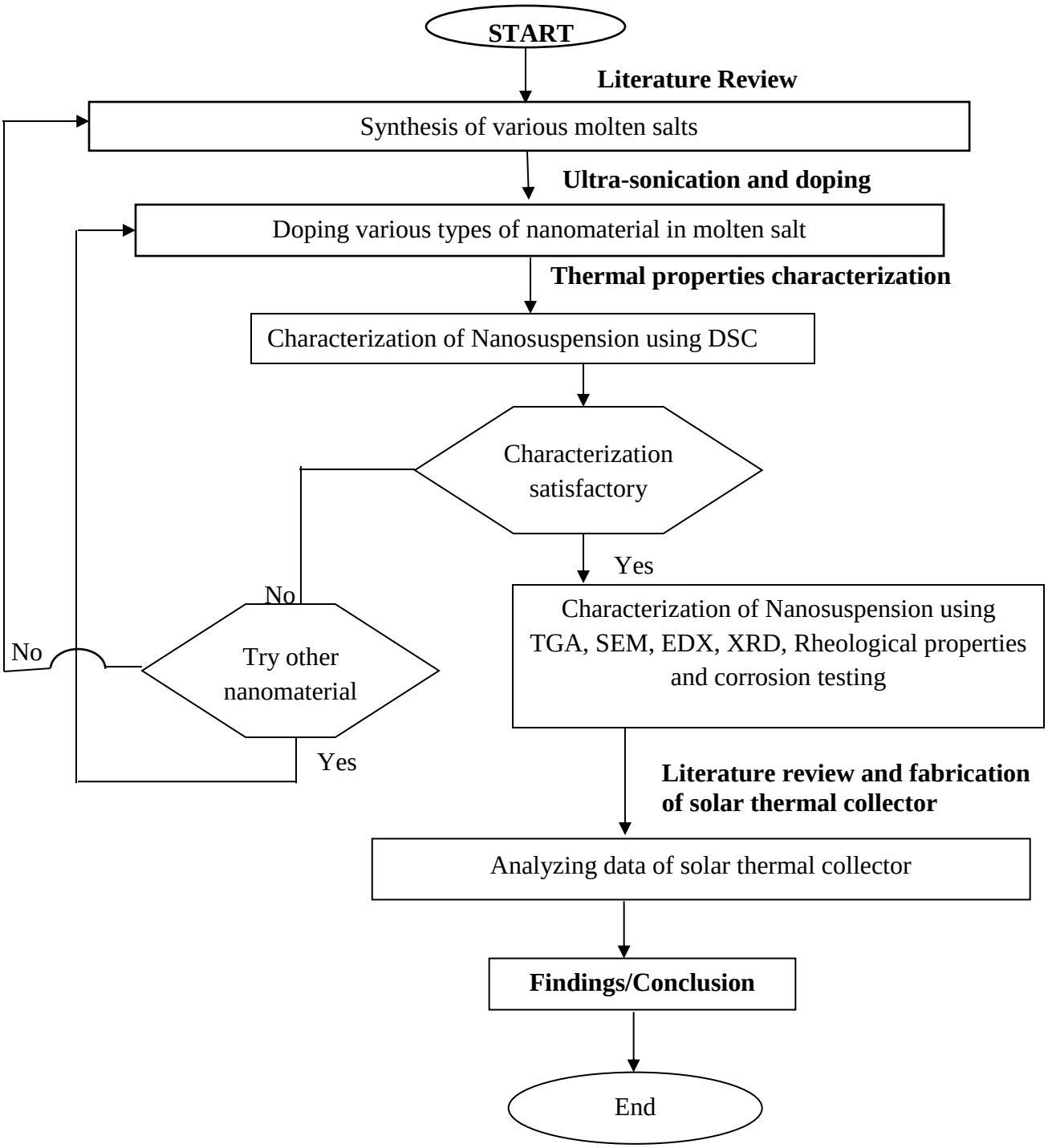

Figure 3-1: Flowchart of research activities

Synthesis of low temperature molten salt doped with GE, f-GE, MWCNT, Al_2O_3 NP, SWCNT, fullerene and Cu NP. Three different weight concentrations of GE, f-grpahene, MWCNT, Al_2O_3 NP, SWCNT, fullerene and Cu NP are selected. They are (i) 0.01 wt. %, (ii) 0.05 wt. % and (iii) 0.1 wt. %. Synthesis procedure is shown in flow chart Figure 3-2.

Nanosuspensions were prepared by dispersing 0.01, 0.05 and 0.1 wt. % GE to eutectic molten salt.

- Same procedure is followed for functionalized GE, f-GE, SWCNT, Al_2O_3 NP, Cu NP, MWCNT and fullerene.

GE nanosuspensions were ultra-sonicated using UP400S hielscher ultrasound technology for 3 hours with 5 mins interval after every half an hour of sonication. Amplitude and sweep cycle was maintained at 50% and 5 sec, respectively [208].

Table 3-1: Mass composition of nitrate salts

Salt	Amount (g)
$NaNO_3$	0.576
KNO_3	2.136
$LiNO_3$	0.744
$CsNO_3$	4.108
$CaNO_3.4H_2O$	2.484

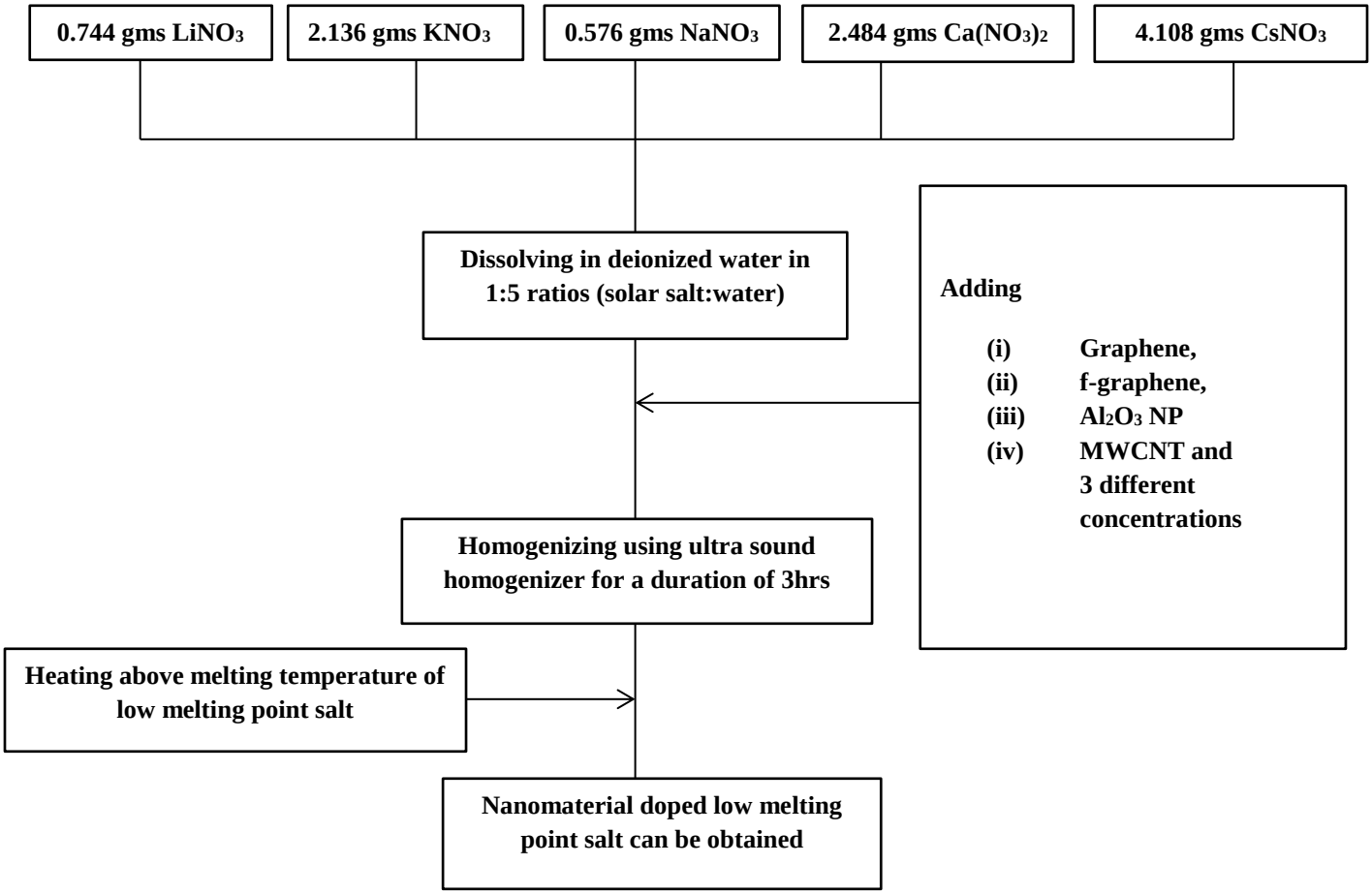

Figure 3-2: Flow chart for synthesis of low melting point salt doped GE, f-GE, SWCNT, Al_2O_3 NP, Cu NP, MWCNT and fullerene.

Afterwards, the nanosuspension was heated on a hotplate at constant temperature of 200 ^oC to vaporize the deionized water. It is important to note that if the nanosuspension is heated for more than 200 ^oC, then nanosuspension will spill out along with water bubbles. After heating for overnight period, the resultant nanosuspension obtained as GE dispersed molten salt as shown in Figure 3-3.

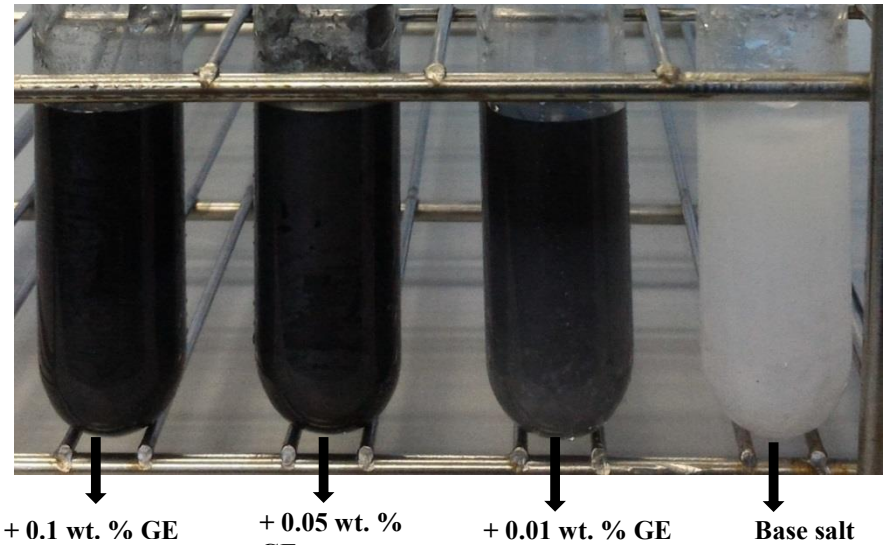

Figure 3-3: photograph of synthesized base salt along with dispersion of GE concentrations

GE dispersed molten salt were collected for thermal properties, rheological, corrosion, x-ray diffraction and Fourier transfer infrared measurements.

CHAPTER – 4

CHARACTERIZATION TECHNIQUES

4.1 Introduction

This chapter gives details of different types of characterization techniques were used for analyzing thermal properties, rheological and corrosion properties of the synthesized eutectic salts and nanosuspension. Characterizations of each sample were done 3 times, so that results should be repeatable. Characterization techniques used here are briefly described below.

4.2 Differential Scanning Calorimeter (DSC)

Heat Capacity (HC) was measured using differential scanning calorimetry (DSC) (TA instrument, Q2000 model) under N_2 atmosphere with flow rate of 20 ml/min as shown in Figure 4-1. Tzero aluminum pans and lids were used for DSC measurement. All pans are hermetically sealed and on the top of lid very small hole was punctured to remove moisture at high temperature. Approximately 25 mg of each sample mass was used for each run. As the molten salt absorbs moisture, samples were heated from room temperature to 180 ^{o}C and then held for 5 mins to remove moisture. Then sample temperature was reduced at a rate of 10 ^{o}C/min to bring down to room temperature. Again, temperature was raised at 10 ^{o}C/min, to 350 ^{o}C to obtain HC values of the sample.

Figure 4-1: DSC of TA instrument

4.3 Differential Thermogravimetric Analysis (DTGA)

Thermal properties were measured by subjecting heat to the sample. Thus, weight loss or gain of the sample with respect to temperature were measured by using thermo-gravimetry analysis (TGA) instrument. Thermal properties of molten salt dispersed with various concentrations of GE were measured using TGA (Mettler Toledo, STARe model) as shown in Figure 4-2. Aluminum pans and lids were used for thermal analysis. Approximately 15 mg of each sample taken in aluminum pan, aluminum pan was hermetically sealed with the lid. STARe software was used to program TGA instrument. All molten salts were heated from room temperature to 500 ^{o}C with a ramp rate of 10 ^{o}C/min. N_2 atmosphere was maintained at 20 ml/min. However, due to the limitation of using aluminum pans up to 500 ^{o}C, analysis was stopped at this temperature.

Figure 4-2: Photograph of DTGA of Mettler Toledo

4.4 Field Emission Scanning Electron Microscope (FESEM)

In general HC is mainly related to uniform dispersion of nanomaterials in the samples. FESEM has been used for high magnification images of base and GE dispersed molten salts. FESEM images were taken using FEI instrument (quanta 400F model). Energy dispersive X-ray (EDX) spectrometry was used for elemental composition of the samples using Oxford instruments (INCA 400 with X-max detector) as shown in Figure 4-3.

Figure 4-3: FESEM of FEI instrument

4.5 Thermal Conductivity

Thermal Conductivity (TC) was measured using KD2 pro thermal properties analyzer. Aluminum container having outer diameter of 3.7 cm and inner diameter of 2.9 cm was used. In order to maintain thermal stability, aluminum container was covered with sufficient cotton wool which in turn was wrapped with aluminum foil. Aluminum container was filled with silicon oil. Vial containing sample and TC probe was immersed in the silicon oil. This entire setup was kept on hot plate to maintain the desired temperature, as shown in Figure 4-4. KD2 pro device was programmed to get TC readings after every 15 minutes. For every particular temperature, three readings are collected and mean of these reading are noted.

Figure 4-4: Thermal conductivity setup

4.6 Hybrid Rheometer

Rheological properties were measured by using a discovery hybrid rheometer (TA instruments), as shown in Figure 4-5. Discovery hybrid rheometer has Peltier stage which operates within temperature range of -40 ^{o}C to 200 ^{o}C. There is a spindle at the center of Peltier stage for automatic detection of rheological properties. Schematic diagram of hybrid rheometer is shown in Figure 4-6. Synthesized molten salts were placed on Peltier stage. Then the sample is heated to desired temperature. Programming for rheology measurement was done through Trios v3.3.1.4364 software. After attaining desired temperature, soak time of 1 min was provided, so that stage and sample should have identical

temperature. Shear rate was varied from 0 to 1000 s^{-1}. All measurements were done by maintaining constant temperature. Rheological properties were investigated at four different temperatures of 70 ^{o}C, 80 ^{o}C, 90 ^{o}C and 200 ^{o}C. 70 ^{o}C and above temperature was chosen as the selected molten salt will be in liquid state.

Figure 4-5: Rheology measurements using discovery hybrid of TA instrument

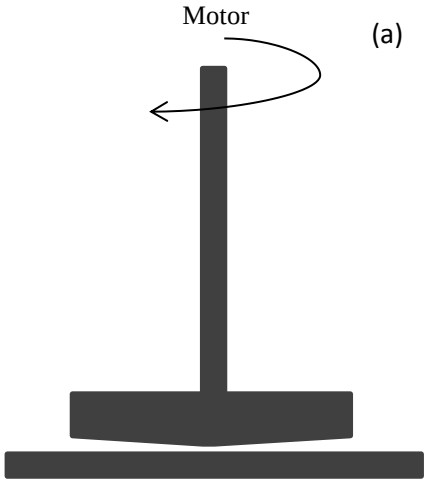

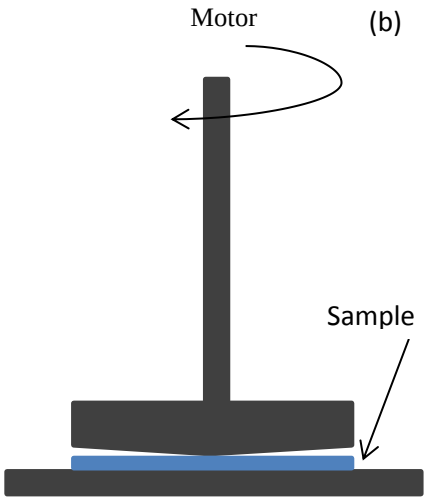

Figure 4-6: Schematic diagram of hybrid rheometer (a) without sample and (b) with sample.

4.7 Fourier Transform Infrared (FTIR)

Fourier transform infrared spectrometer measurements were carried out using spectrum 100 instrument of Perkin Elmer, as shown in Figure 4-7. Programming has been done through software spectrum 6.3.5. FTIR data has been collected within the frequency range of 4000-650 cm^{-1}. Samples were made by hard press to make in to disc type. KBr has not been used because molten salt can become in disc structure. However, KBr is transparent to infrared radiations. FTIR spectrometer is used to analyze degradation of samples, by verifying its respective peaks [209].

Figure 4-7: FTIR instrument of Perkin Elmer

4.8 X-ray Diffraction (XRD)

X-ray Diffraction (XRD) characterization was performed by BRUKER aXS-D8 advance X-ray diffractometer with Cu Kα, having wavelength=1.5405 Å and X-ray radiation in the 2theta angle ranging from 10^{o} to 100^{o}.

Figure 4-8: X-ray Diffractometer of Bruker

4.9 Corrosion test

ASTM D 130 is the standard method to test corrosiveness of copper [210]. Copper and SS304 strips are made in 30 mm X 10 mm as mentioned in ASTM standards. All strips were polished using silicon carbide paper. Strips were immersed in a veil containing molten salt, and then the veils were heated and tested. All samples were heated at 100 ± 5 ^{o}C for 24 hrs. Then strips were removed and cleaned. Color change of copper strips was compared with ASTM copper strip corrosion standard [210].

CHAPTER – 5

RESULT AND DISCUSSION

5.1 Introduction

This chapter gives detailed analysis of synthesised eutectic salt and nanosuspension. HC, TC, thermal properties, rheological properties, corrosion properties, predicting of HC, TC and viscosity has been discussed in this chapter. Outcome of the characterization studies have provided the strong basis for furthermore analysis of nanosuspension in solar thermal collector.

5.2 Graphene

Figure 5-1 (a), (b) and (c) shows SEM images of multilayered graphene 60 nm. It was found that graphene as two dimensional multilayered sheets. At atomic level graphene has honeycomb lattice structure with sp^2 hybridization. Figure 5-2 shows XRD graph of graphene 60 nm multilayered sheets. It was observed that graphene peak at 26.69 degrees.

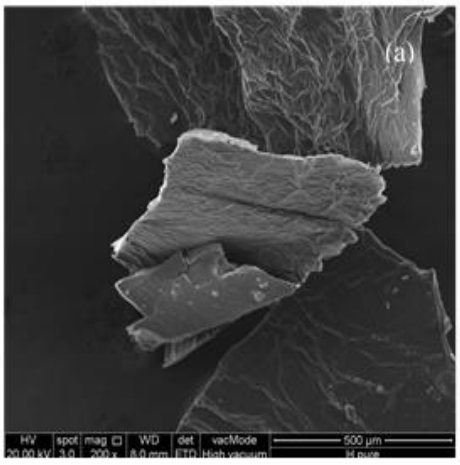

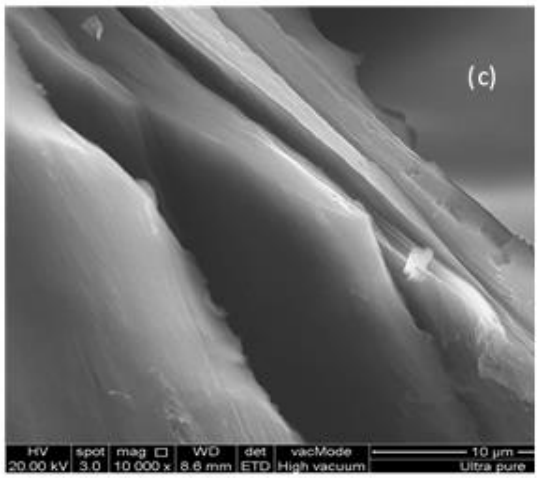

Figure 5-1: (a), (b) and (c): SEM image of multilayered graphene 60nm sheets

X-ray diffraction peak matches with ICSD (inorganic crystal structure database) pattern number 98-005-2916.

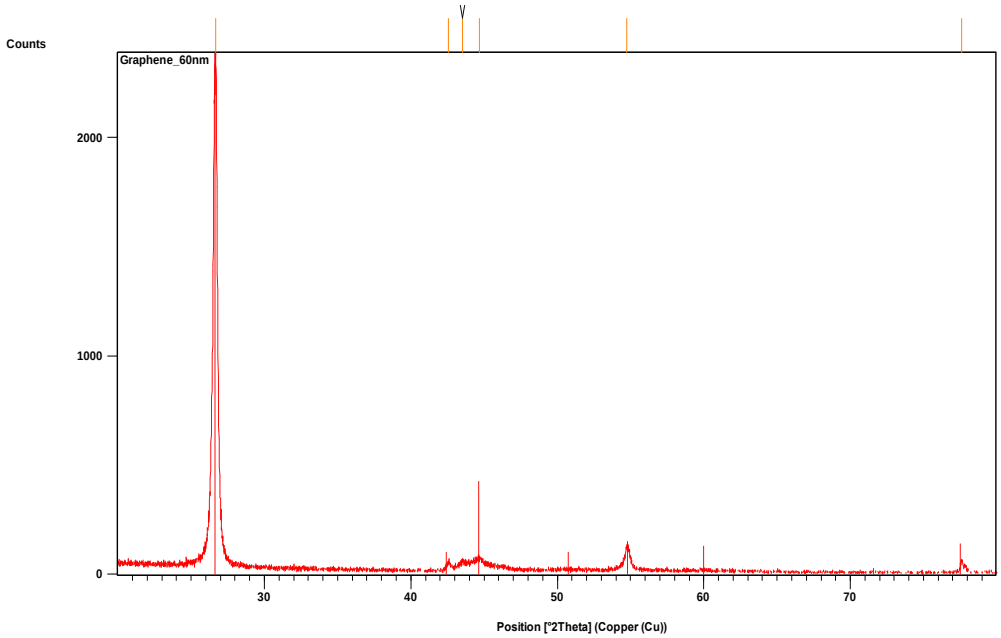

Figure 5-2: XRD graph of graphene 60nm sheet.

5.3 Differential Scanning Calorimetery

Figure 5-3 shows effect of GE concentration on HC of base molten salts. It was observed that HC is constantly enhanced with increasing concentration of GE. The average enhancement in HC varies from 5-13%, with respect to GE concentration. HC obtained for various samples are tabulated in Table 5-1 as shown below. From Table 5-1, it is clear that HC is a linear function of GE concentration. Enhanced HC of nanosuspensions may be due to following reasons. They are (i) reduced inter-crystal spacing due to presence of GE and (ii) a new mechanism of semi-solid behavior is expected to appear at the interaction between GE and molten salt. This semi-solid behavior possesses high thermal properties than liquid [183].

Table 5-1: Enhanced HC values with various concentrations of GE in base molten salts

Salt with various concentration of GE	Lowest HC	Highest HC value	Average HC	Enhanced HC
base salt	1.19 at 25 ^{o}C	1.38 at 185 °C	1.26	-
0.01 wt. %	1.25 at 25 ^{o}C	1.45 at 190 °C	1.34	5.065%
0.05 wt. %	1.28 at 25 ^{o}C	1.48 at 193 °C	1.39	7.525%
0.1 wt. %	1.36 at 25 ^{o}C	1.56 at 191 °C	1.46	13.169%

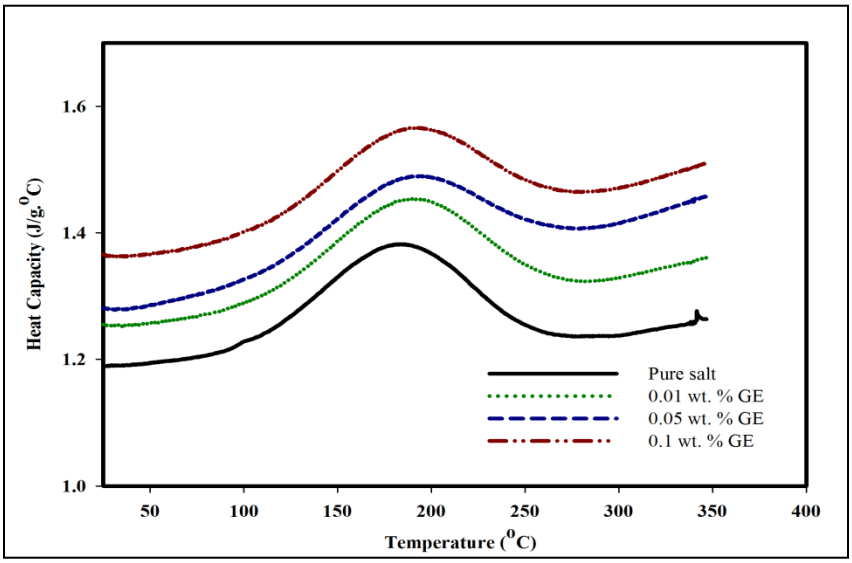

Figure 5-3: HC of base salt and mixed with different concentrations of GE

5.3.1 Dispersion of different concentration of GE in molten salt

As it was observed that enhancement in HC with doping of GE in molten salt. We tried to analysis enhancement in HC with increasing wt. % of GE. So, we tried to analyze for 1 wt. %, 3 wt. % and 5 wt. % of GE in pure salt. Synthesis process remains the same as shown in Figure 5-4. Just we increased doping wt. % of GE. For every 10gm of molten salt, we doped 0.1 gms, 0.3 gms and 0.5gms of GE for 1 wt. %, 3 wt. % and 5 wt. %, respectively. Figure 5-4 shows HC enhancement and detract with different wt. % of GE. 1 wt. % of GE shows an enhancement of HC by 14.550%. But, 1 wt. % of GE will not be economical. However, for 3 wt. % and 5 wt. % of GE, there is detract in HC enhancement, this might be due to coagulating of GE at one point [211].

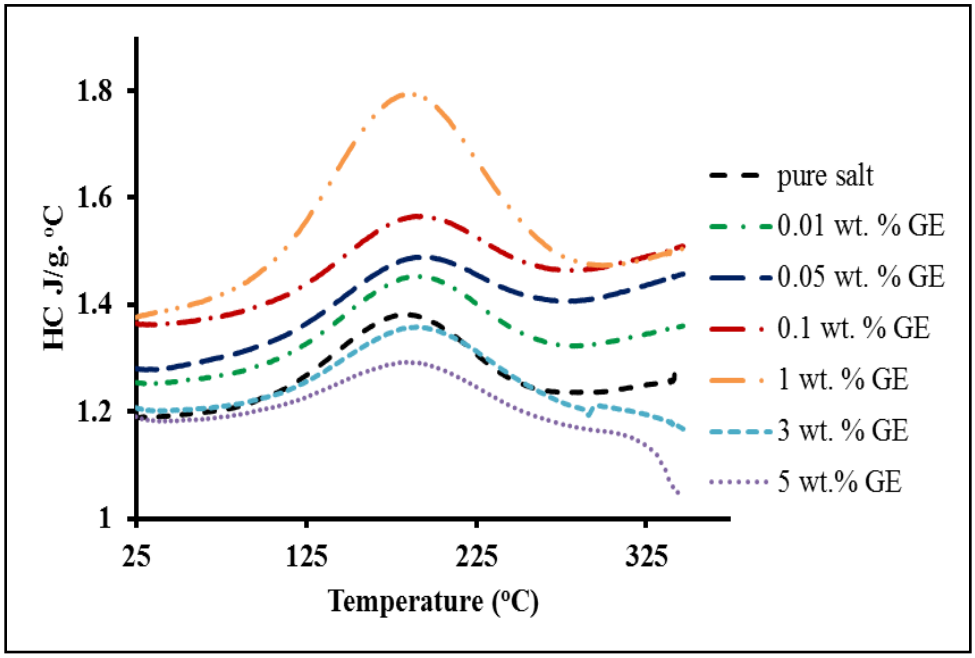

Figure 5-4: DSC characterization of pure salt and doped with different concentration of GE.

5.3.2 Dispersion of GE oxide in selected molten salt

Figure 5-5 graph shows DSC characterization of pure salt and with dispersion of GO. In this experiment also, we have selected three different wt. % of GO (i.e, 0.01, 0.05 and 0.1 wt. %). Figure 5-5 shows uneven enhancement and detraction of HC. The possible reason for this is there is no successful convective heat transfer from molten salt to GO and vice versa. Another possible reason for decrease in HC of nanosuspension was that GE oxide particles are constrained at the interface of solid-liquid layer. This makes alteration in Gibbs free energy, thus making decline in HC of nanosuspension [212].

5.3.3 Dispersion of Aluminum oxide NP in molten salt

Figure 5-6 shows DSC graph of pure salt along with doping of Al_2O_3 NP with six different concentrations. Six different concentration are 0.05, 0.1, 1, 3 and 5 wt. %. From Figure 5-6, it was observed that by doping Al_2O_3 NP, HC is lower than pure salt. However, by increasing Al_2O_3 NP concentration, there is uneven enhancement and detraction in HC. This behavior of uneven enhancement of HC was due agglomeration of Al_2O_3 NP at one point. Agglomeration of Al_2O_3 NP in molten salt leads to alteration in convective heat transfer in nanosuspension. In addition to alteration in Gibbs free energy, changes in phonon vibration at the solid-liquid interface, also plays a prominent role in alternation of HC. Variation in phonon vibration and Gibb free energy results in decrease of HC [184].

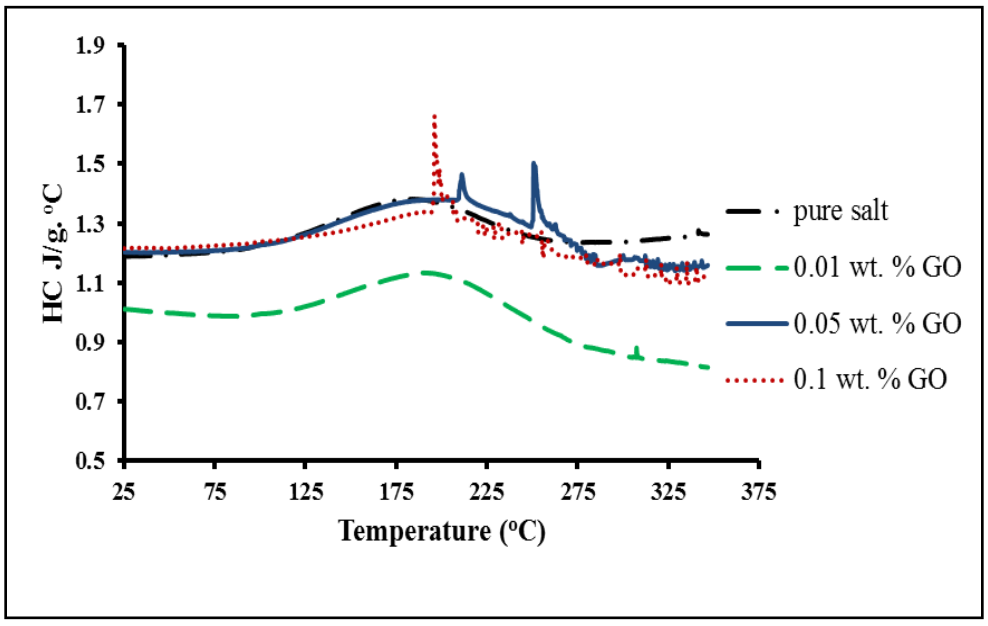

Figure 5-5: DSC characterization of pure salt and doped with different concentration of GE oxide.

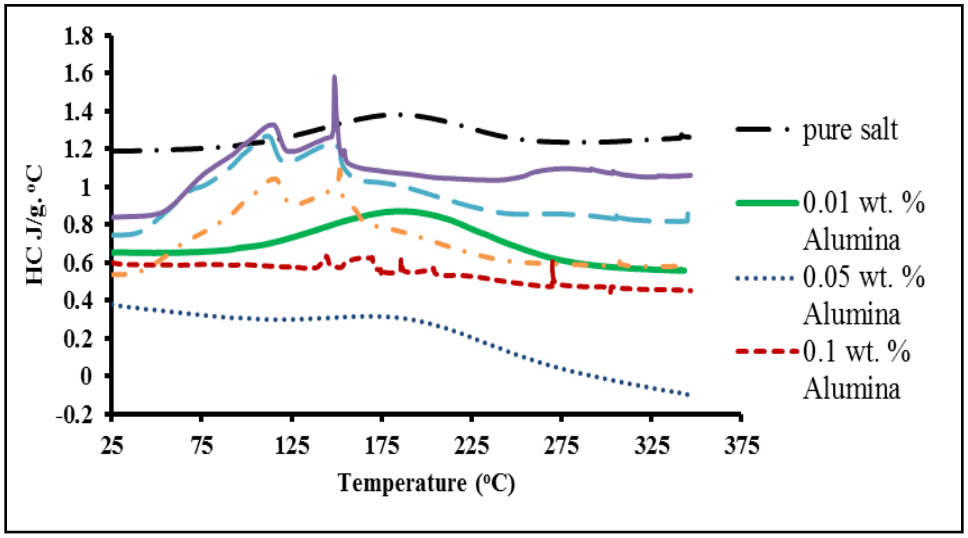

Figure 5-6: DSC characterization of pure salt and doped with various concentrations of Al_2O_3 NP.

5.3.4 Dispersion of multi-walled carbon nanotube in molten salt

Figure 5-7 shows DSC graph of multi-walled carbon nanotube in molten salt with three different concentrations. Three different concentrations are 0.01 0.05 and 0.1 wt. %. From Figure 5-7, it was concluded that by doping multi-walled carbon nanotube in molten salt results in lower HC than base salt. This behavior of declined HC for increasing concentration of multi-walled carbon nanotube may be due to coagulation of multi-walled carbon nanotube at one point.

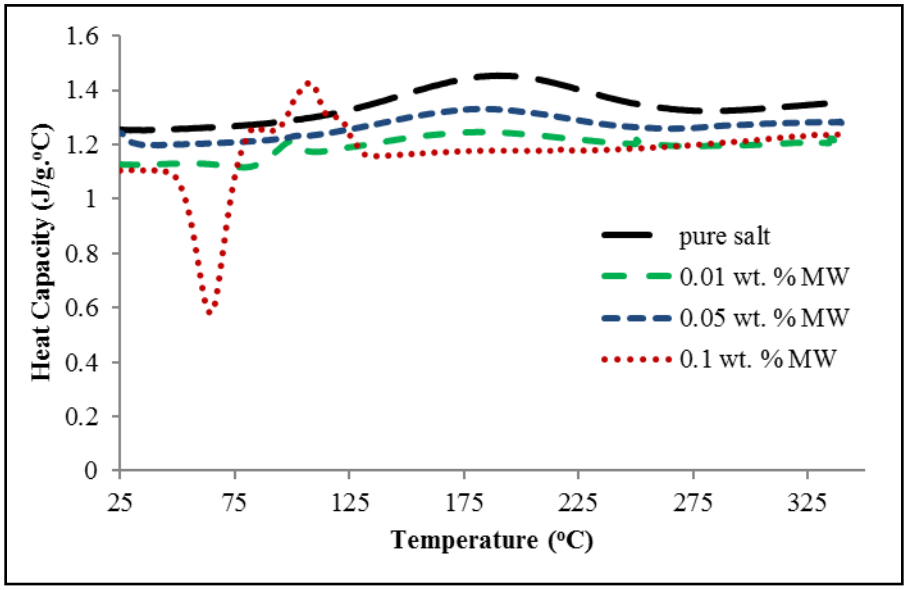

Figure 5-7: DSC characterization of base salt and doped with various concentrations of MWCNT.

5.3.5 Theoretical Analysis of HC

Figure 5-8 gives comparison of theoretical and experimental analysis of HC. Density and HC of molten salt were measured as 2.708 g/cm^3 and 1.19 J/g. ^{o}C. Density and HC of GE were used are 2 g/cm^3 and 0.71 J/g. ^{o}C. Density of molten salt was measured using conventional (mass/volume) method. Predicting of HC of nanosuspension has been done using thermal equilibrium equation. This study has been done only to compare experimental results with general equation results.

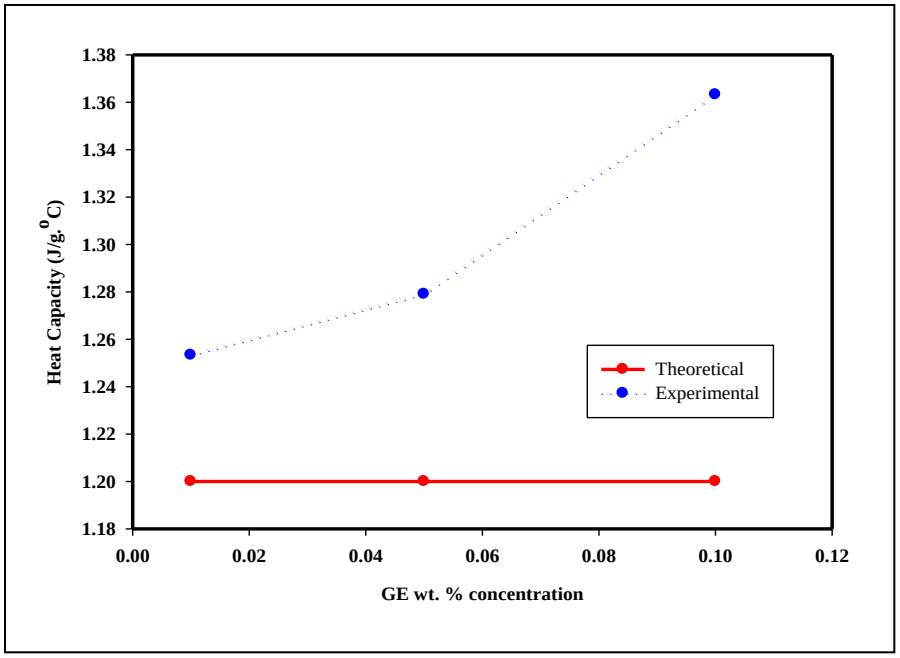

Figure 5-8: Comparison of theoretical and experimental HC with three concentrations of GE (0.01, 0.05 and 0.1 wt. %)

The experimental values are in good agreement with theoretical values having deviation of 4.44%, 6.58% and 13.60% for 0.01, 0.05 and 0.1 wt. % GE, respectively. This deviation was because the above model does not take consideration of temperature and thickness or size of GE. However, authors suggest that improvement in the Eq. 2-6 can be done by superposition of individual HC of base fluids and nanomaterial. Large deviation in experimental result compared to theoretical prediction of HC was due to constrained layering at solid-liquid interface. This constrain makes alteration in Gibbs free energy, thus causing change in HC.

5.4 Field Emission Scanning Electron Microscope (FESEM)

Figure 5-9 shows scanning electron microscope (SEM) and back scattered electron (BSE) images of base salt and GE doped molten salts. Generally, BSE is used for knowing of various elements in the samples through contrast difference. From Figure 5-9, it can be observed that all samples absorbed moisture while placing in FESEM chamber. As all nitrate salts are hygroscopic in nature and eutectic mixture of nitrate salts makes hygroscopic nature more drastic. Hence, it was difficult to obtain clear SEM and BSE images of the samples.

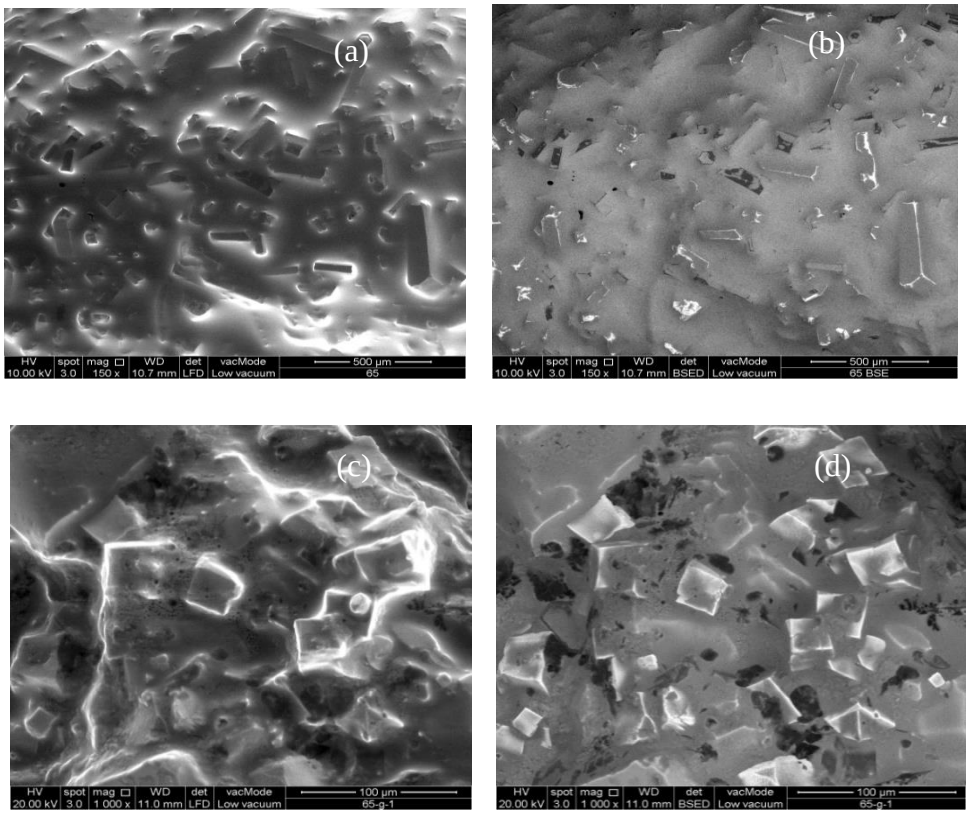

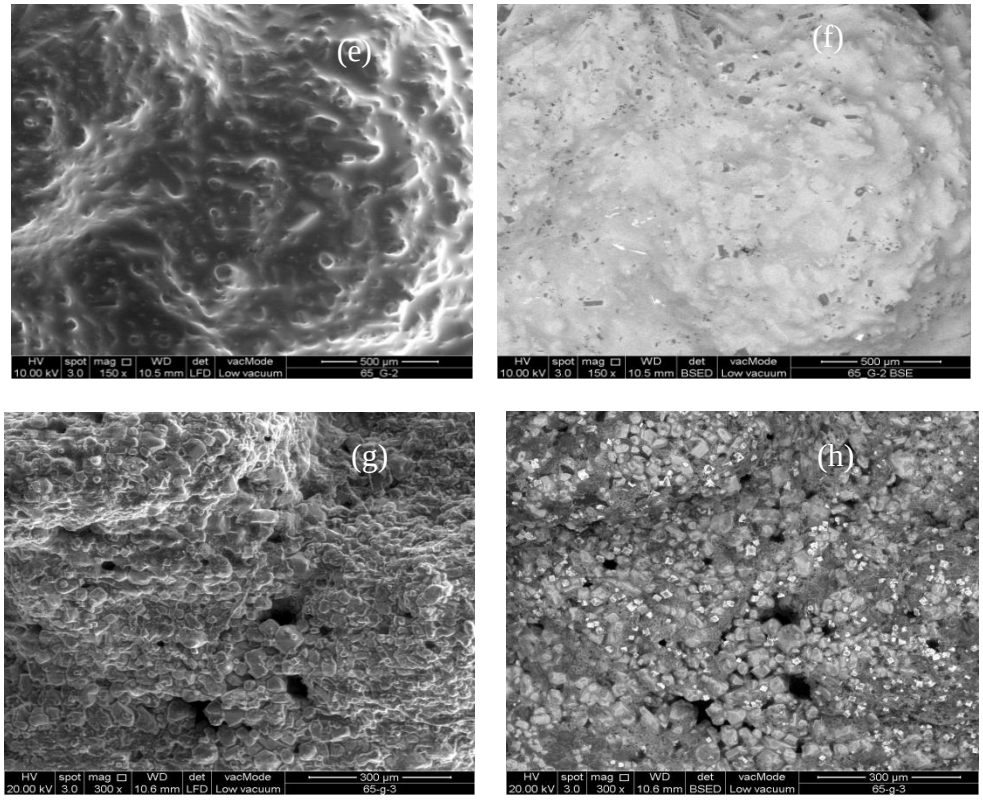

Figure 5-9: (a), (c), (e), (g) are SEM and (b), (d), (f) and (h) are BSE images of base salt, 0.01 wt. %, 0.05 wt. % and 0.1 wt. % doped, GE respectively.

5.4.1 Energy Dispersive X-ray (*EDX*) Analysis

From BSE characterizations, contrast difference of various elements cannot be clearly seen due to hygroscopic nature of molten salts. Other option for is go to for EDX analysis. Basically, EDX is used for knowing elemental composition in the sample. The purple line in the Figure 5-10 is the scanned area for EDX analysis. From the peaks, it can be deduced that all elements of molten salt are available, except Li. As EDX detect elements heavier than Be. It can also be observed through weigh composition that carbon (C) quantity was very low for base salt.

Gradually, amount of carbon is increasing with respect to GE concentration.

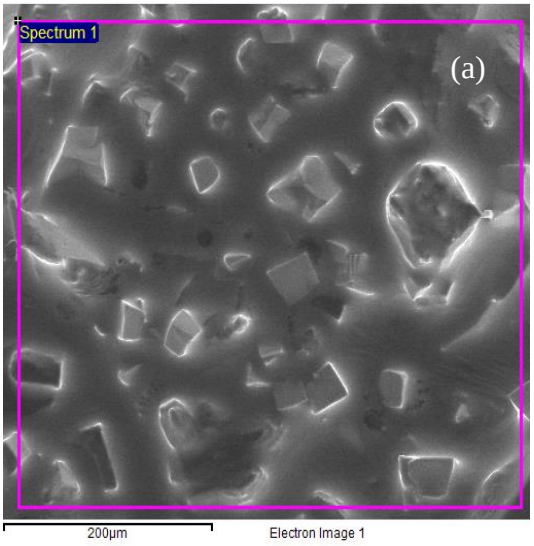

(b)

Spectrum 1

Element	Weight%	Atomic%
C K	3.16	5.62
N K	13.94	21.27
O K	46.69	62.38
Na K	0.83	0.77
K K	8.68	4.74
Ca K	2.47	1.32
Cs L	24.23	3.90

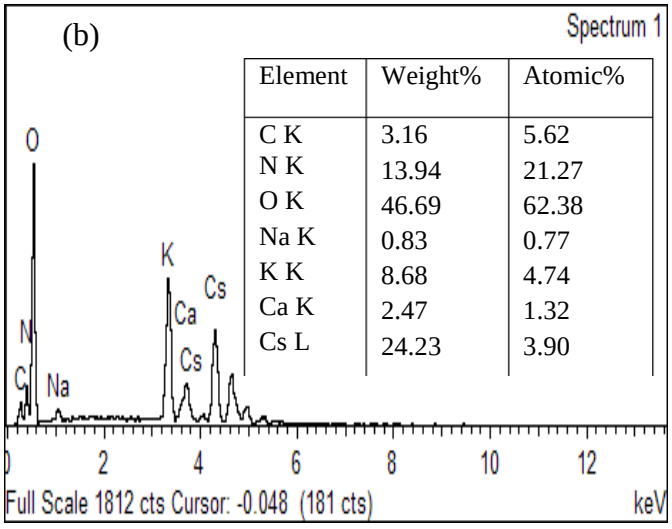

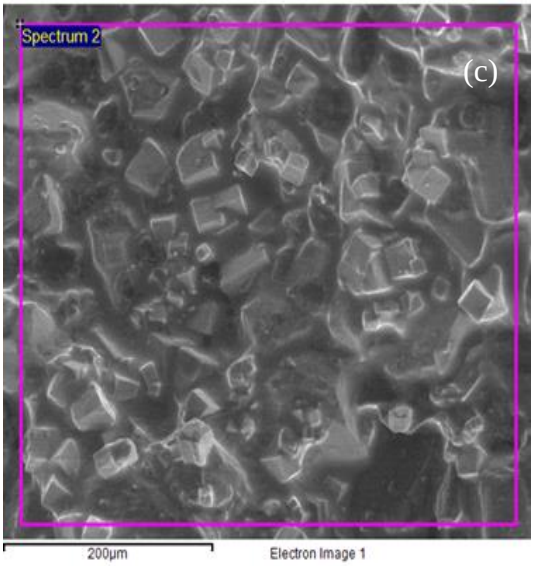

(d)

Spectrum 2

Element	Weight%	Atomic%
C K	5.37	9.44
N K	13.11	19.74
O K	45.97	60.61
Na K	1.09	1.00
K K	7.51	4.05
Ca K	1.78	0.94
Cs L	24.77	3.93

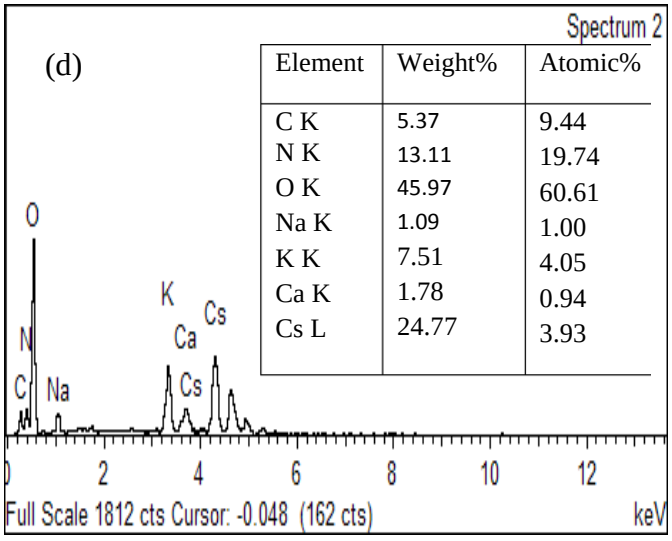

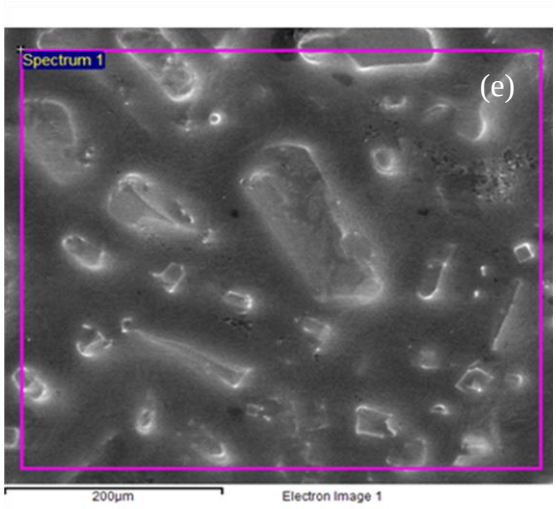

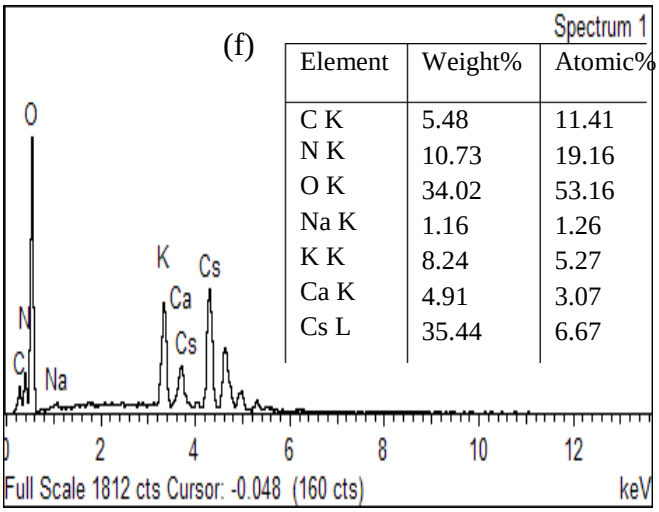

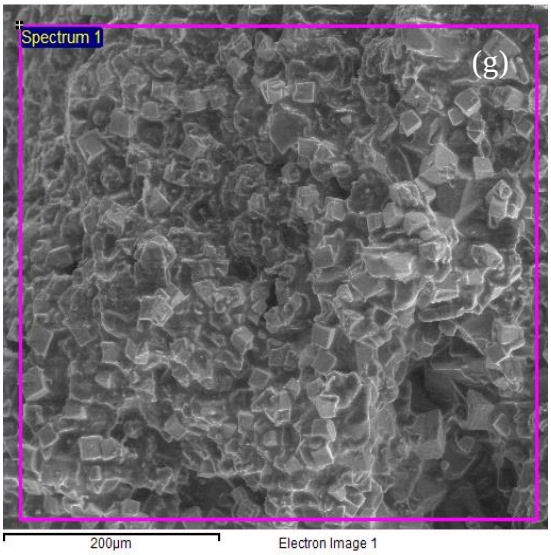

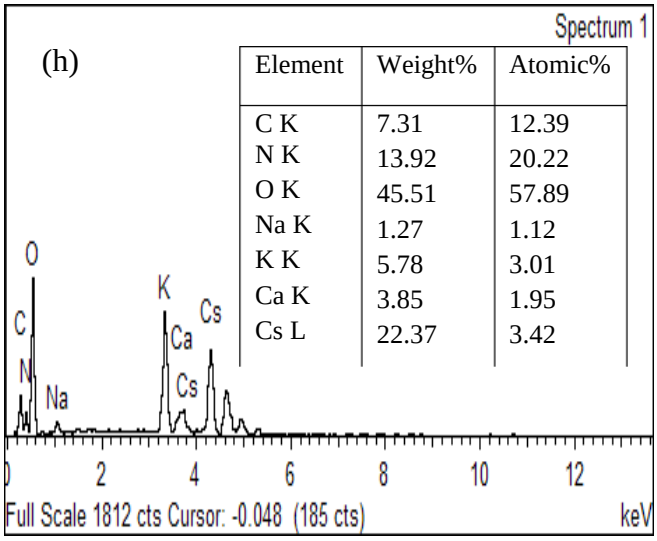

Figure 5-10: (a), (c), (e) and (g) are SEM images, where EDX pattern had scanned. (b), (d), (f) and (h) are EDX pattern of base salt and with different concentrations of GE.

5.5 Thermogravimetric Analysis (TGA)

TGA graph of pure molten salt mixed with different concentration of GE is shown in Figure 5-11. In graph, there is a small jump at starting point of curve. This is because of hygroscopic nature of nitrates and mixture of nitrates makes overall composition more hygroscopic. While weighing of samples, molten salt absorbs moisture. This moisture will get remove, while the sample gets heated above its room temperature. It can be observe that there was a huge weight loss for all samples below 200 ^{o}C. As the characterization was done under N_2 atmosphere, evaporation of water molecules takes just below 200 ^{o}C. After evaporation of water molecules, it was observed that all samples are thermally stable up to 500 ^{o}C. TGA characterization was repeated with same samples and also it was observed approximately same TGA curve for all repeated samples.

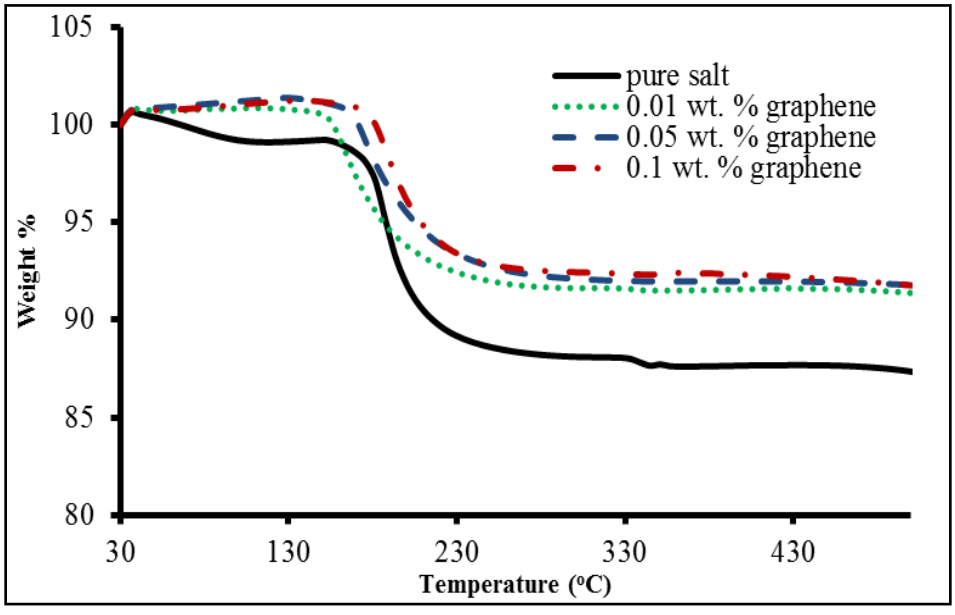

Figure 5-11: Normalized TGA curve of pure salt with different concentrations of GE.

5.6 Differential Thermogravimetric Analysis (DTGA)

Differential Thermogravimetric Analysis (DTGA) graph of base molten salt mixed with different concentrations (0.01, 0.05 and 0.1 wt. %) of GE is shown in Figure 5-12. A small jump is noticed at the start of the curve. This is because of hygroscopic nature of nitrate salts. While weighing of samples, molten salt absorbs moisture, which was removed when the sample gets heated above room temperature. Melting point of base salt was observed around 72 ^{o}C, instead of 65 ^{o}C [171]. It was because of N_2 gas atmosphere. A huge weight loss for all samples was observed below 200 ^{o}C. As the characterization was done under N_2 gas atmosphere, evaporation of water molecules takes place below 200 ^{o}C. By analyzing Figure 5-12, it is evident that all the synthesized molten salts are thermally stable up to 500 ^{o}C.

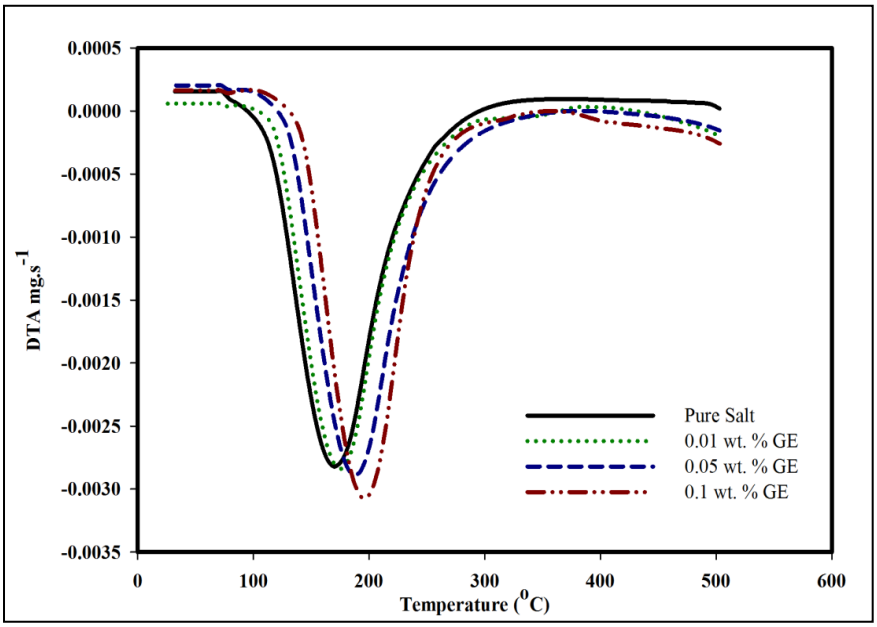

Figure 5-12: DTA curve of base salt with different concentrations of GE.

5.7 Thermal Conductivity

Effect of GE addition on TC is depicted in Figure 5-13. The TC of base salt decreased with increasing temperature. With the addition of 0.01 wt. % GE in molten salt, initially the TC decreased until 50 °C and remained almost constant up to 70 °C and starts to increase from 70 °C. However, enhanced TC for 0.05 and 0.1 wt. % GE compared to base salt which depicted the similar trend of initial decrease in TC with temperature until 70 ^{o}C and starts to increase after 70 ^{o}C. There was an increase in TC enhancement by 1.32 and 2.31% by doping GE of 0.05 and 0.1 wt. %, respectively. Enhanced TC may be due to high TC and Brownian motion of GE [213]. Another reason for enhanced TC may be due to percolation network of GE at higher concentration [214].

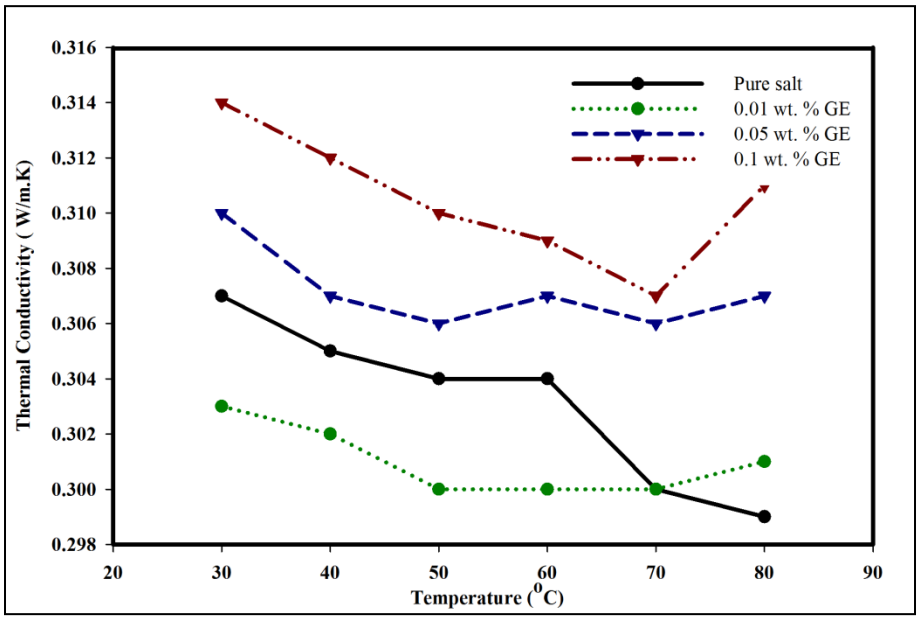

Figure 5-13: TC of base molten salt with different concentration of GE (0.01, 0.05 and 0.1 wt. %).

Few TC models like Maxwell, Hamilton-Crosser and Nan's models are also discussed in later sections.

5.7.1 Maxwell and Hamilton-Crosser models

Predicting TC values of molten salt doped with GE are studied here using Maxwell and Hamilton-Crosser models. Figure 5-14 shows the comparison between effective TC of Maxwell, Hamilton-Crosser models and experimental results at room temperature. Table 5-2 shows list of variables and its values used in theoretical models. It was observed that both Maxwell and Hamilton-Crosser models are very close to experimental results. Deviation of error for both Maxwell and Hamilton-Crosser models is in between ±3%. These two models take into consideration of individual TC and volume fraction values. Khanafer and Vafai [215] observed that Hamilton-Crosser model gives good prediction of TC with volume fraction of nanomaterials ≤ 4%. Hence predicting TC values of molten salt doped with GE is in good agreement with experimental results.

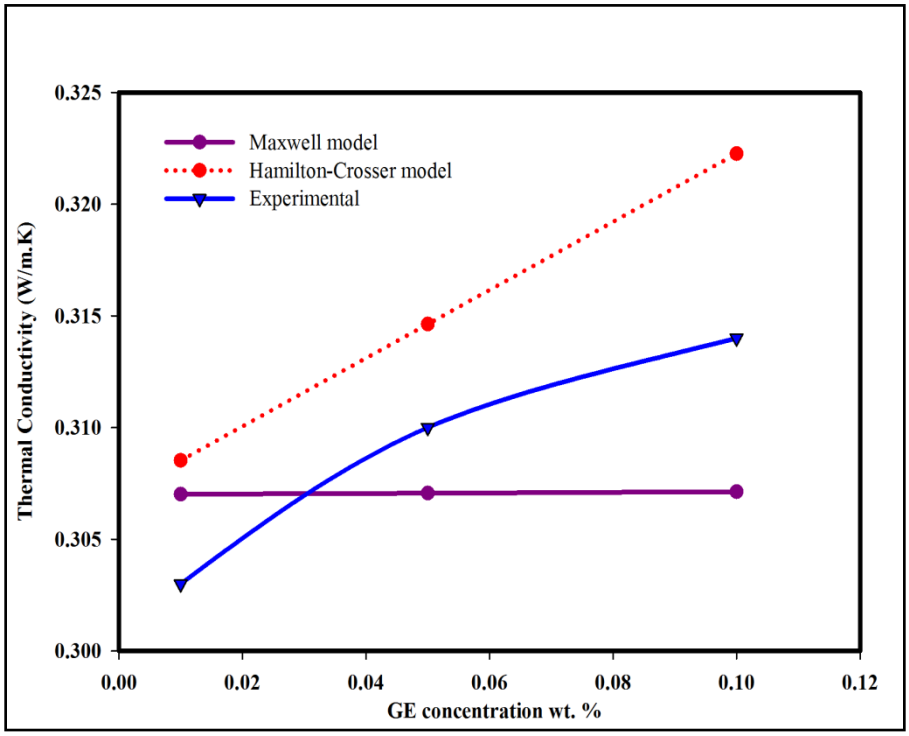

Figure 5-14: Comparison of experimental TC results with Maxwell and Hamilton-Crosser model with respect to GE concentration at room temperature.

Table 5-2: List of variables used in Maxwell and Hamilton-Crosser model

Variable	**Value**
Kp	5200 W/m.K
Kf	0.307 W/m.K
ϕ (10^{-5})	1.34751, 6.73721 and 13.4735
n_s	375

5.7.2 Nan Model of TC

Nan et al. [133] has developed a TC model for CNT based fluids as presented in equation (4) and (5). In Nan's model, aspect ratio of GE was used. Figure 5-15 shows comparison of Nan's model with measured

experimental results at room temperature. It was observed that Nan's model significantly over predicted the experimental data. The error of deviation was exponentially increasing with respect to addition of GE concentration. This discrepancy may be due to the effect of GE sheet thickness, as Nan's model does not take GE thickness into the consideration. Another reason for enhanced TC of Nan's model was due equation (4) is largely dependent on change in volume fraction [216].

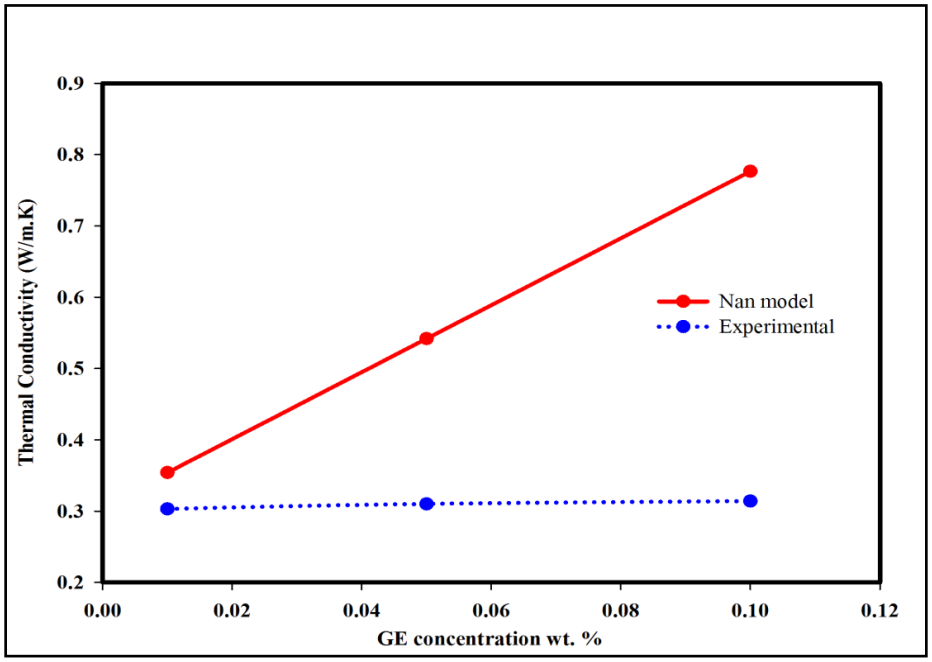

Figure 5-15: Comparison of experimental results with Nan's model prediction for 0.01, 0.05 and 0.1 wt. % of GE concentrations at room temperature.

5.8 Viscosity

Viscosity is defined as the retardation force made by the fluid to flow. Viscosity of molten salt mixtures at 70 ^{o}C along with three different concentrations of GE is shown in Figure 5-16 (a). It is well known that all nitrates are Newtonian fluids [217]. An average viscosity of base salt was measured as 2.6800 Pa.s. After addition of 0.01, 0.05 and 0.1 wt. % GE in base salt, average viscosity got increased by ~124%, ~208% and ~547%, respectively. Enhancement in viscosity is due to agglomeration of GE in molten salt [205]. Viscosity and dipole moment of base salt are important parameters that influence agglomeration of GE [218]. It is evident that the particle size and particle size distribution plays a significant role in viscosity enhancement. Due to agglomeration, the average cluster size increases and losses the uniform boundary layer near the wall hence increases the flow resistance.

From Figure 5-16 (a), it can also be observed that for each curve viscosity decreased marginally, with increase in shear rate. As the spindle starts to rotate, molten salt molecules try to align themselves in the direction of spindle rotation. This transition provides more friction to the spindle rotation. Once the molten salt molecules get aligned to spindle rotation, then it provides less friction to the spindle rotation than the former state. This makes former viscosity higher than later viscosity [216].

Effect of shear stress and shear strain is shown in Figure 5-16 (b), (d), (f) which demonstrates the non-Newtonian behavior of base salt and all nanosuspension at 70, 80 and 90 ^{o}C, respectively. Base salt and nanosuspension behavior is highly dependent on its kinematic history and duration of shear rate.

At 80 ^{o}C, the average value of viscosity of base salt is 0.7978 Pa.s, which is lower than viscosity at 70 ^{o}C. This is due to the fact that at higher temperature inter and intramolecular forces within the molten salt gets weaken. Similar trends were also observed at other higher temperatures up to 200 ^{o}C. By this, it can be concluded that molten salt viscosity is highly dependent on operating temperature. With addition of 0.01, 0.05 and 0.1 wt. % GE in base salt, there is an average enhancement of viscosity by ~62%, ~91% and ~424%, respectively. Table 5-3 gives an overview all results of viscosity.

Table 5-3: Enhanced viscosity values with various concentrations of GE in base molten salts

Temp\ sample name	base salt Viscosity (Pa.s)	base salt + 0.01 wt. % GE		base salt + 0.05 wt. % GE		base salt + 0.1 wt. % GE	
		Viscosity Pa.s	% enhancement	Viscosity Pa.s	% enhancement	Viscosity Pa.s	% enhancement
70 ^{o}C	2.6800	6.0287	124.95	8.2751	208.76	17.3659	547.96
80 ^{o}C	0.7978	1.2942	62.22	1.5268	91.38	4.1846	424.51
90 ^{o}C	0.3724	0.3382	-9.13	0.6493	74.35	1.7924	381.31
200 ^{o}C	0.0346	0.0352	1.49	0.0322	-6.89	0.0330	-4.66

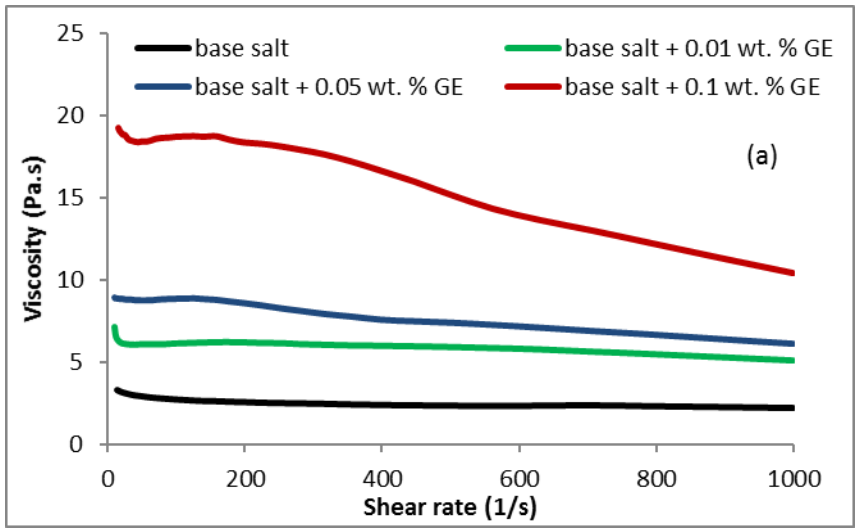
base salt
base salt + 0.01 wt. % GE
base salt + 0.05 wt. % GE
base salt + 0.1 wt. % GE
(a)
Viscosity (Pa.s)
Shear rate (1/s)
0
5
10
15
20
25
0
200
400
600
800
1000

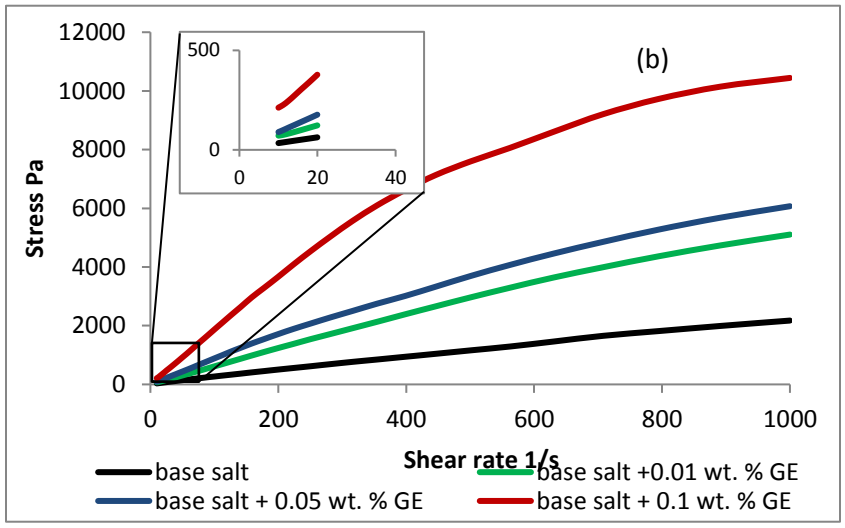
(b)
Stress Pa
Shear rate 1/s
0
2000
4000
6000
8000
10000
12000
0
200
400
600
800
1000
500
0
0
20
40
base salt
base salt +0.01 wt. % GE
base salt + 0.05 wt. % GE
base salt + 0.1 wt. % GE

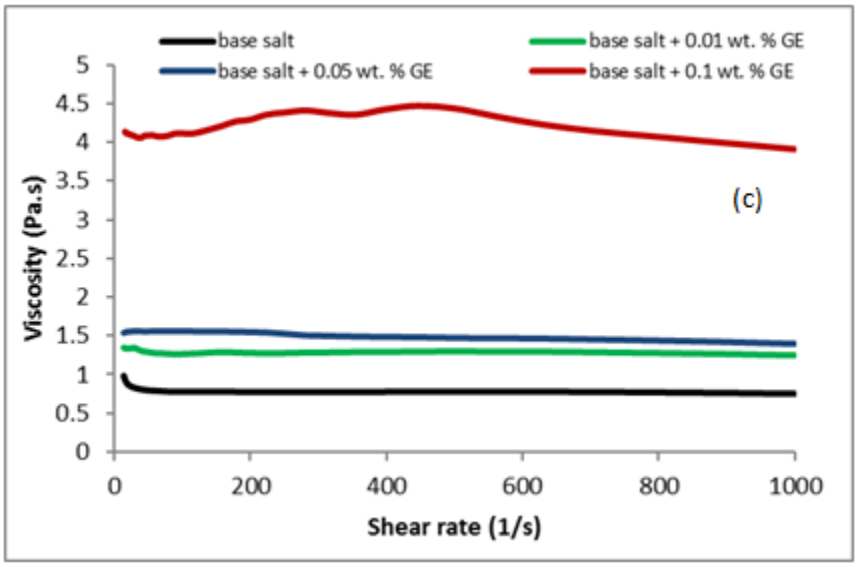
base salt
base salt + 0.01 wt. % GE
base salt + 0.05 wt. % GE
base salt + 0.1 wt. % GE
(c)
Viscosity (Pa.s)
Shear rate (1/s)
0
0.5
1
1.5
2
2.5
3
3.5
4
4.5
5
0
200
400
600
800
1000

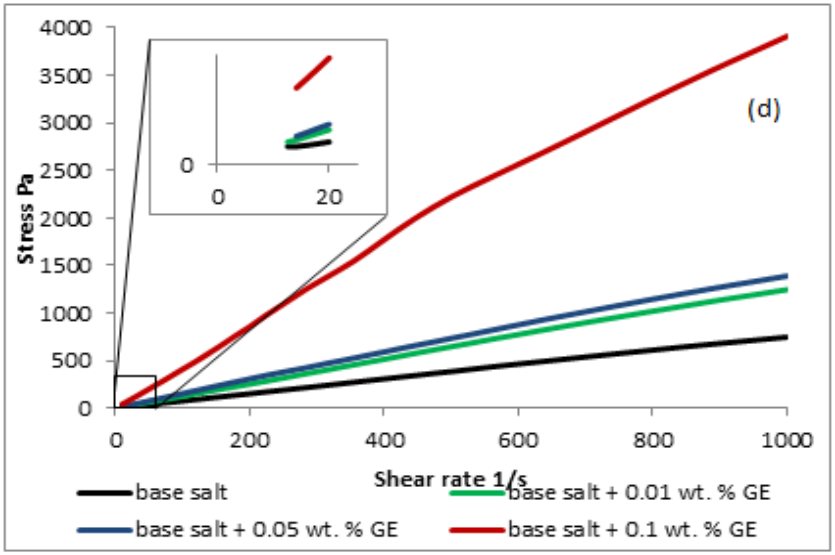
(d)
Stress Pa
Shear rate 1/s
0
500
1000
1500
2000
2500
3000
3500
4000
0
200
400
600
800
1000
0
0
20
base salt
base salt + 0.01 wt. % GE
base salt + 0.05 wt. % GE
base salt + 0.1 wt. % GE

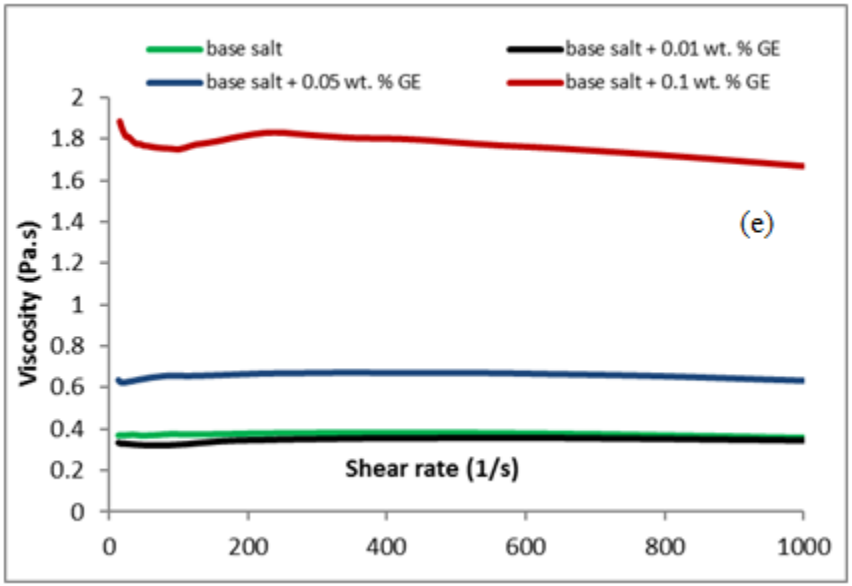
base salt
base salt + 0.01 wt. % GE
base salt + 0.05 wt. % GE
base salt + 0.1 wt. % GE
Viscosity (Pa.s)
Shear rate (1/s)
(e)
0
0.2
0.4
0.6
0.8
1
1.2
1.4
1.6
1.8
2
0
200
400
600
800
1000

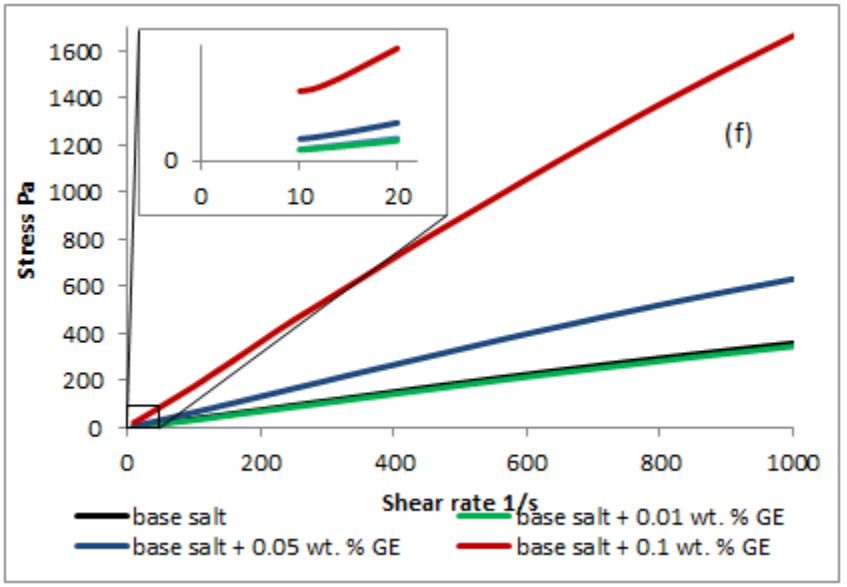
Stress Pa
Shear rate 1/s
(f)
0
200
400
600
800
1000
1200
1400
1600
0
10
20
base salt
base salt + 0.01 wt. % GE
base salt + 0.05 wt. % GE
base salt + 0.1 wt. % GE

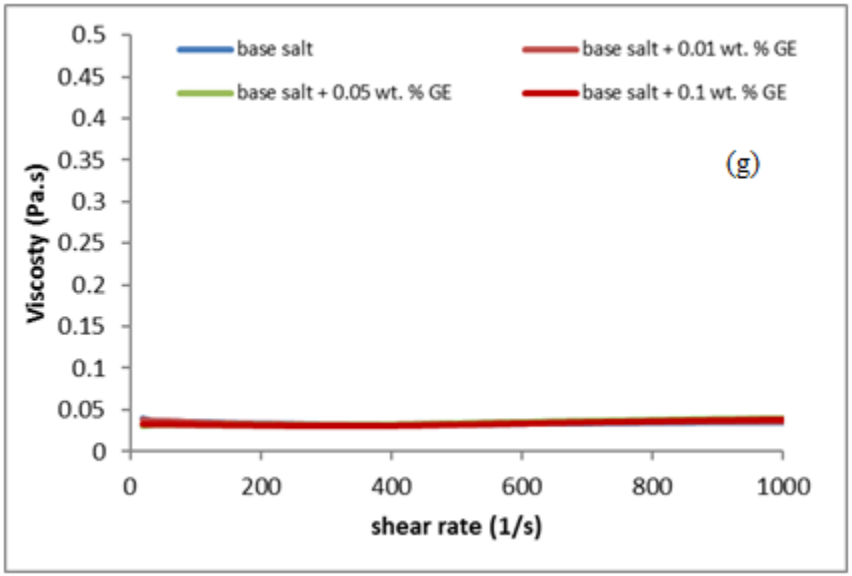
base salt
base salt + 0.01 wt. % GE
base salt + 0.05 wt. % GE
base salt + 0.1 wt. % GE
Viscosty (Pa.s)
shear rate (1/s)
(g)
0
0.05
0.1
0.15
0.2
0.25
0.3
0.35
0.4
0.45
0.5
0
200
400
600
800
1000

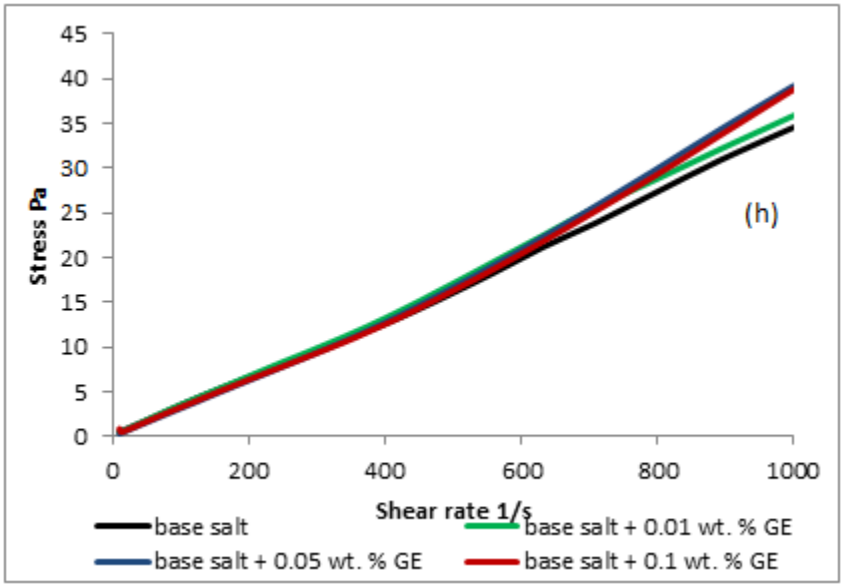
Stress Pa
Shear rate 1/s
(h)
0
5
10
15
20
25
30
35
40
45
0
200
400
600
800
1000
base salt
base salt + 0.01 wt. % GE
base salt + 0.05 wt. % GE
base salt + 0.1 wt. % GE

Figure 5-16: (a) Viscosity vs Shear rate and Stress vs Shear rate of base salt along with three different concentrations of GE at 70 ^{o}C, (c) & (d) Viscosity vs Shear rate and Stress vs Shear rate of base salt along with three different concentrations of GE at 80 ^{o}C, (e) & (f) Viscosity vs Shear rate and Stress vs Shear rate of base salt along with three different concentrations of GE at 90 ^{o}C and (g) & (h) Viscosity vs Shear rate and Stress vs Shear rate of base salt along with three different concentrations of GE at 200 ^{o}C.

5.8.1 Predicting of viscosity using Einstein model

Predicting viscosity values of molten salt dispersed graphene are studied here using Einstein model of viscosity. Figure 5-17 shows comparison between viscosities of Einstein model and experimental at various temperatures. Errors of deviation of Einstein's equation of viscosity are tabulated in Table 5-4. It was observed that Einstein's model is having large error of deviation at all temperatures except 200 ^{o}C. Large error of deviation is because of Einstein's model does not takes consideration of

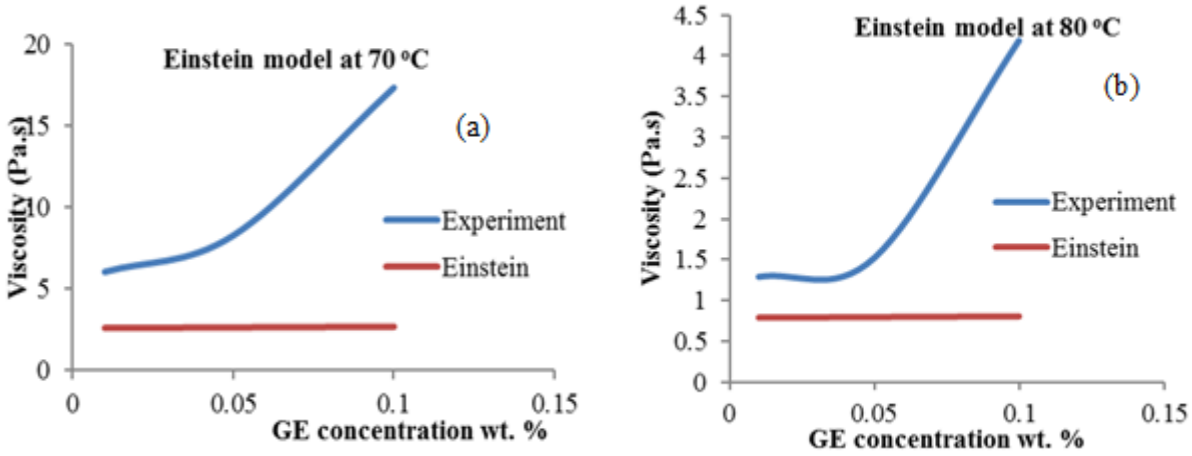

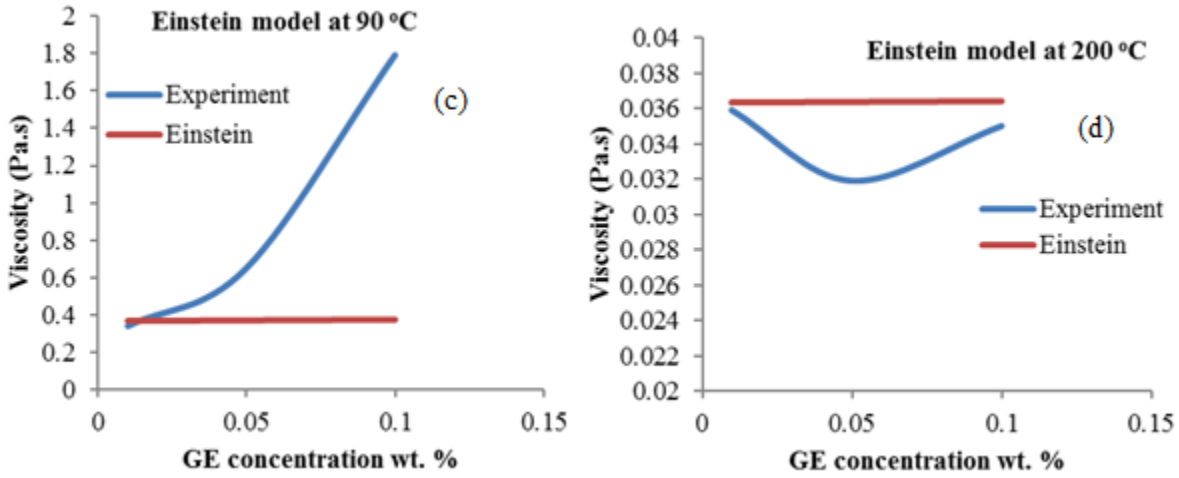

Figure 5-17: Comparison of experimental results at various temperatures with Einstein model. Comparison at (a) 70, (b) 80, (c) 90 and (d) 200 °C.

Table 5-4 Error deviation of Einstein's model of viscosity at various temperatures

Temperature (°C)	GE concentration wt. %	Theoretical Viscosity (Pa.s)	Experimental Viscosity (Pa.s)	% Error
70	0.01	2.6806	6.0287	~124
	0.05	2.6833	8.2751	~208
	0.1	2.6867	17.3659	~546
80	0.01	0.7978	1.2942	~62
	0.05	0.7987	1.5268	~91
	0.1	0.7997	4.1846	~423
90	0.01	0.3724	0.3382	~-9
	0.05	0.3728	0.6493	~74
	0.1	0.3733	1.7876	~379
200	0.01	0.0363	0.0359	~-1
	0.05	0.0363	0.0319	~-12
	0.1	0.0363	0.035	~-3

temperature and surface area of nanomaterial. With increase in temperature, error of deviation decreases. This is due to viscosity of molten salt reaching to its minimum value. Authors suggest developing a new formula for predicting of viscosity at various temperatures which

takes into consideration of (i) temperature, (ii) concentration of various fluids and nano particles (iii) size and shape of GE or nano particles and (iv) viscosity of base fluid.

5.9 Fourier Transform Infrared (FTIR)

Figure 5-18 shows FTIR spectrum of base salt and GE dispersed base salt. FTIR spectrums of all nitrate salts are present at band of 1340 cm^{-1} [219, 220]. The N-O is antisymmetric vibration band [221, 222]. Besides, it can be noticed that the angular deformation band of O-N-O at 840 cm^{-1} [223]. Base salt FTIR spectrum is also identical to FTIR spectrum of all GE dispersed base salt. Details of FTIR frequency and band assignment are given Table 5-5.

Table 5-5: FTIR frequency assignments

FTIR frequency (cm^{-1})	**Band Assignment**
3462	-OH
2849-2923	C-H stretching
2409	C-O stretching
1634	C=N stretching
1334	NO_3 stretching
1243-1040	$-COO^-$ vibrations
825-850	O-N-O group bending
760	$-COO^-$ In plane bending

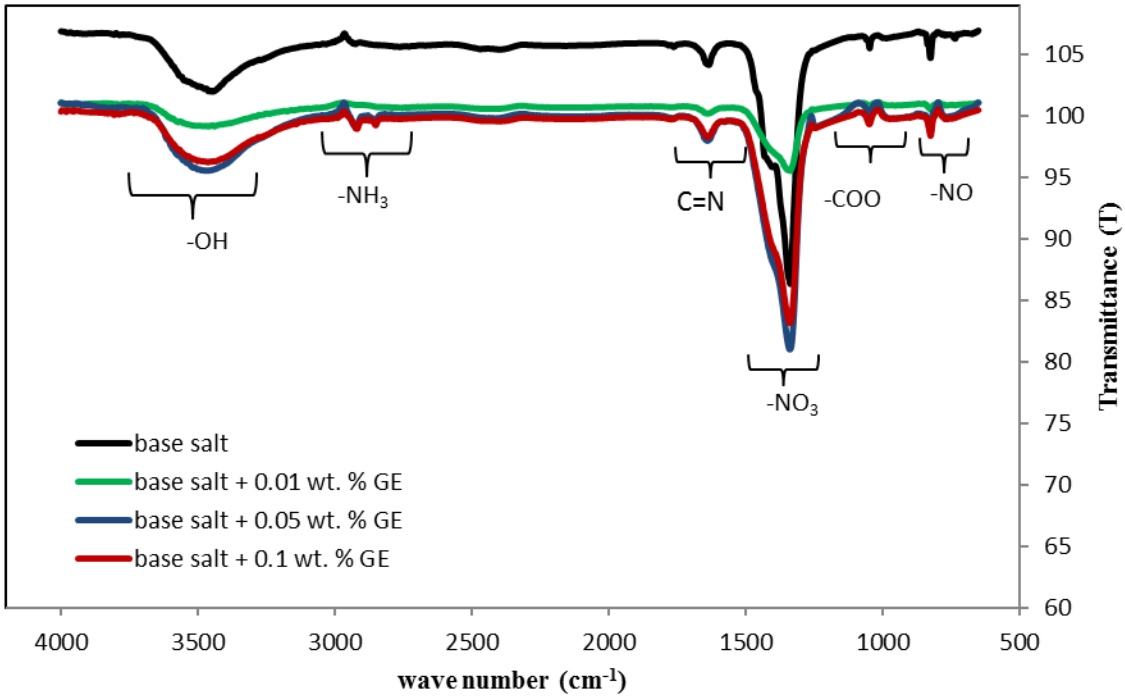

Figure 5-18: FTIR spectrum of base salt and GE dispersed base salt.

5.10 X-Ray Diffraction (XRD)

X-Ray Diffraction (XRD) spectra of base salt and GE dispersed base salt are shown in Figure 5-19. There is no change in XRD pattern after dispersing GE concentration. It was observed that there is no change in XRD pattern for base salt and GE dispersed base salt. This confirms that GE is not interfering in any crystals of all nitrate salts. Literature shows that peak related to respective peaks as shown in Table 5-6.

Table 5-6: Literature peak of XRD

Peak Number	Compound	Reference
1	$NaNO_3$	[186]
2	KNO_3	[224]

3	$CaNO_3$	[225]
4	$LiNO_3$	[226, 227]
5	$CsNO_3$	[228]

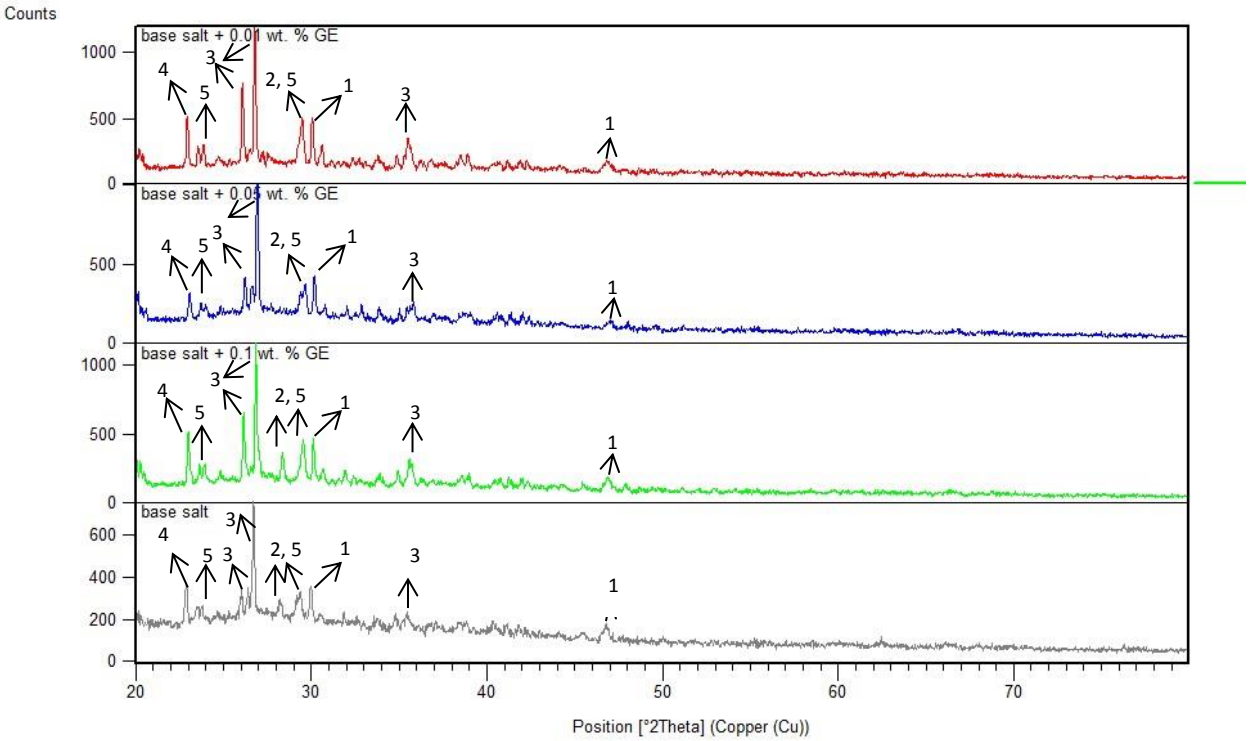

Figure 5-19: XRD graph of base salt and GE dispersed base salt.

5.11 Corrosion Analysis

5.11.1 Copper

Figure 5-20 below shows the image of Cu strips, before and after the corrosion test. Each Cu strip was immersed in molten salt in a glass veil. Several glass veils containing molten salt and GE dispersed molten salts were heated in oven for 24 hours at 100 ± 5 ^{o}C. After the experiment,

samples were cleaned and compared with ASTM copper strip corrosion standards as shown in Figure 5-21.

(a) (b) (c) (d) (e)

Figure 5-20: Copper strips before and after the corrosion test; (a) polished copper strip before the corrosion, (b), (c), (d) and (e) copper strip after the corrosion test in base salt, molten salt dispersed 0.01 wt. % GE, molten salt dispersed 0.05 wt. % GE and 0.1 wt. % GE, respectively.

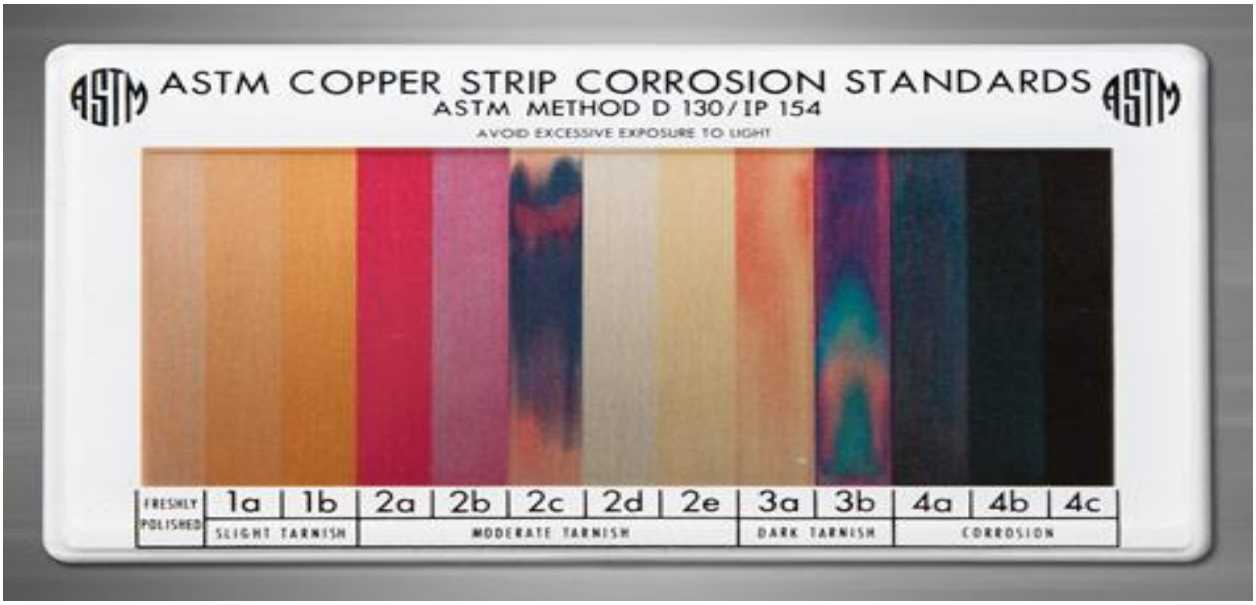

Figure 5-21: ASTM copper strip corrosion standards [210].

By comparing Figure 5-20 with Figure 5-21, It can be observed that base salt and 0.01 wt. % GE dispersed base salt (Figure 5-20 (b) and (c)) are slight tarnished, 0.05 wt. % GE dispersed base salt (Figure 5-20 (d)) was moderately tarnished and 0.1 wt. % GE dispersed base salt (Figure 5-20 (e)) was dark tarnished. None of the copper strips are corroded. More detailed micro and nanoscopic analysis of copper strips are discussed in section 5.11.3, 5.11.5 and 5.11.7.1.

5.11.2 SS304

Same procedure was followed for corrosion test of SS304 as that of copper. Figure 5-22 shows photograph of SS304, before and after the corrosion test. As there is no comparison standard for stainless steel. From Figure 5-22, it can be said that there was no corrosion for SS304. Another way is to analysis the corrosion of SS304 strips are only through SEM and EDX. SEM and EDX analysis are discussed in section 5.11.4, 5.11.6 and 5.11.7.2.

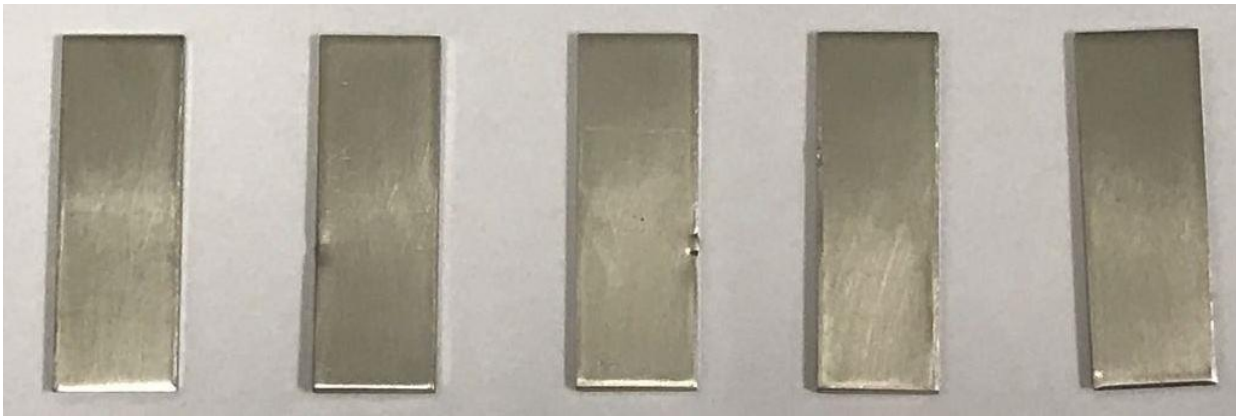

(a) (b) (c) (d) (e)

Figure 5-22: SS304 strips before and after the corrosion test; (a) polished copper strip, (b), (c), (d) and (e) SS304 strip after corrosion test in base salt, molten salt dispersed 0.01, 0.05 and 0.1 wt. %, respectively.

5.11.3 SEM analysis on corrosion of copper

Figure 5-23 shows morphological characterization of copper strips, before and after the corrosion test. There are lots of scratches on all FESEM images, these scratches were occurred while polishing of Cu using silicon carbide paper. Polishing was done to remove rust from Cu strips. By comparing Figure 5-23 (a) with all other SEM images. It can be observed that corrosion rate was increased with increase in GE concentration. The possible reason for increase in corrosion rate with increase in GE concentration is due to weakening of intermolecular bonding of nitrate salts. This weakening is directly related to temperature of nanosuspension. All samples were kept at identical temperature i.e. 100 ± 5 ^{o}C. Due to difference in concentration of GE in all samples, temperature of nanosuspension was variable. The temperature of base salt, 0.01, 0.05 and

0.1 wt. % GE dispersed base salts were measured as 88.4, 93.1, 94.5 and 95.6 ^{o}C, respectively. So, the increase in temperature of nanosuspension makes the weakening of intermolecular bonding of molten salt. Thereby, Cu reacts with oxygen becomes as CuO. Thus, corrosion rate gets increased.

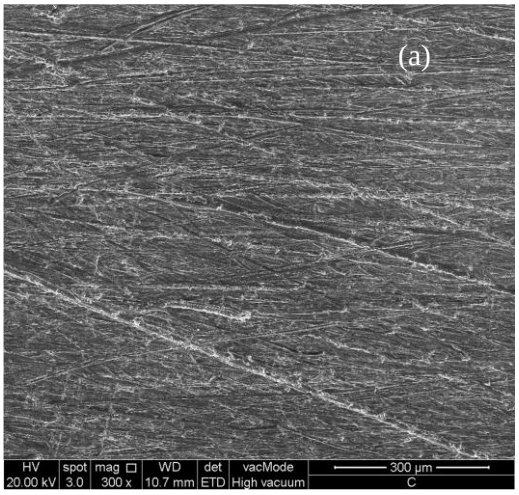

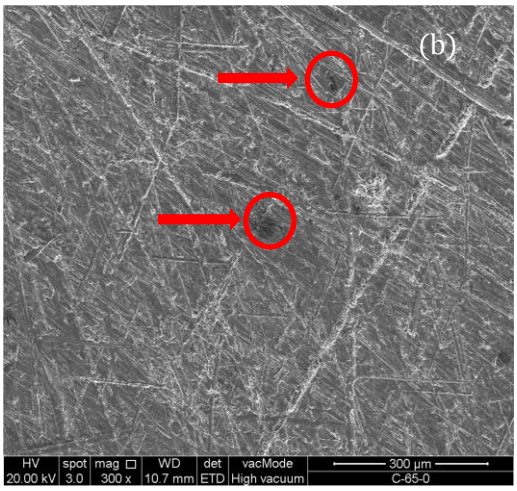

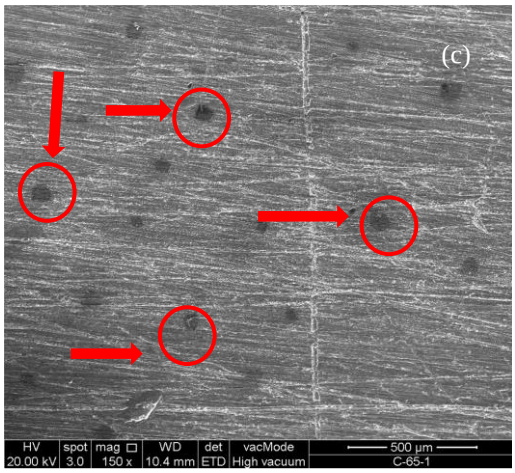

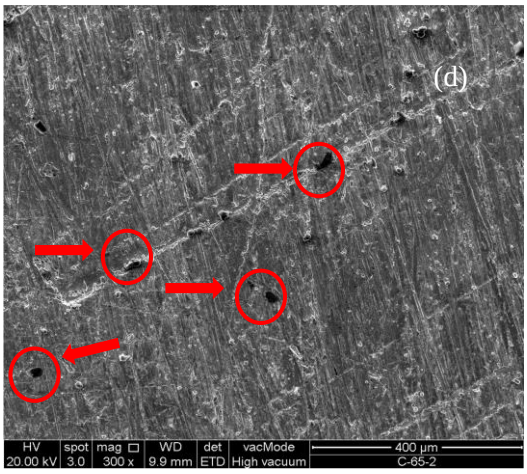

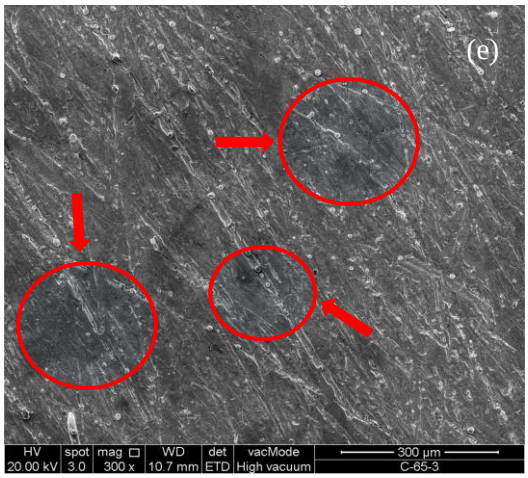

Figure 5-23: Shows SEM analysis of corrosion test on copper strip. **Figure 5-23** (a) is morphology of bare copper strip and (b), (c), (d) and (e) are SEM images of copper strips after corrosion test in base salt, molten salt dispersed 0.01, 0.05 and 0.1 wt. %, respectively.

5.11.4 SEM analysis of Stainless steel

Figure 5-24 shows morphological images characterized with FESEM, before and after the corrosion test of SS304. Figure 5-24 (a) is microscopic image of SS304 before corrosion test. It was observed that lot of scratches on SS304. This was due to polishing of SS304 surface using silicon carbide paper. From Figure 5-24 (b), (c), (d) and (e), it was observed that there are many spots of corrosion on SS304.

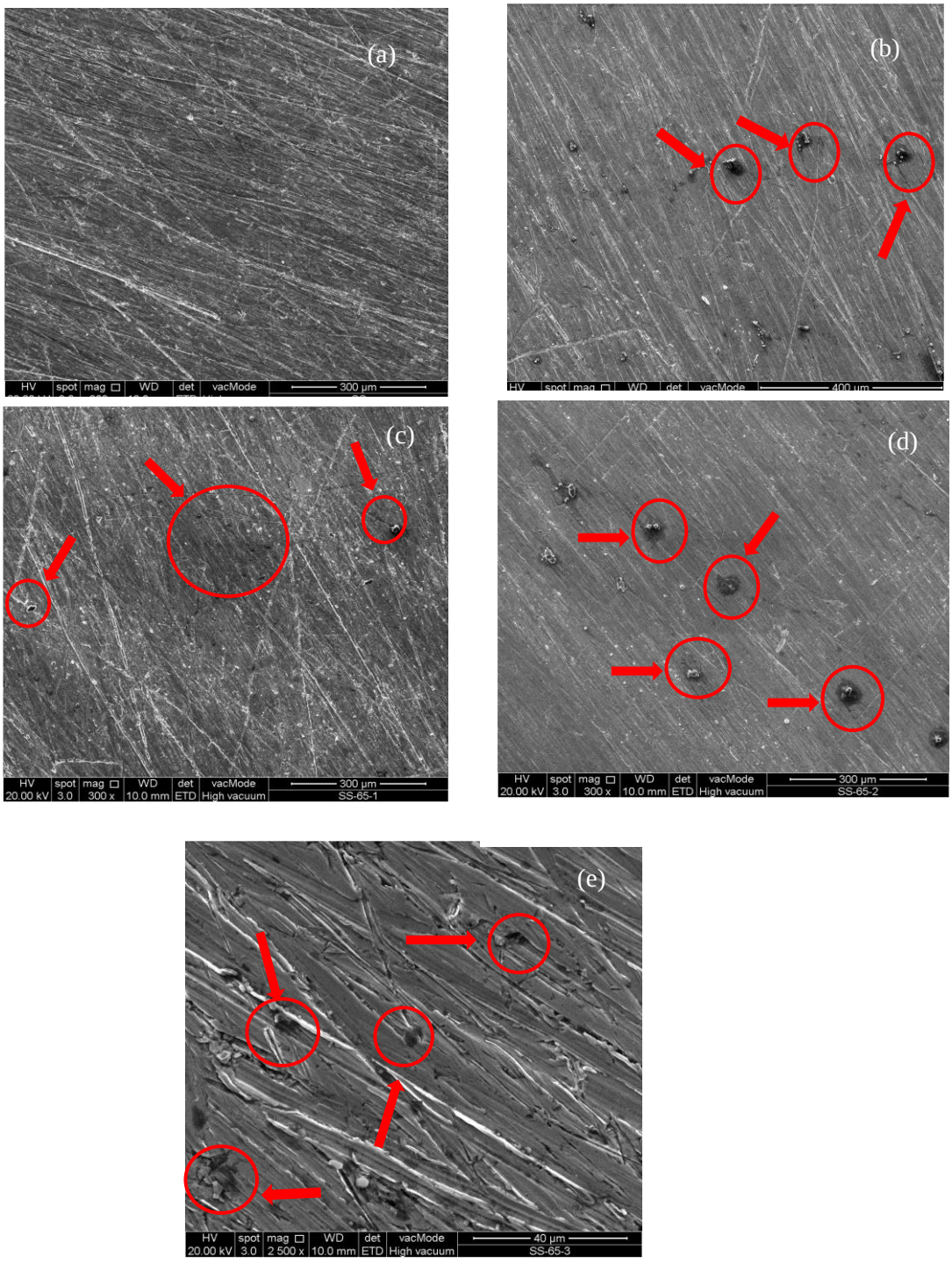

Figure 5-24: shows SEM analysis of corrosion test on SS304 strip. **Figure 5-24** (a) is morphology of bare SS304 strip and (b), (c), (d) and (e) are SEM images of SS304 strips after corrosion test in base salt, molten salt dispersed 0.01, 0.05 and 0.1 wt. %, respectively.

5.11.5 EDX analysis of copper

Figure 5-25 shows the scanned surface areas analyzed through EDX, before and after the corrosion test. From Figure 5-25 (a) and (b), it can be observed that bare Cu strip did not get corroded as there is no presence of oxygen in EDX spectrum. From Figure 5-25 (c), it was observed that Cu got localized corrosion. For the same area, EDX has been done and observed that oxygen was present in the spectrum. Thus, it was concluded that Cu strip got corroded. From Figure 5-25 (e), it can be seen that there are too many corroded spots, and the reason was explained in the section 5.11.3. Chemical analysis (Figure 5-25 (f)) shows that amount of oxygen got increased. This confirms that corrosion rate gets increased with increase in GE concentration in base salt. Similarly, it was observed that corrosion spots also got increased in Figure 5-25 (g) and (i). Figure 5-25 (h) and (j) confirms that the amount of oxygen quantity got increased. Thus, it can be concluded that corrosion rate has increased with increase in GE concentrations in base salt.

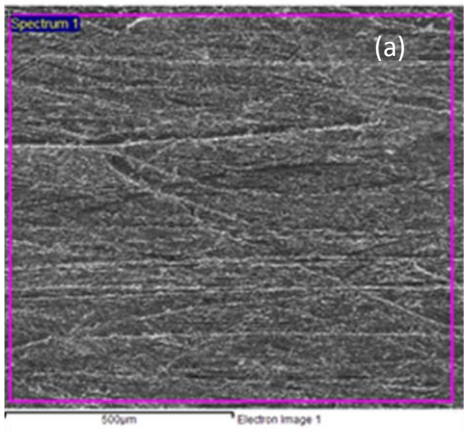

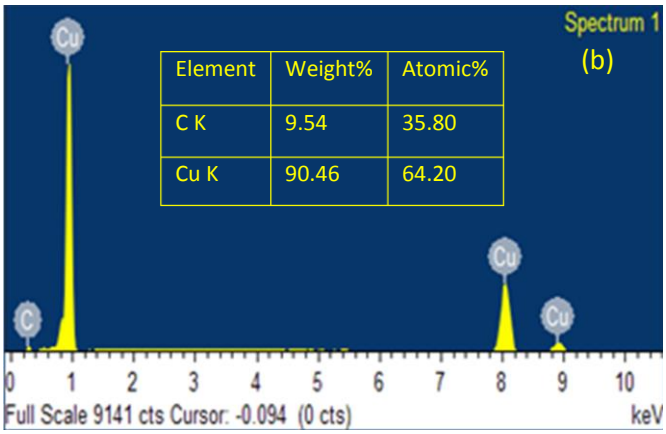

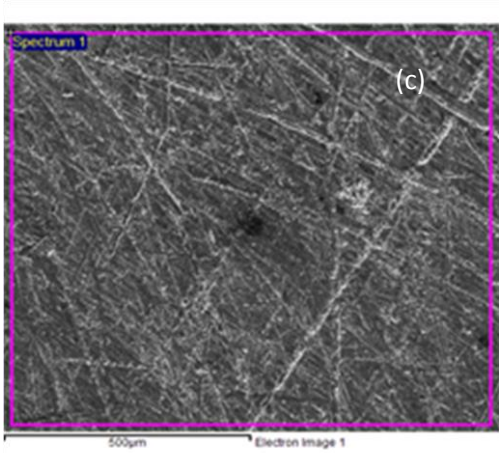
Spectrum 1
(c)
500µm
Electron Image 1

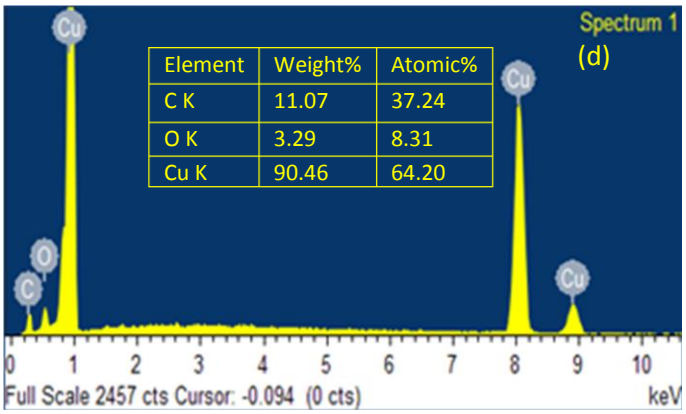
Spectrum 1
(d)
Element | Weight% | Atomic%
C K | 11.07 | 37.24
O K | 3.29 | 8.31
Cu K | 90.46 | 64.20
Cu
O
C
0 1 2 3 4 5 6 7 8 9 10
Full Scale 2457 cts Cursor: -0.094 (0 cts)
keV

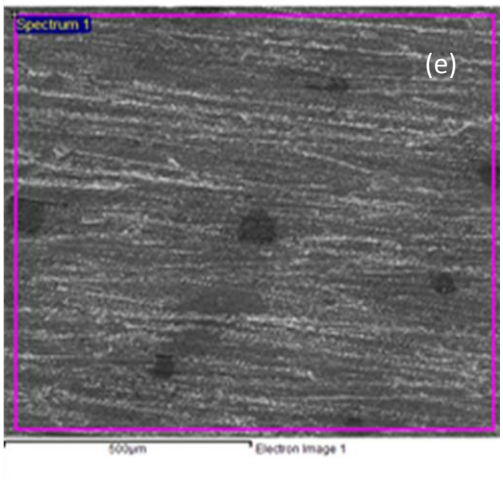
Spectrum 1
(e)
500µm
Electron Image 1

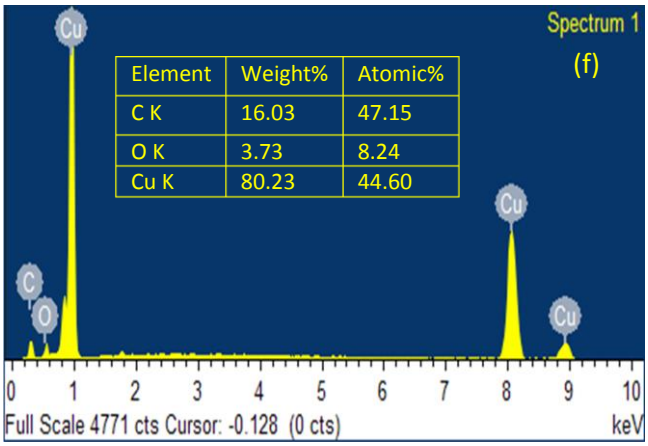
Spectrum 1
(f)
Element | Weight% | Atomic%
C K | 16.03 | 47.15
O K | 3.73 | 8.24
Cu K | 80.23 | 44.60
Cu
C
O
0 1 2 3 4 5 6 7 8 9 10
Full Scale 4771 cts Cursor: -0.128 (0 cts)
keV

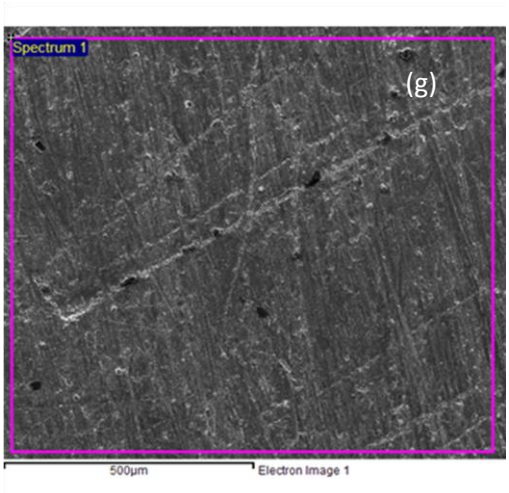
Spectrum 1
(g)
500µm
Electron Image 1

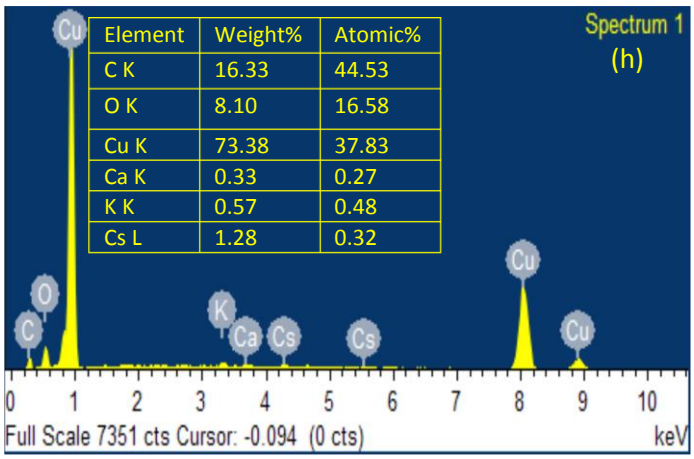
Spectrum 1
(h)
Element | Weight% | Atomic%
C K | 16.33 | 44.53
O K | 8.10 | 16.58
Cu K | 73.38 | 37.83
Ca K | 0.33 | 0.27
K K | 0.57 | 0.48
Cs L | 1.28 | 0.32
Cu
O
C
K
Ca
Cs
Cs
0 1 2 3 4 5 6 7 8 9 10
Full Scale 7351 cts Cursor: -0.094 (0 cts)
keV

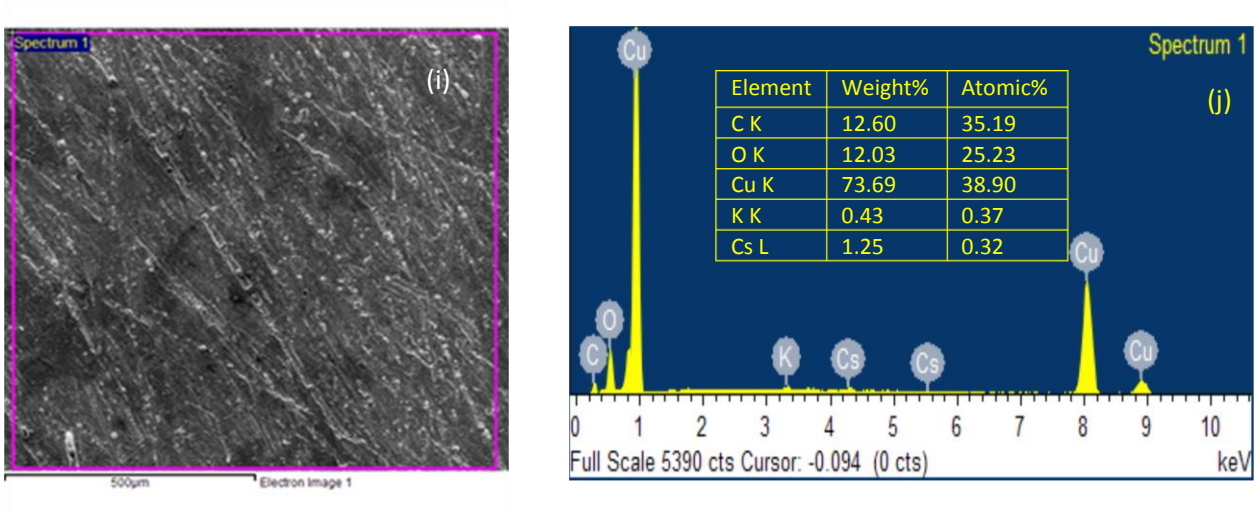

Figure 5-25: (a), (c), (e), (g) and (i) are SEM images, where EDX pattern had scanned. (b), (d) (f) (h) and (j) are EDX pattern of copper strip. (a), (b) are SEM and EDX of bare copper strip. (c), (e), (g) and (i) are SEM images and (b), (d), (f), (h) and (j) are EDX pattern of copper strips after corrosion test with base salt, base salt dispersed with 0.01, 0.05 and 0.1 wt. % GE concentration.

5.11.6 EDX analysis of SS304

Figure 5-26 shows the scanned surface areas analyzed through EDX, before and after the corrosion test. From Figure 5-26 (a) and (b), it can be observed that bare SS304 strip did not get corroded as there is no oxygen in EDX spectrum. From Figure 5-26 (c), it is observed that SS304 have localized corrosion. EDX analysis (Figure 5-26 (d)) shows that oxygen element present in the spectrum. Thus, it can be concluded that SS304 strip gets corroded in presence of base salt. From Figure 5-26 (e), (g) and (i), it can also be viewed for few corrosion spots. Based on EDX analysis, amount of oxygen quantity remained the same before and after the

corrosion test of SS304. From this it can be concluded that amount of corrosion rate before and after dispersion of GE in base salt is constant. Similarly, corrosion spots for base salt dispersed with 0.01, 0.05 and 0.1 wt. % GE were observed. However, based on EDX analysis as shown in Figure 5-26 (f), (h) and (j), revealed that the amount of oxygen approximately remained the same. This can be understood in such a way that growth of oxides (such as FeO, NiO, CrO) forms a protective layer to avoid diffusion growth of oxygen in SS304.

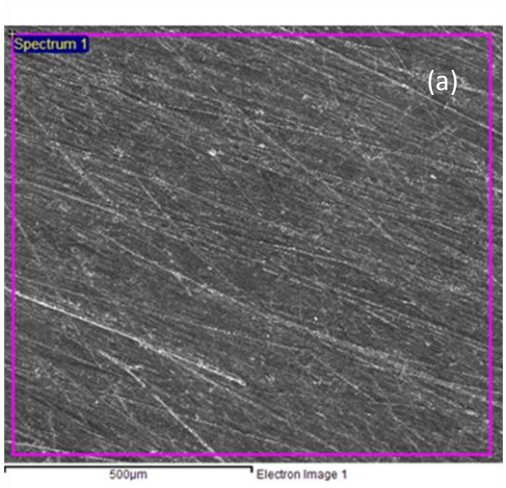

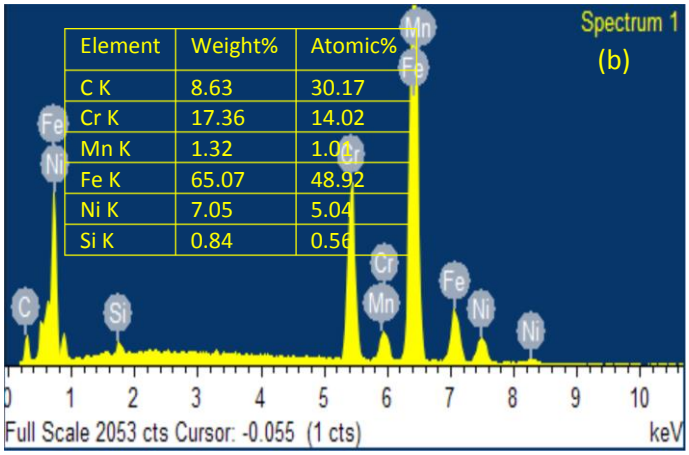

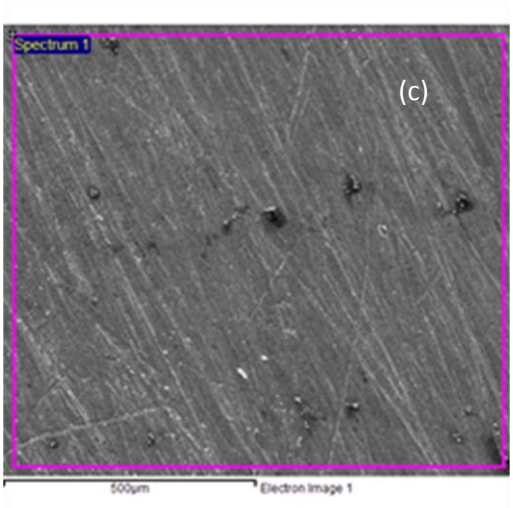

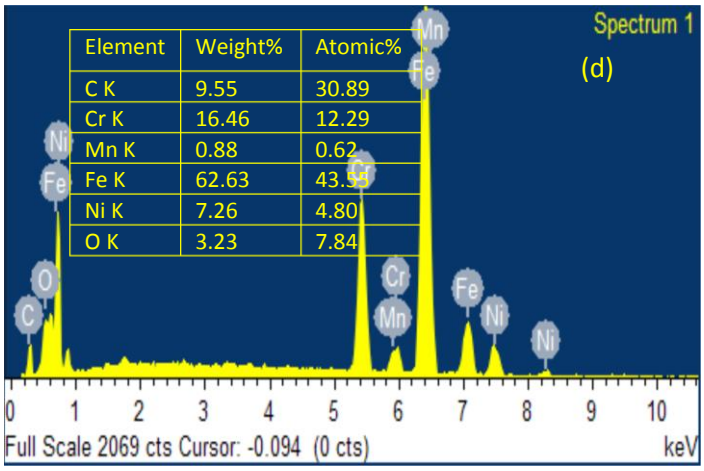

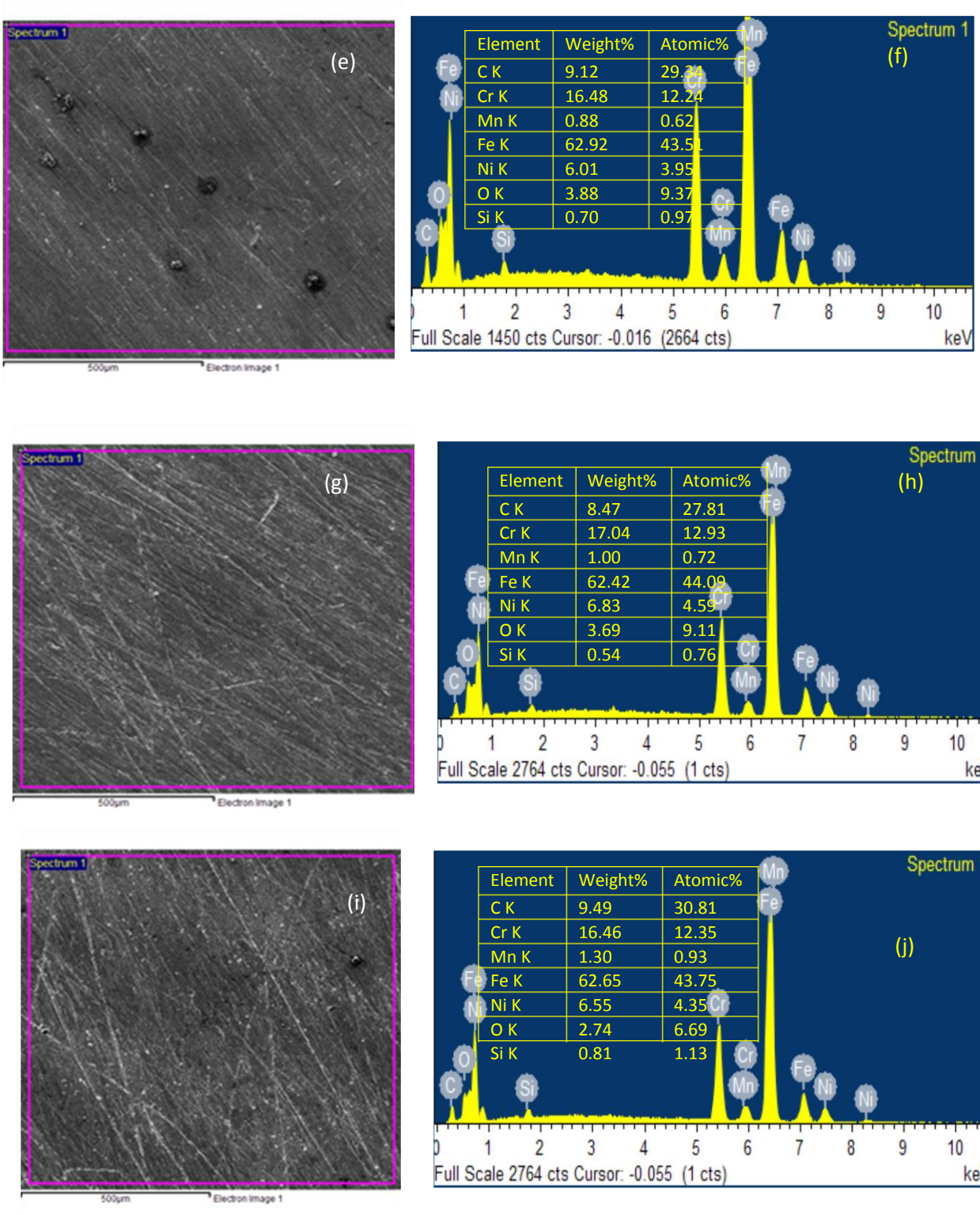

Figure 5-26: (a), (c), (e), (g) and (i) are SEM images, where EDX pattern had scanned. (b), (d) (f) (h) and (j) are EDX pattern of SS304 strip. (a), (b) are SEM and EDX of bare SS304 strip. (c), (e), (g) and (i) are SEM

images of copper strips after corrosion test with base salt, base salt dispersed with 0.01, 0.05 and 0.1 wt. % GE concentration and (d), (f), (h) and (j) are EDX pattern, respectively.

5.11.7 XRD analysis of Copper and SS304

5.11.7.1 Low temperature corrosion test of Copper

Figure 5-27 shows X-ray diffraction spectra of Cu strips, before and after low temperature corrosion test. All these peaks match with ICSD card number: 98 005 5320. Major peaks were found to be at 43.50, 50.62 and 74.28 degrees in 2theta position. Copper peaks are related to crystal lattice of (1 1 1), (2 0 0) and (2 2 0) [229]. So from XRD graphs, it was found that peaks positions are unaltered. This confirms that Cu material did not got corroded after corrosion test.

5.11.7.2 Low temperature corrosion test of SS304

X-ray diffraction spectra of SS304 strips, before and after low temperature corrosion test are shown in Figure 5-28. SS304 test were done in base salt and GE dispersed base salt. Figure 5-28 is also a comparison of SS304 strip before and after corrosion test. From XRD graphs, it was found that peaks positions are unaltered. This confirms that SS304 material did not got corroded after corrosion test. For 0.01 wt. % GE dispersed in base salt, that new peak was observed at 26.70 degrees, but later came to know that it was because of instrument error.

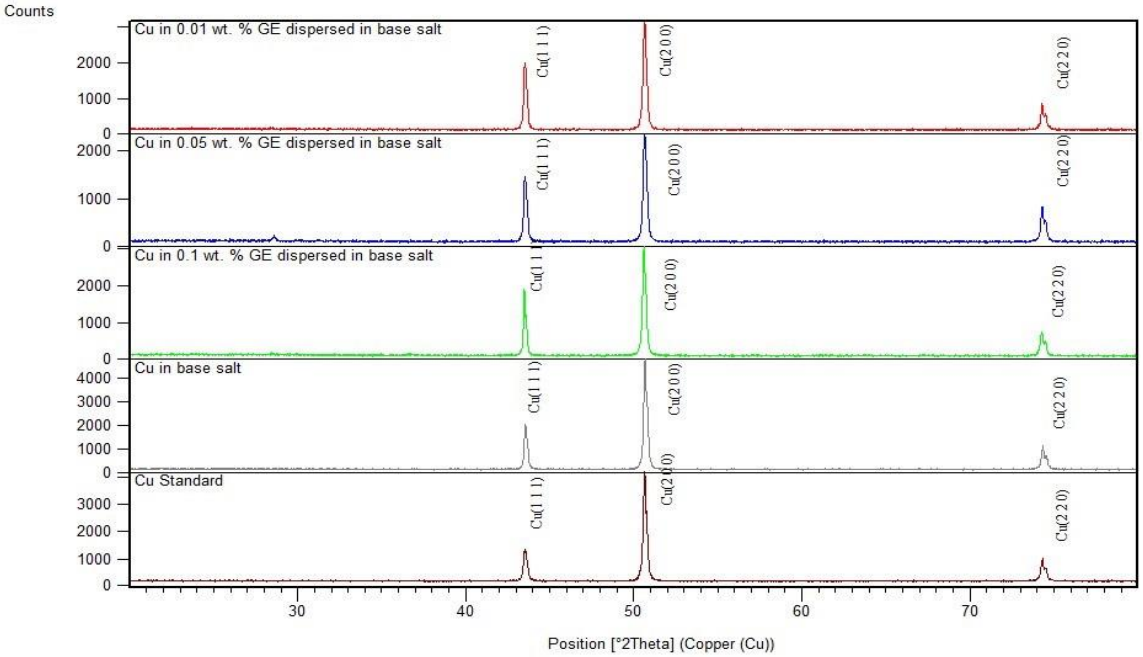

Figure 5-27: shows low temperature corrosion test on copper strip. Cu standard is XRD of bare copper strip and remaining XRD patterns are of Cu strips after corrosion test in base salt, base salt dispersed in 0.01, 0.05 and 0.1 wt. %, respectively.

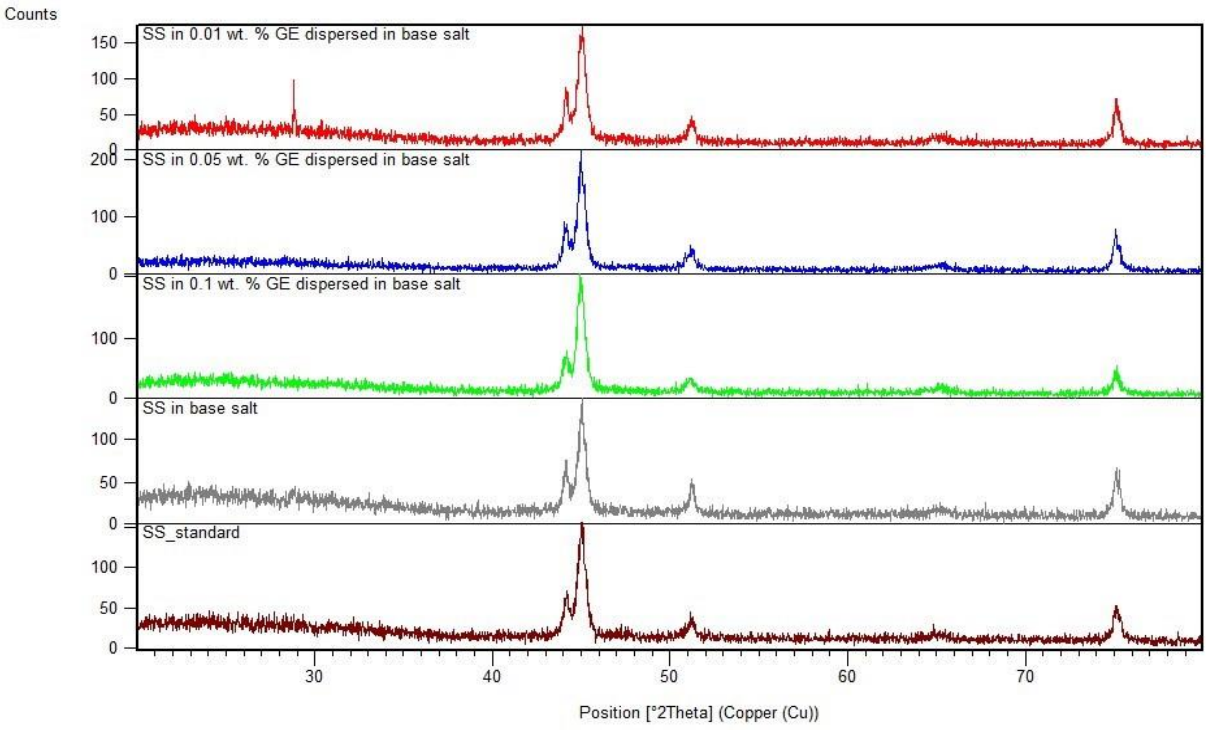

Figure 5-28: shows low temperature corrosion test on SS304 strip. SS standard is XRD of bare SS304 strip and remaining XRD patterns are of SS strips after corrosion test in base salt, base salt dispersed in 0.01, 0.05 and 0.1 wt. %, respectively.

5.11.8 High temperature corrosion test

5.11.8.1 Copper

High temperature corrosion test was performed on SS304 and copper material. Test method was conducted by following ISO 17245 protocol. Test was performed in a furnace with specimen placed in porcelain bowl. Then porcelain bowl was filled with molten salt, so that whole specimen (SS304 and copper) should get immersed. Four copper (or) SS304 were

placed in each porcelain bowl and kept in furnace for duration of 500 hours. Furnace temperature was maintained at 500 ^{o}C. After every 60-70 hour, molten salt was added, so that specimen strips should be completely immersed all time. Figure 5-29 shows that copper strips dipped in molten salt and GE dispersed molten salt. Snapshot was taken after cooling and removing molten salt from copper specimens. Detailed analyses of copper strips under high temperature corrosion test are discussed through SEM, EDX and XRD in section 5.11.8.3, 5.11.9 and 5.11.9.1.

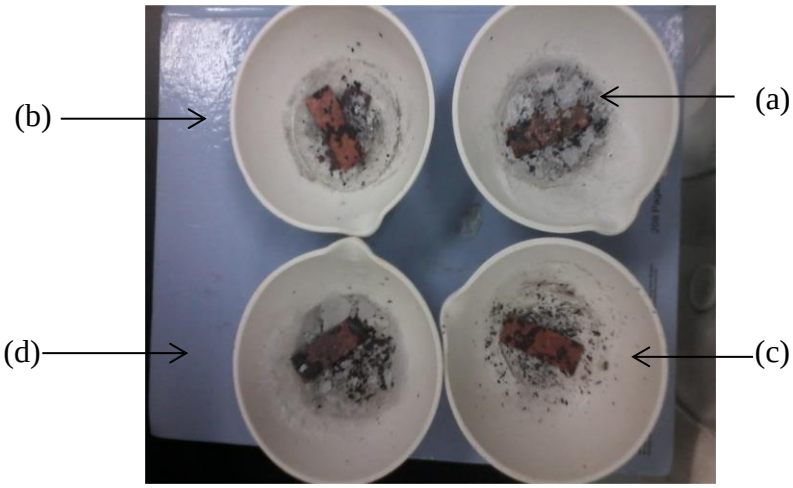

Figure 5-29: Snapshot of copper strips after corrosion test; (a), (b), (c) and (d) are copper strips after high temperature corrosion test in base salt, eutectic salt dispersed 0.01, 0.05 and 0.1 wt. % GE, respectively.

5.11.8.2 Stainless Steel 304

Same procedure was followed of ISO 17245 as that of copper strips. Figure 5-30 shows snapshot of SS304 strips after corrosion test. From Figure 5-30, it can be said that SS034 strips are completely corroded.

Another way to analysis the corrosion of SS304 strips are through SEM, EDX and XRD analysis are discussed in section.

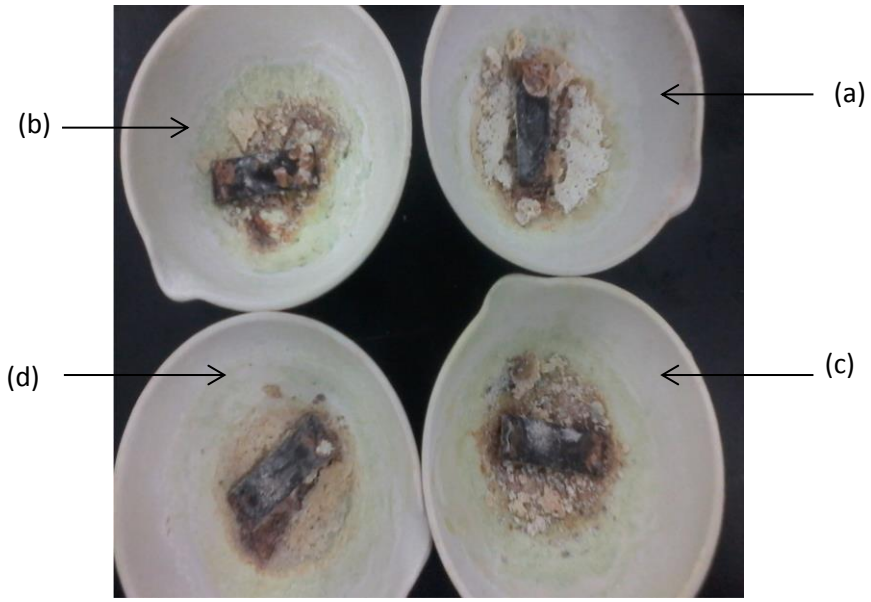

Figure 5-30: Snapshot of SS304 strips after corrosion test; (a), (b), (c) and (d) are copper strips after high temperature corrosion test in base salt, eutectic salt dispersed 0.01, 0.05 and 0.1 wt. % GE, respectively.

5.11.8.3 SEM analysis of copper

Figure 5-31 shows morphological characterization of copper strips, after corrosion test. It can be observed that after corrosion test Cu material gets peel out of the strip. By microscopically analyzing all SEM images, it can be observe that corrosion is obvious in base salt and GE dispersed base salt. Corrosion rate is due to nitrate salts interact with Cu material and Cu material will gets oxidize to CuO. CuO gets released in to molten salt due to (i) gravitational force and (ii) breaking of bond between CuO and Cu.

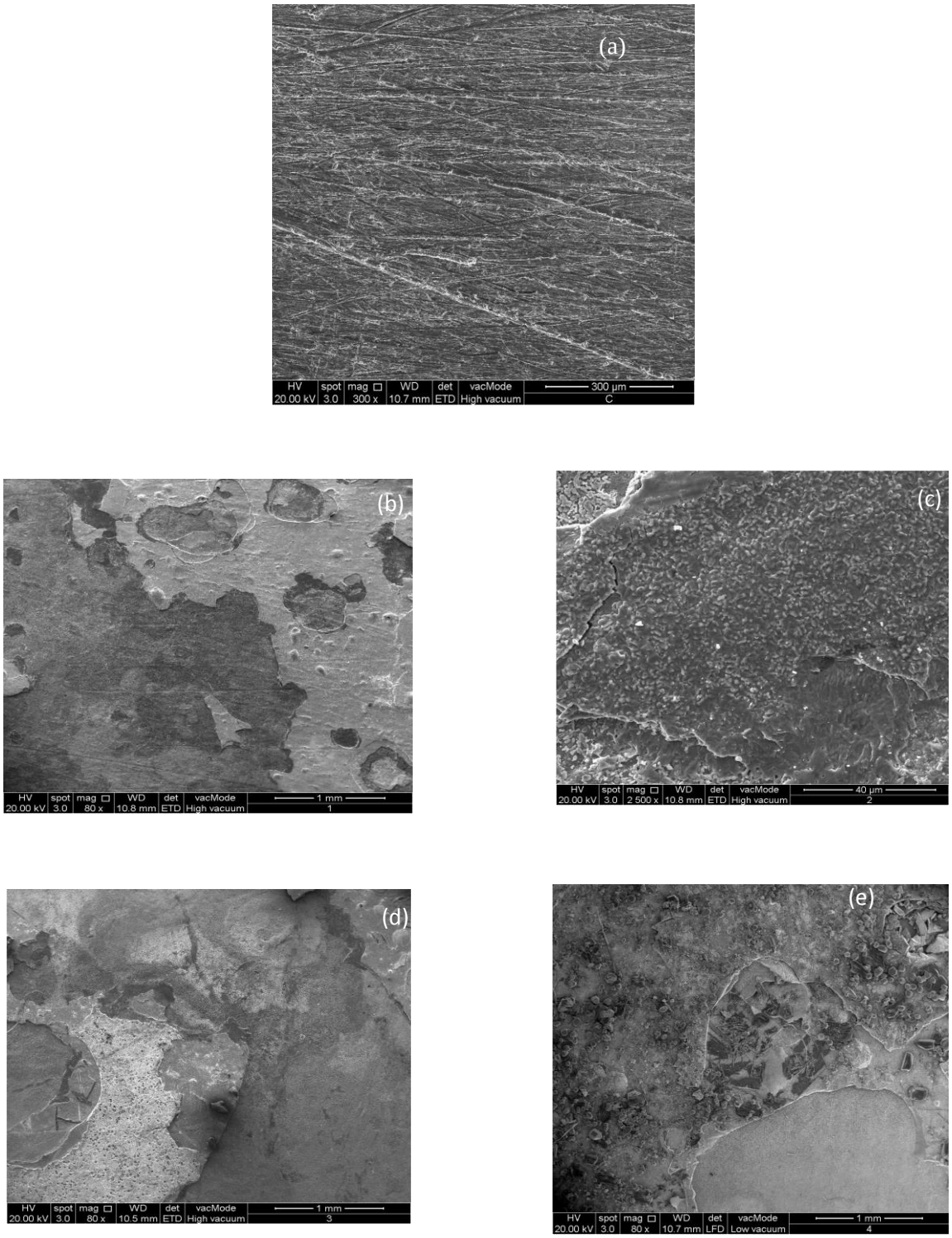

Figure 5-31: shows SEM analysis of corrosion test on copper strip. **Figure 5-31** (a) is morphology of bare copper strip and (b), (c), (d) and (e) are SEM images of copper strips after corrosion test in base salt, eutectic salt dispersed 0.01, 0.05 and 0.1 wt. %, respectively.

5.11.9 EDX analysis of copper

Figure 5-32 shows the scanned surface areas analyzed through EDX, before and after high temperature corrosion test. Figure 5-32 (a) and (b), is the analysis of bare Cu strip. From Figure 5-32 (c), (e), (g) and (i), it was observe that Cu strips are peeling out. By doing EDX on the same area, it was observe that the presence of oxygen compound. This means that Cu got corroded. By analyzing the amount of oxygen quantity in EDX spectrum, it can be concluded that corrosion rate is constant for base salt and GE dispersed base salt.

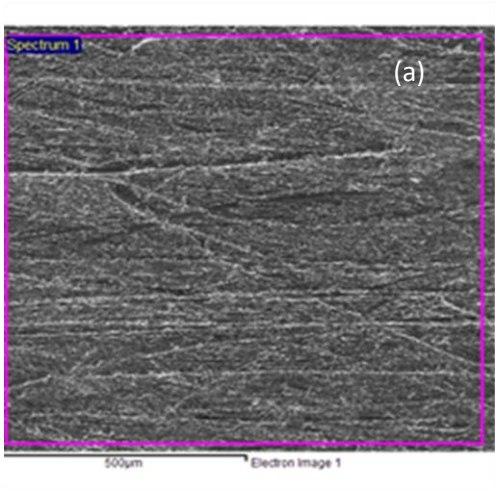

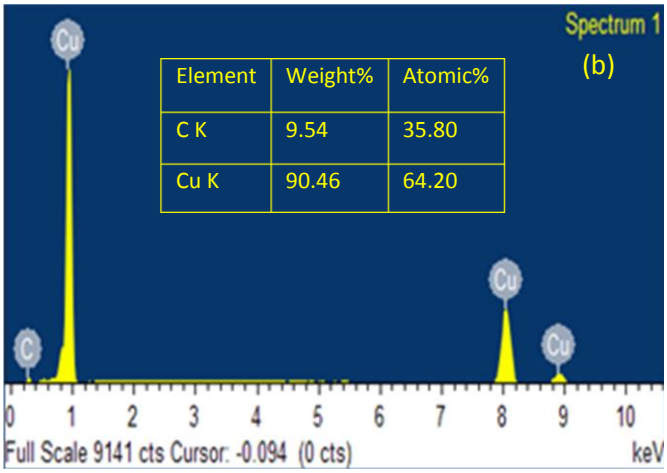

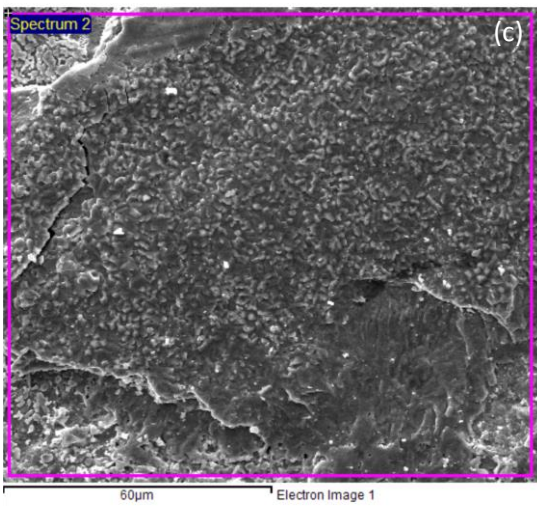
Spectrum 2
(c)
60µm
Electron Image 1

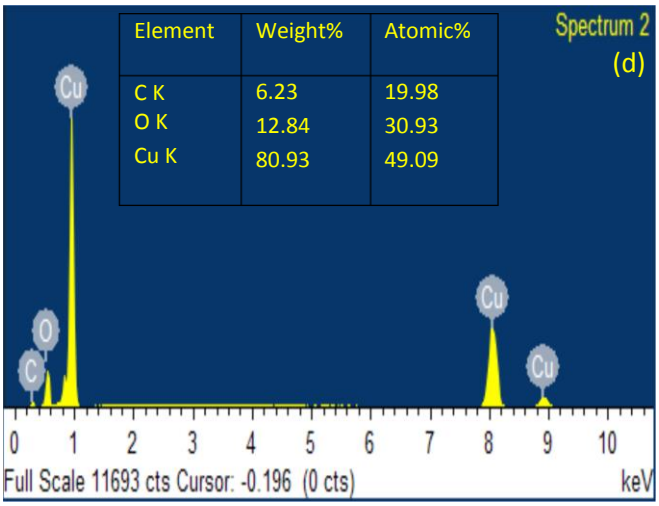
Element | Weight% | Atomic%
C K | 6.23 | 19.98
O K | 12.84 | 30.93
Cu K | 80.93 | 49.09
Spectrum 2
(d)
Cu
O
C
Cu
Cu
0 1 2 3 4 5 6 7 8 9 10
Full Scale 11693 cts Cursor: -0.196 (0 cts)
keV

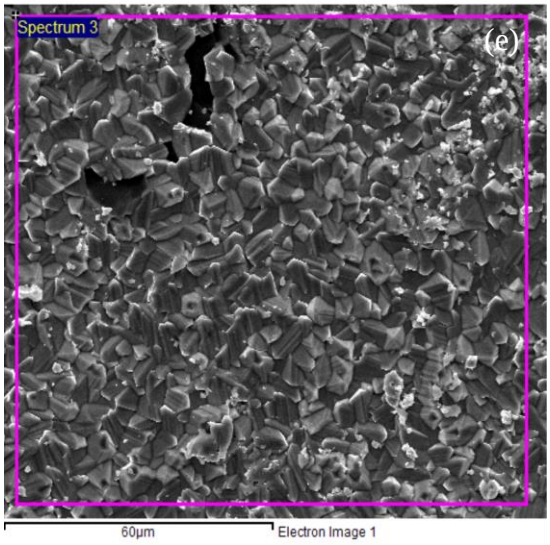
Spectrum 3
(e)
60µm
Electron Image 1

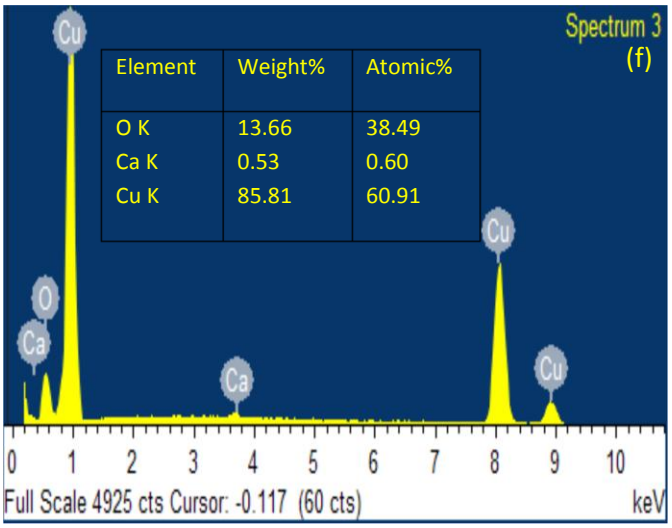
Element | Weight% | Atomic%
O K | 13.66 | 38.49
Ca K | 0.53 | 0.60
Cu K | 85.81 | 60.91
Spectrum 3
(f)
Cu
O
Ca
Ca
Cu
Cu
0 1 2 3 4 5 6 7 8 9 10
Full Scale 4925 cts Cursor: -0.117 (60 cts)
keV

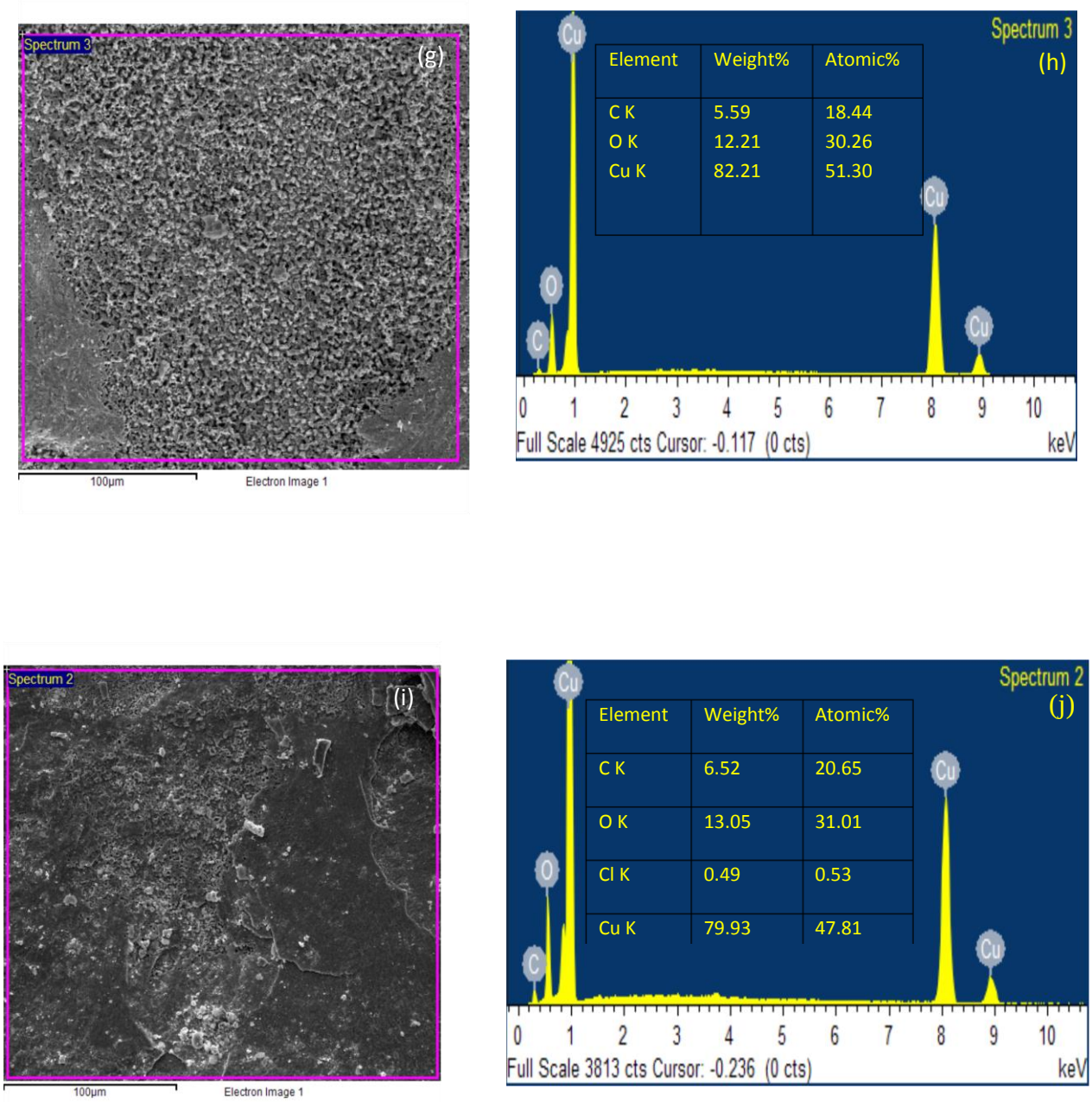

Figure 5-32: (a), (c), (e), (g) and (i) are SEM images, where EDX pattern had scanned. (b), (d) (f) (h) and (j) are EDX pattern of copper strip. (a), (b) are SEM and EDX of bare copper strip. (c), (e), (g) and (i) are SEM images of copper strips after corrosion test with base salt, base salt dispersed with 0.01, 0.05 and 0.1 wt. % GE concentration and (d), (f), (h) and (j) are EDX pattern, respectively.

5.11.9.1 High temperature corrosion test of copper

X-ray diffraction spectra of Cu strips, before and after high temperature corrosion test are shown in Figure 5-33. Corrosion test were done in base salt and GE dispersed base salt. Figure 5-33 is also a comparison of Cu strip before and after corrosion test. After corrosion test, Cu material is completely getting oxidize to form CuO. A copper ion reacts with nitrate ions to form CuO. For standard Cu as shown in Figure 5-33, Major peaks found in diffraction pattern are of Cu. Copper peaks are related to crystal lattice of (1 1 1), (2 0 0) and (2 2 0) [229]. Figure 5-33 also shows presence of peak due to CuO at 36.5^{o}, 42.5^{o} and 61.4^{o} which confirms monoclinic structure [230].

5.11.9.1.1 SEM analysis of SS304

Figure 5-34 shows morphological images characterized with FESEM, after the corrosion test of SS304. From Figure 5-34 (a), (b), (c) and (d), it was observed that small portion of SS304 is peeling out. This is due to molten salt and GE dispersed molten salt reacts with the composition of SS304 to become as respective oxide material.

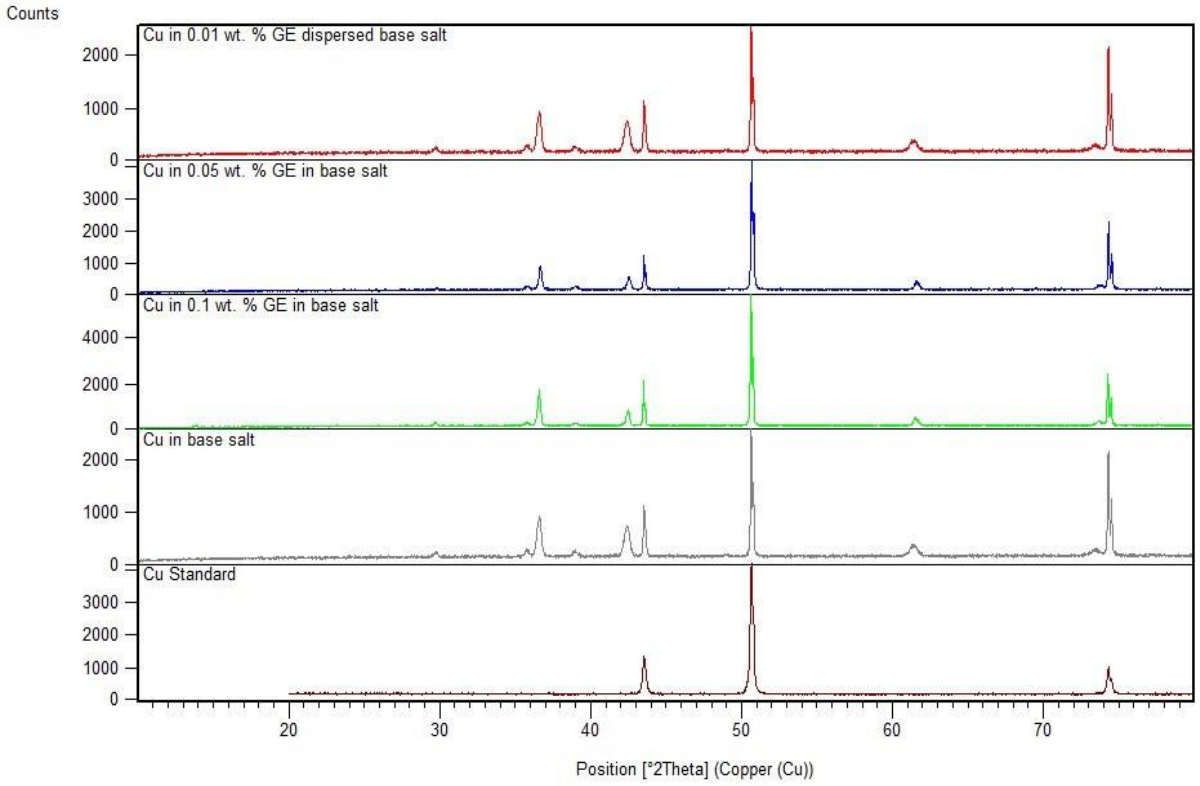

Figure 5-33: shows high temperature corrosion test on copper strip. Cu standard is XRD of bare copper strip and remaining XRD patterns are of Cu strips after corrosion test in base salt, base salt dispersed in 0.01, 0.05 and 0.1 wt. %, respectively.

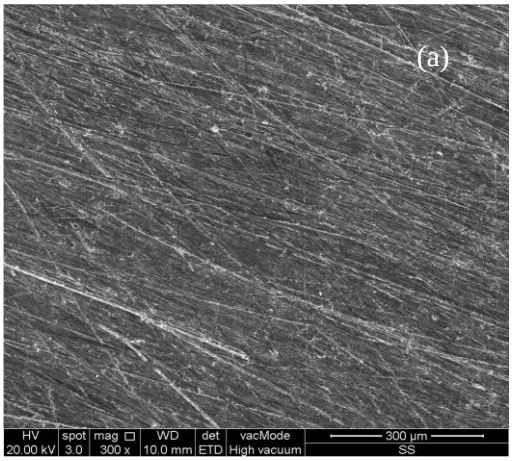

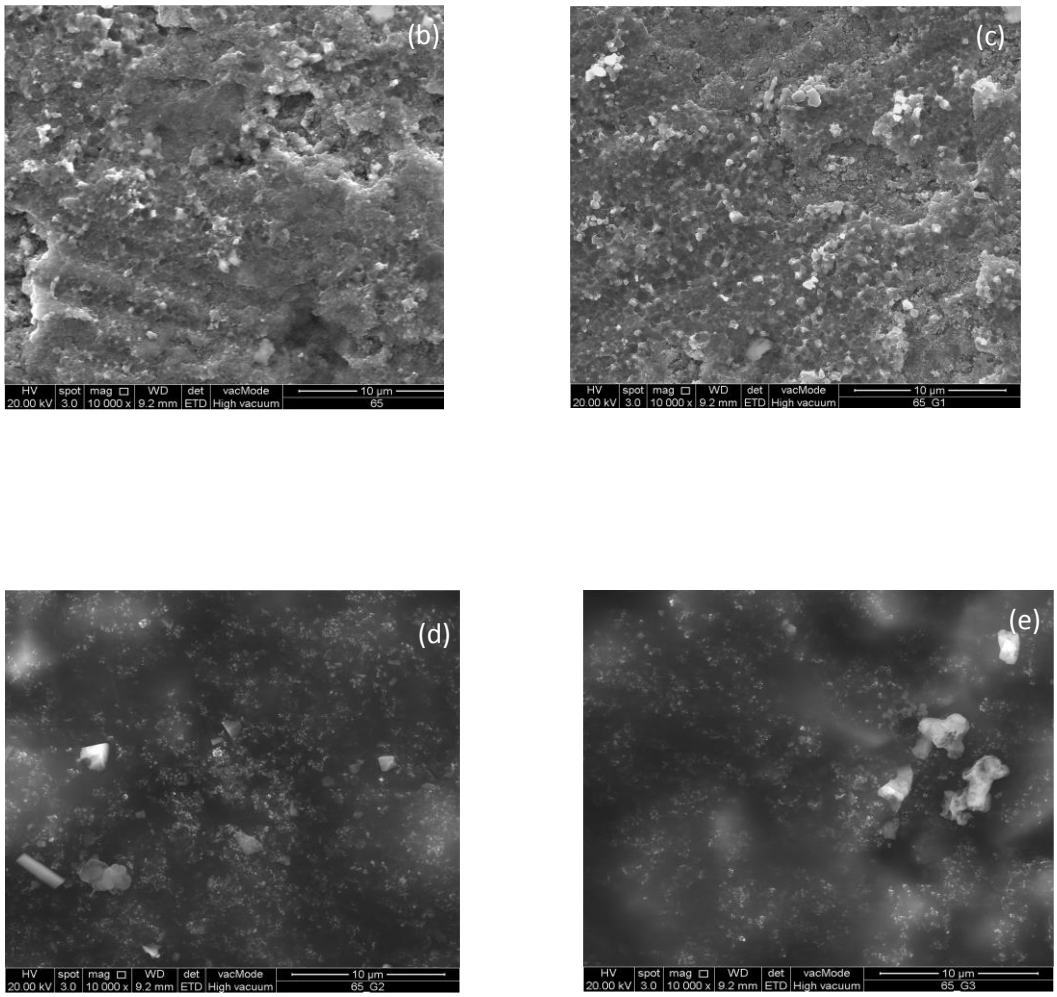

Figure 5-34: shows SEM analysis of corrosion test on SS304 strip. (a) is morphology of bare SS304 strip and (b), (c), (d) and (e) are SEM images of SS304 strips after corrosion test in base salt, eutectic salt dispersed 0.01, 0.05 and 0.1 wt. %, respectively.

5.11.9.2 EDX analysis of SS304

Figure 5-35 shows the scanned surface areas of SS304 analyzed through EDX, before and after corrosion test. Figure 5-35 (a) and (b), it was analyzed that SS304 did not get corroded as there was no oxygen

component in EDX spectrum. From Figure 5-35 (c), (e), (g) and (i), it was observed that SS304 strips are peeling out. From EDX spectrum in Figure 5-35 (d), (f), (h) and (j), it was observed that O is present in all specimens after corrosion test and amount of O is almost the same in elemental analysis. For this it can be concluded that corrosion rate is same in base salt and GE dispersed base salt.

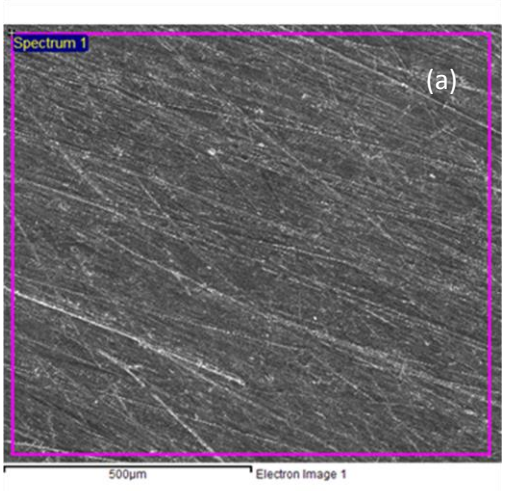

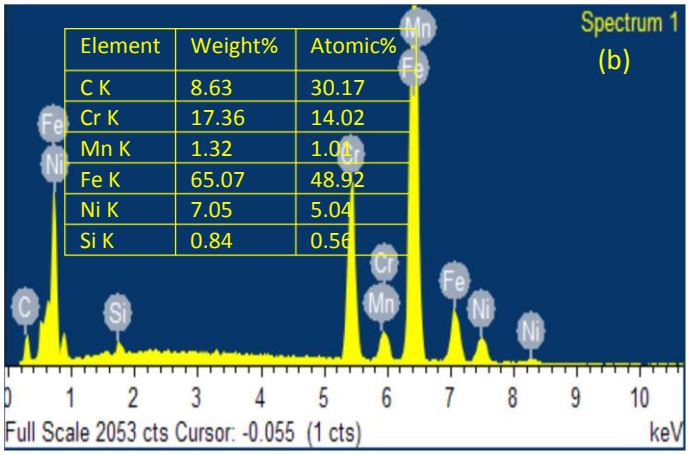

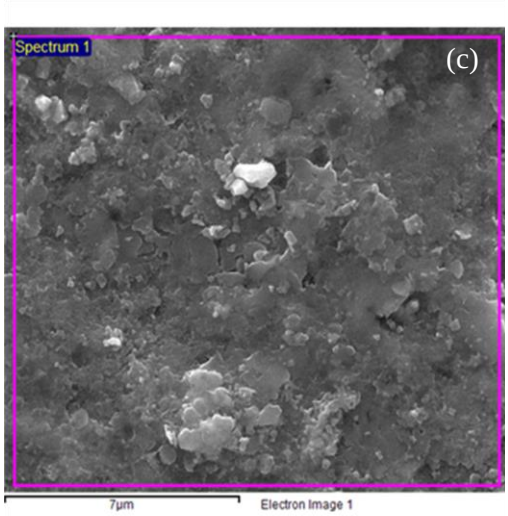

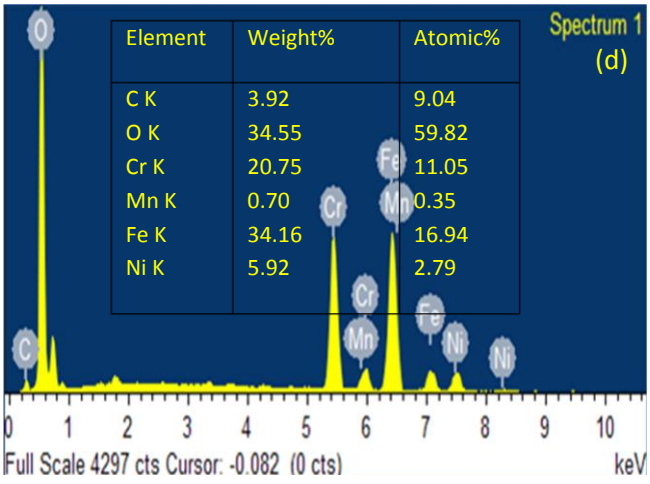

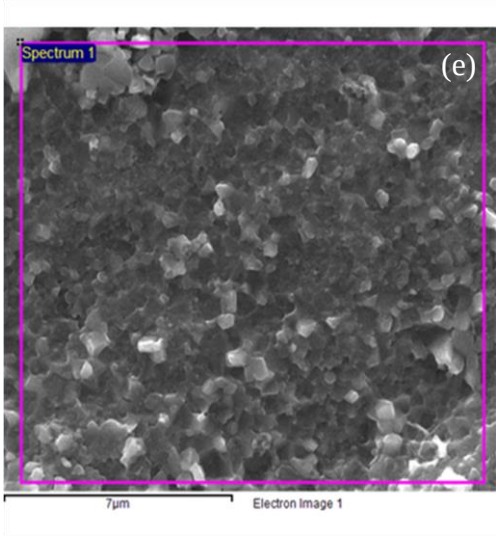
Spectrum 1
(e)
7µm
Electron Image 1

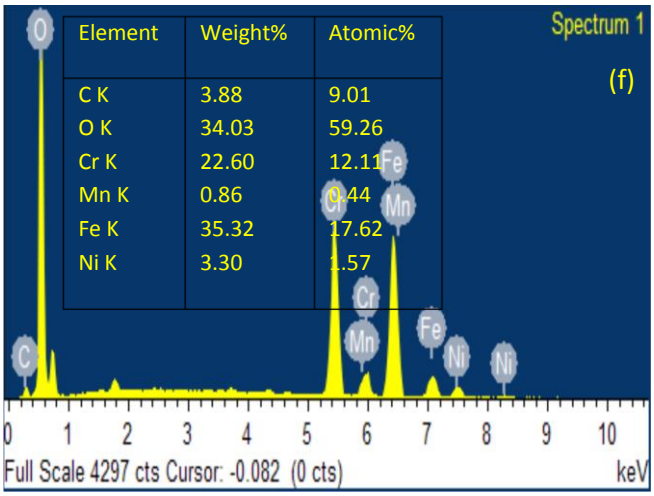
Element | Weight% | Atomic%
C K | 3.88 | 9.01
O K | 34.03 | 59.26
Cr K | 22.60 | 12.11
Mn K | 0.86 | 0.44
Fe K | 35.32 | 17.62
Ni K | 3.30 | 1.57
Spectrum 1
(f)
0 1 2 3 4 5 6 7 8 9 10
Full Scale 4297 cts Cursor: -0.082 (0 cts)
keV

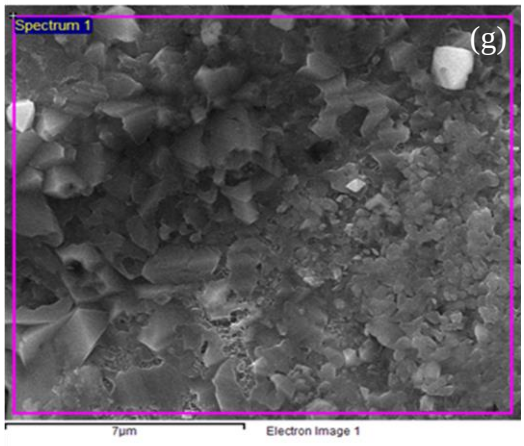
Spectrum 1
(g)
7µm
Electron Image 1

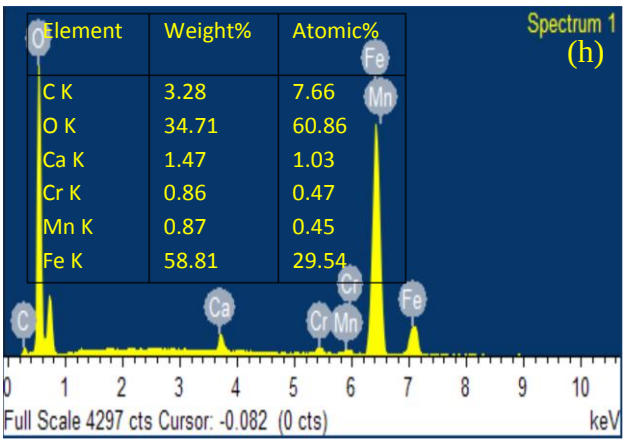
Element | Weight% | Atomic%
C K | 3.28 | 7.66
O K | 34.71 | 60.86
Ca K | 1.47 | 1.03
Cr K | 0.86 | 0.47
Mn K | 0.87 | 0.45
Fe K | 58.81 | 29.54
Spectrum 1
(h)
0 1 2 3 4 5 6 7 8 9 10
Full Scale 4297 cts Cursor: -0.082 (0 cts)
keV

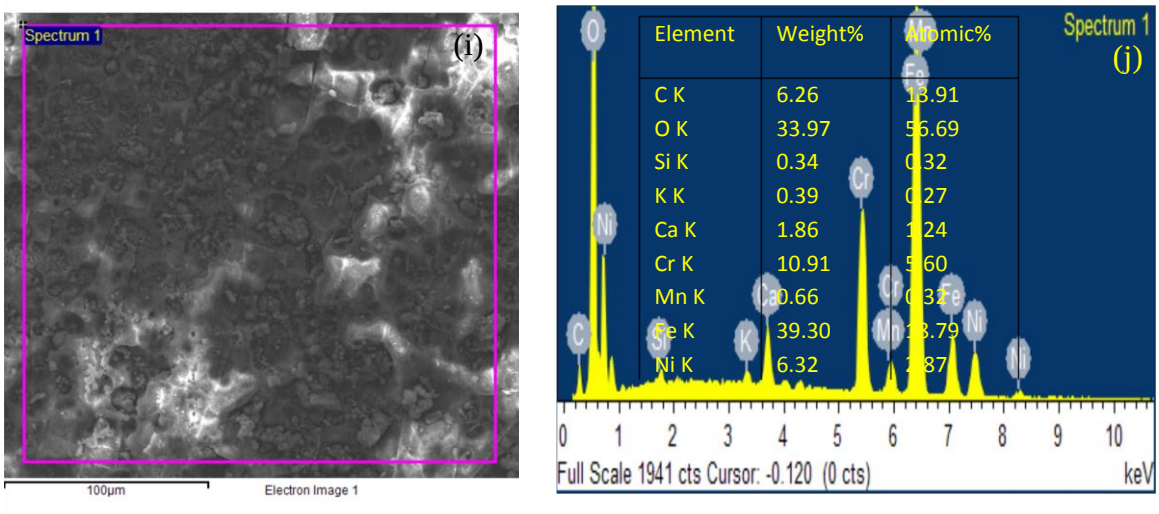

Figure 5-35: (a), (c), (e), (g) and (i) are SEM images, where EDX pattern had scanned. (b), (d) (f) (h) and (j) are EDX pattern of SS304 strip. (a), (b) are SEM and EDX of bare SS304 strip. (c), (e), (g) and (i) are SEM images of copper strips after corrosion test with base salt, base salt dispersed with 0.01, 0.05 and 0.1 wt. % GE concentration and (d), (f), (h) and (j) are EDX pattern, respectively.

5.11.9.3 High temperature corrosion test of SS304

X-ray diffraction spectra of SS304 strips, before and after high temperature corrosion test are shown in Figure 5-36. Corrosion test were done in base salt and GE dispersed base salt. Figure 5-36 is also a comparison of SS304 strip before and after corrosion test. After corrosion test, SS304 material is completely getting oxidize to form its composition oxides (ex: CuO, MnO, FeO etc). As metallic composition reacts with nitrate ions to form its respective metal oxides.

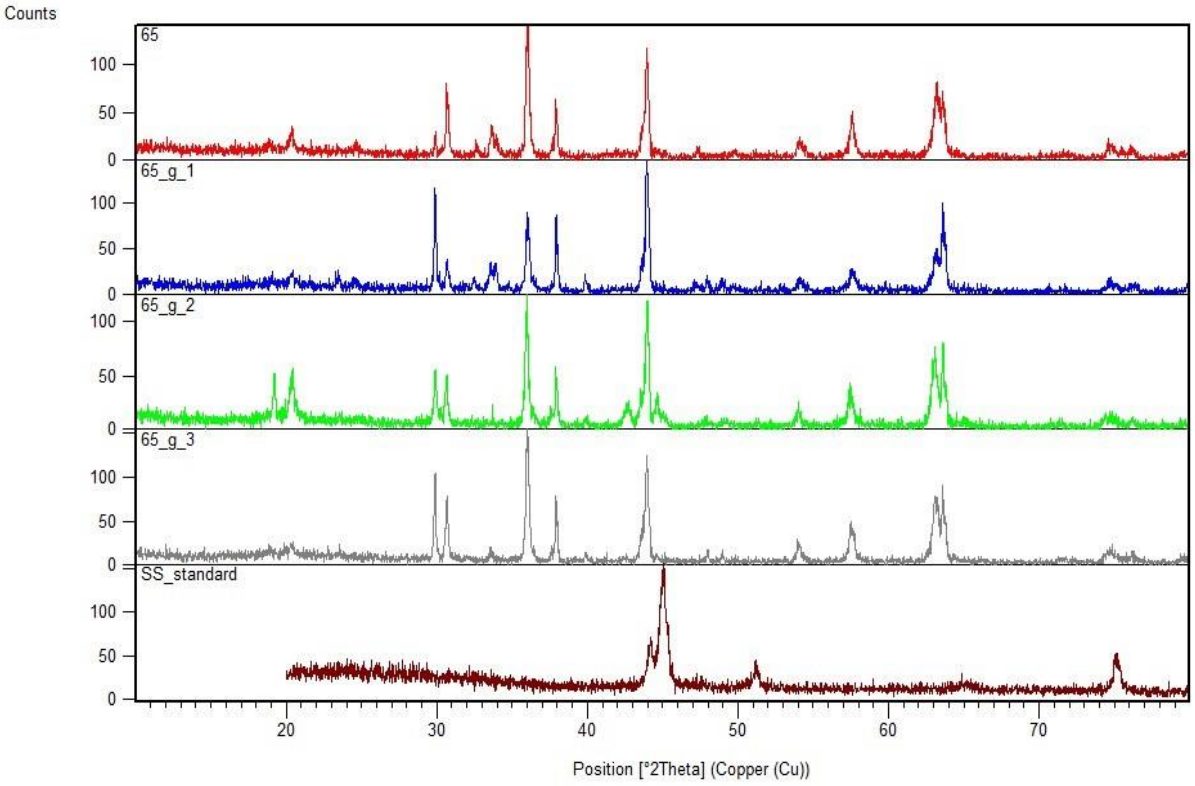

Figure 5-36: shows high temperature corrosion test on SS304 strip. SS standard is XRD of bare SS304 strip and remaining XRD patterns are of SS strips after corrosion test in base salt, base salt dispersed in 0.01, 0.05 and 0.1 wt. %, respectively.

5.12 Kinetic studies

TGA can also been used to study the thermal dissociation of liquid nitrate molecules. Model free kinetic was used for non-isothermal measurements of nitrate and GE dispersed nitrate molecules [231]. E is activation energy

$$E_{\alpha} = \sum_{i=1}^{n} \sum_{j \neq i}^{n} \frac{J[E_{\alpha}, T_i(t_{\alpha})]}{J[E_{\alpha}, T_f(t_{\alpha})]} \qquad \textbf{Eq. 5-1}$$

Where i and j are arbitrary constant under which different heating rates. J is calculated using trapezoid rule. Minimization procedure was iterated for each α to get activation energy. This method was successful to calculate kinetic energy of inorganic materials.

Where t is temperature and α is extent of conversion.

In model free kinetic, activation energy was directly calculated from TGA curves. Temperature is one of the major parameter in rate of degradation. In order to reduce errors sample mass of all samples are taken almost identical. For activation energy, we have programmed TGA in such a way that TGA curve should display of its sample (excluding moisture content). After weighing of sample, sample was heated to 180 ^{o}C and then given hold time of 10 min. This protocol makes vaporization of water content. Then again sample is cooled down to 25 ^{o}C. Then sample is heated to 850 ^{o}C, to know the kinetic parameters of the sample. N_2 as purge gas maintained at flow rate of 20 ml/min.

At the top left of Figure 5-37, shows TGA analysis of base salt at three different heating rates i.e., 5, 10 and 15 ^{o}C. At the bottom left of Figure 5-37 is the decomposition of samples in percentage with respect to temperature. And right side of the graph is variation of activation energy with respect to % of decomposition.

It was observed that as the heating rate increases, the decomposition curve shifted to higher. This is clearly due to rate of heating.

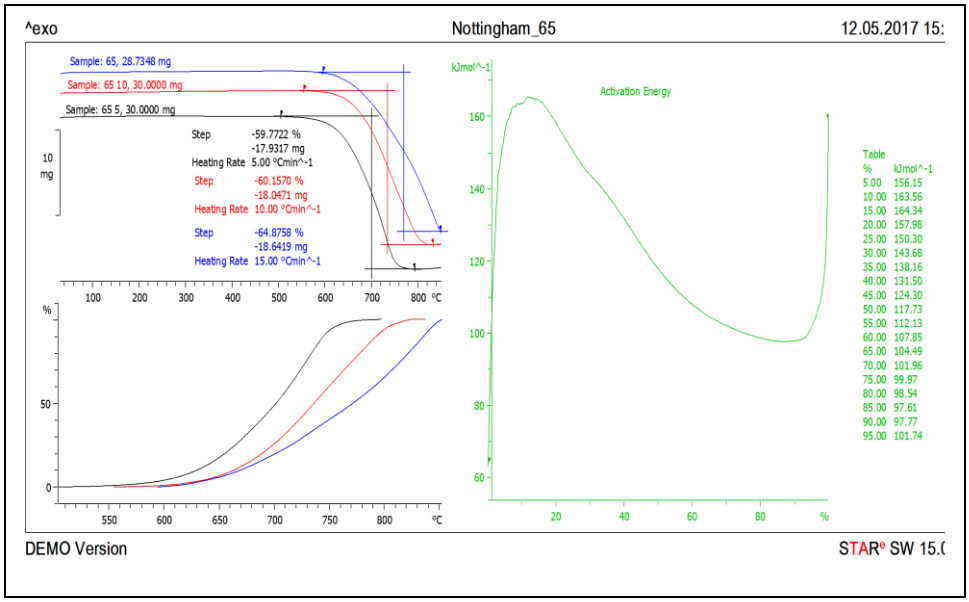

Figure 5-37: Activation energy calculation for of base salt at three different heating rates i.e., 5, 10, 15 ^{o}C.

At the top left of Figure 5-38, shows TGA analysis of base salt at three different heating rates i.e., 5, 10 and 15 ^{o}C. At the bottom left of Figure 5-38 is the decomposition of samples in percentage with respect to temperature. And right side of the graph is variation of activation energy with respect to percentage (%) of decomposition.

It was observed that as the heating rate increases, the decomposition curve shifted to higher. This is clearly due to rate of heating.

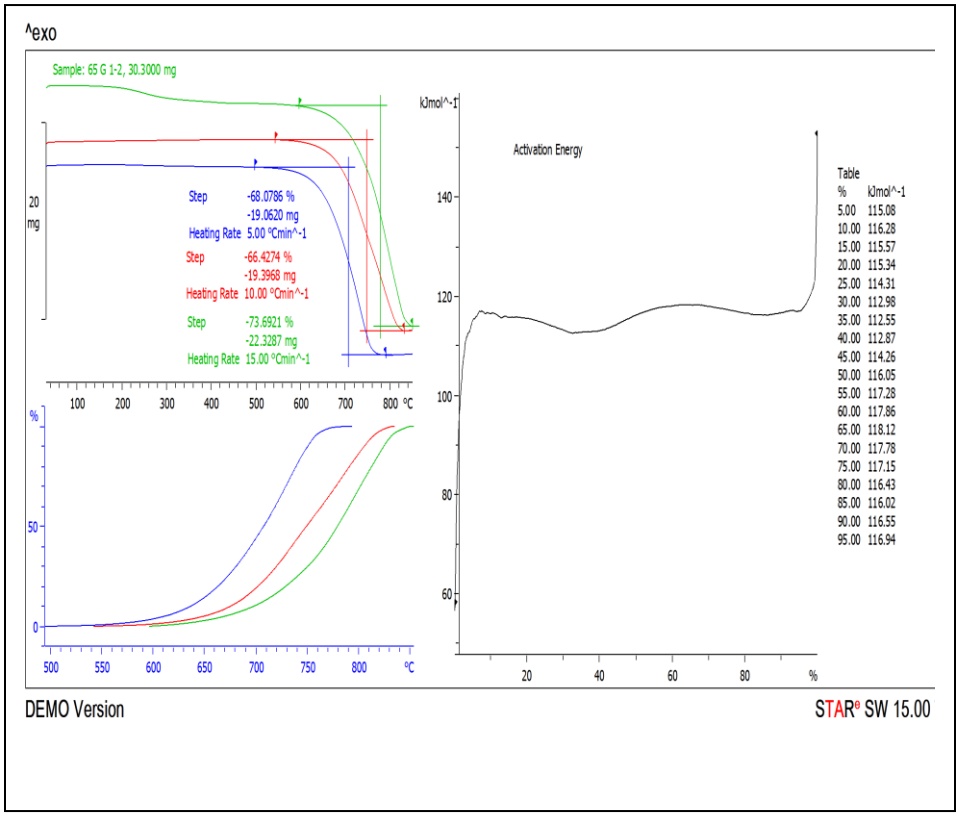

Figure 5-38: Activation energy calculation for 0.01 wt. % GE dispersed in base salt at three different heating rates i.e., 5, 10, 15 ^{o}C.

At the top left of Figure 5-39, shows TGA analysis of base salt at three different heating rates i.e., 5, 10 and 15 ^{o}C. At the bottom left of Figure 5-39 is the decomposition of samples in percentage with respect to temperature. And right side of the graph is variation of activation energy with respect to percentage (%) of decomposition.

It was observed that as the heating rate increases, the decomposition curve shifted to higher. This is clearly due to rate of heating.

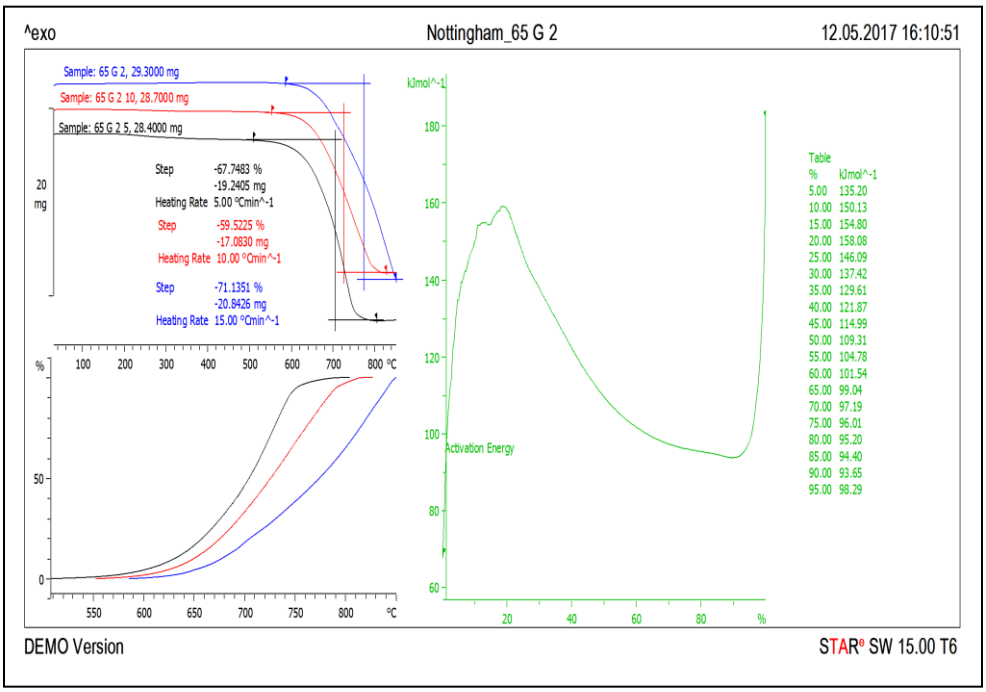

Figure 5-39: Activation energy calculation for 0.05 wt. % GE dispersed in base salt at three different heating rates i.e., 5, 10, 15 ^{o}C.

At the top left of Figure 5-40, shows TGA analysis of base salt at three different heating rates i.e., 5, 10 and 15 ^{o}C. At the bottom left of Figure 5-40 is the decomposition of samples in percentage with respect to temperature. And right side of the graph is variation of activation energy with respect to percentage (%) of decomposition.

It was observed that as the heating rate increases, the decomposition curve shifted to higher. This is clearly due to rate of heating.

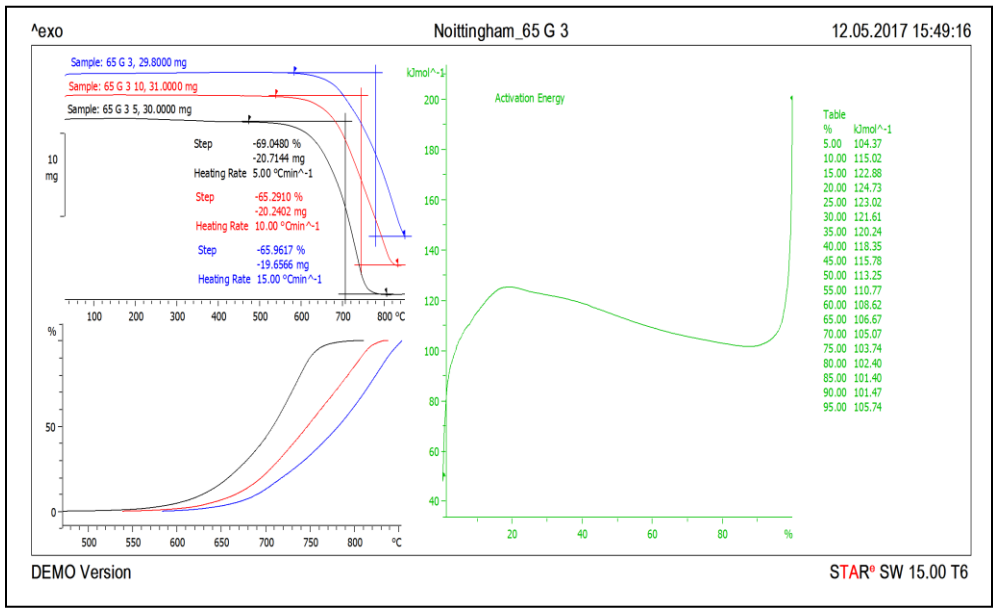

Figure 5-40: Activation energy calculation for 0.1 wt. % GE dispersed in base salt at three different heating rates i.e., 5, 10, 15 ^{o}C.

It was found that highest activation energy was obtained in base salt. Oxidation is one of the major parameter in decomposition kinetics. Addition of graphene decreases activation energy of base salt.

5.12.1 Decomposition analysis of molten salt and GE dispersed molten salt.

At high temperatures, nitrate salts gets thermally decomposed, which can be understood by three different mechanisms. They are (i) nitrate ions decompose into nitrite ion and oxygen gas, (ii) formation of alkali oxide and nitrogen oxide and (iii) evaporation of nitrate oxide [232].

First mechanism can be understood by the equation Eq. 5-2. Evaporation of oxygen is the product of decomposition.

$$NO_{3\,(l)} \overset{\Delta}{\leftrightarrow} NO_{2\,(l)} + \frac{1}{2} O_{2\,(g)} \qquad \textbf{Eq. 5-2}$$

Second mechanism can be understood in such a way that nitrate ion decomposes in to intermediate nitrite ion as given in equation.

$$NaNO_{2\,(l)} \overset{\Delta}{\leftrightarrow} Na_2O + NO2{+}NO \qquad \text{Eq. 5-3.}$$

$$NaNO_{2\,(l)} \overset{\Delta}{\leftrightarrow} Na_2O + NO_2 + NO \qquad \textbf{Eq. 5-3}$$

Third mechanism is complete decomposition of alkali nitrate ion.

Figures (Figure 5-37, Figure 5-38, Figure 5-39 and Figure 5-40) show TGA for alkali nitrate at heating rate of 5, 10 and 15 ^{o}C/min. It was observed that heating rate was an important parameter on decomposition of nitrate ions. It can be concluded that higher ramp rate gives higher decomposition temperature. Same effect was observed in all synthesized samples including GE dispersed molten salt. Thus, addition of GE in nitrate salts has not altered decomposition temperatures of nitrate salt.

CHAPTER – 6

APPLICATION

6.1 Introduction

In this chapter, fabricating and testing of a small-scale prototype of solar thermal collector for testing of synthesised molten salt and nanosuspension has been discussed. Two types of solar collectors have been fabricated i.e., (i) Flat plate thermal collector and (ii) Flat plate PV/T using SS304. Daily operating results of base salt and nanosuspension has been presented in this chapter.

6.2 Fabricating of prototype for TES application

Initially, Cu sheets of size 300mmx300mmx0.35mm and Cu tubes. While doing hot welding between Cu sheet and Cu tube. Cu sheets are deforming completely as shown in Figure 6-1. As Cu was deforming, we tried by using stainless steel of grade 304 for fabricating and it did not got deformed.

Figure 6-1: Manufacturing of solar thermal collector using Cu sheets and tubes

So, we have taken stainless steel of grade 304 as our testing material. Figure 6-2 below shows manufacturing of solar thermal collector using stainless steel. Dimensions of stainless steel sheet are equal to photo-voltaic collector, to compare both of them.

Figure 6-2: Manufacturing of solar thermal collector using stainless steel 304.

Solar thermal collector was glued behind photo-voltaic collector as shown in Figure 6-3 and Figure 6-4 is rare view of PV/thermal collector. Figure 6-5 is solar thermal collector after black coating.

Figure 6-3: Snapshot of PV/thermal and thermal collector.

Figure 6-4: Rare view of PV/thermal and thermal collector

Figure 6-5: Solar thermal collector after black coating

6.3 Daily operating

Solar heat flux was estimated using solar collector. Figure 6-6 shows temperature variation of water with respect to solar radiation. By analyzing the Figure 6-6 shows that maximum water temperature reaches at 72.5 ^{o}C. After reaching to its highest temperature, it remains constant even with decrease in solar flux. This might be due to isothermal behavior of water. It was also observed the water temperature was below 70 ^{o}C. This is due lot of fluctuations in solar heat flux. Water temperature of PV/T collector is lower than thermal collector, this is due PV collector was fixed on the top of thermal collector. However, maximum temperature obtained in PV/T collector is 66.5 ^{o}C, which is also acceptable for hot

water usage. In the meantime PV collector also gives electricity maximum up to 10 watts.

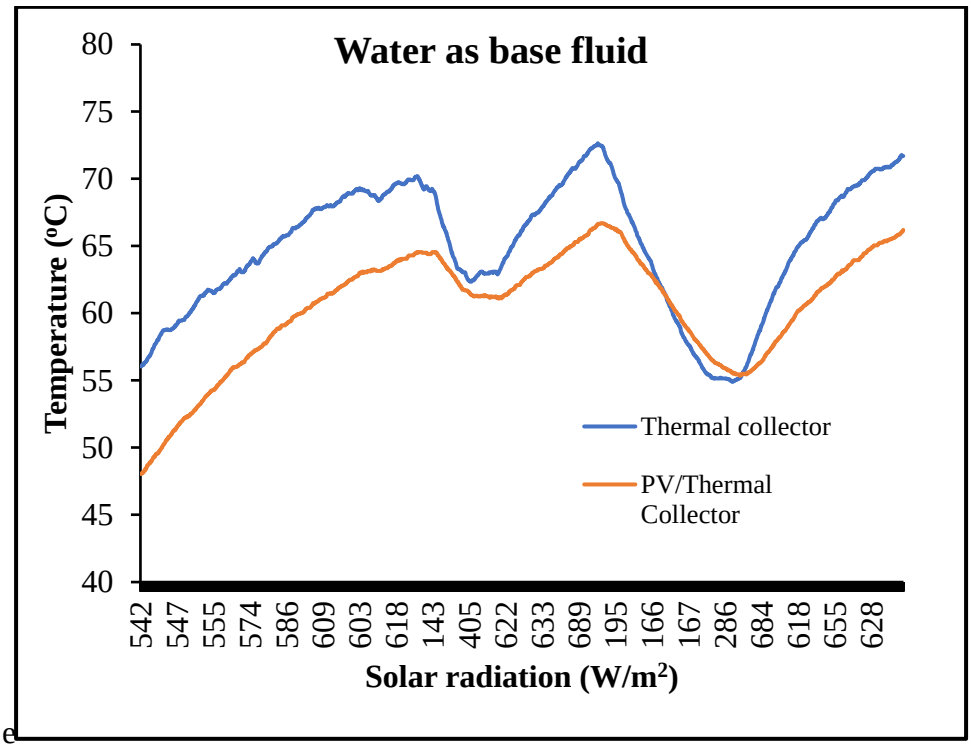

e

Figure 6-6: Variation of water temperature in thermal and PV/thermal collector

Figure 6-7 shows temperature variation of base salt in thermal and PV/thermal collector. From analysis of Figure 6-7 shows that molten salt temperature almost identical to water temperature. The highest temperature obtained in thermal collector was 72.3 ºC, where was in PV/thermal collector the highest temperature obtained was 71.75 ºC. By comparing x-axis (i.e., solar radiation) of Figure 6-6 and Figure 6-7, it was found that even with less solar radiation, temperature of base molten salt

remains constant for little bit long duration of time than water temperature. This is due to thermal stability of base salt.

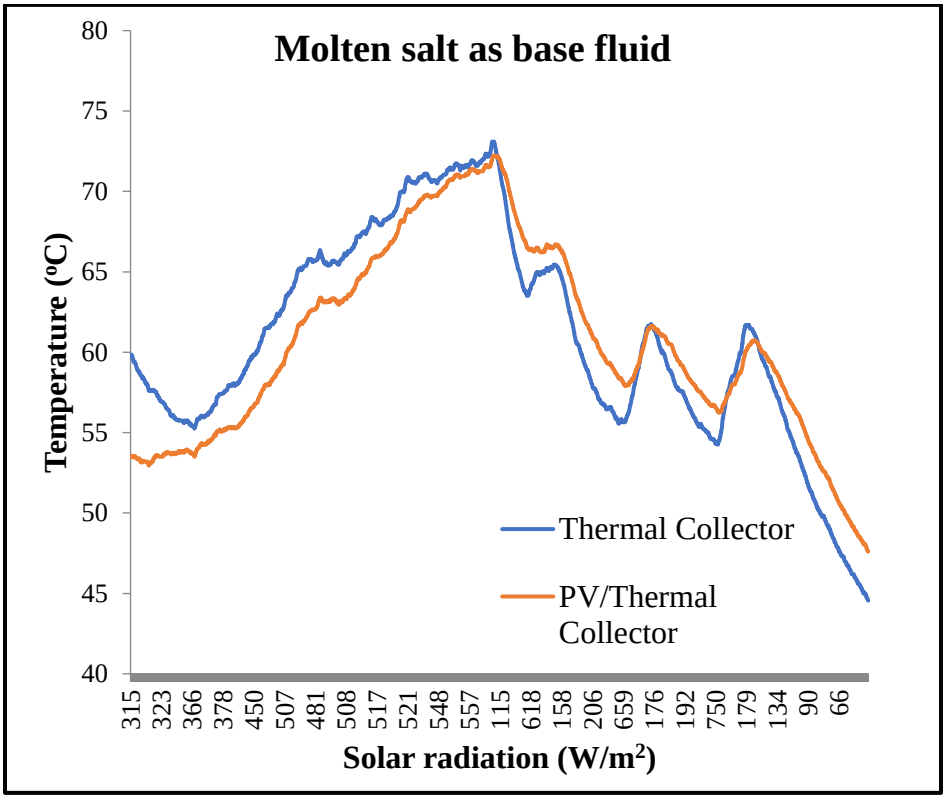

Figure 6-7: Variation of base fluid temperature in thermal and PV/Thermal collector

Figure 6-8 shows temperature variation of base salt dispersed with 0.01 wt. % GE in thermal and PV/Thermal collector. From Figure 6-8, it was found that the highest temperature obtained as 82.3 ºC for thermal collector and 85.95 ºC for PV/Thermal collector. This is due to high thermal conductivity of GE. Experiment was repeated on the next day and found almost the same results. By analysis on x-axis, it was found that even with low solar radiation (ex: 30.31 W/m^2) temperature of nanosuspension remained at 45.65 ºC. This means that heat capacity has

got increased of base salt after adding GE. Thus, it was concluded that by adding GE in base salt there is increase in TC and HC.

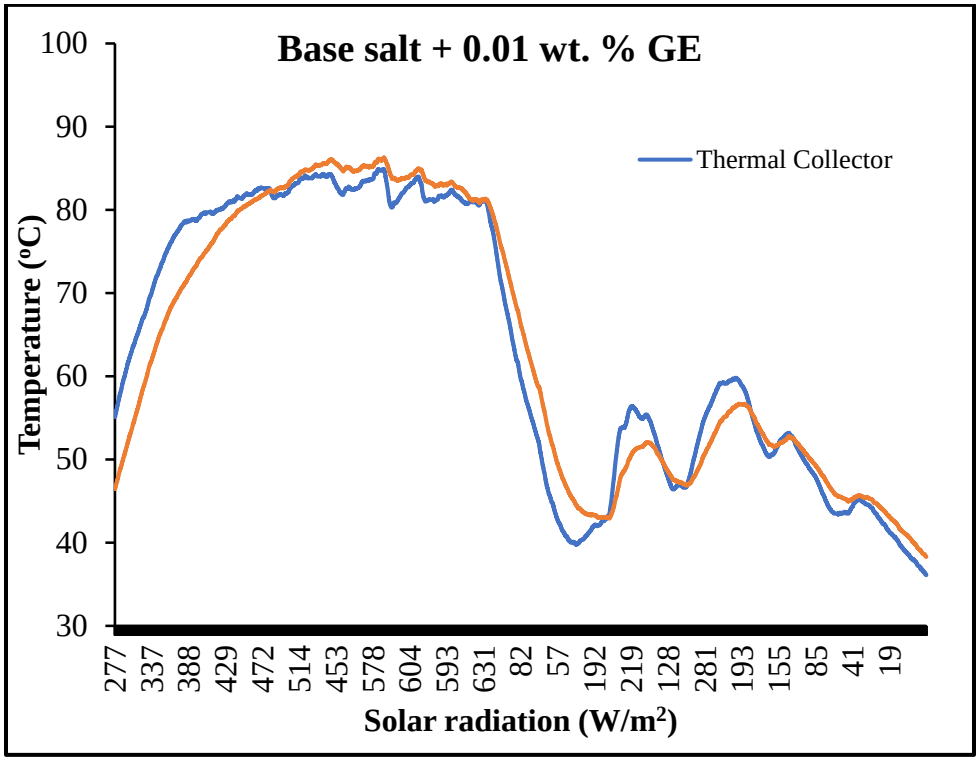

Figure 6-8: Temperature variation of base salt + 0.01 wt. % GE in thermal and PV/Thermal collector

Figure 6-9 shows temperature variation of base salt dispersed with 0.05 wt. % GE in thermal and PV/Thermal collector. The highest temperature reached was 83 °C and 72 °C for thermal collector and PV/thermal collector, respectively. In thermal collector, by dispersing 0.05 wt. % GE in base salt, it was found that TES materials temperature was higher than 0.01 wt. % GE in base salt. The result is obvious with higher concentration of GE. But in PV/thermal collector, it was obtained that lower temperature than 0.01 wt. % GE. This might be due to cluster formation of GE sheets.

From Figure 6-9, it was also observe that average temperature of thermal and PV/thermal collector was above 55 ^{o}C, this is due to increase in HC with increase in dispersion concentration.

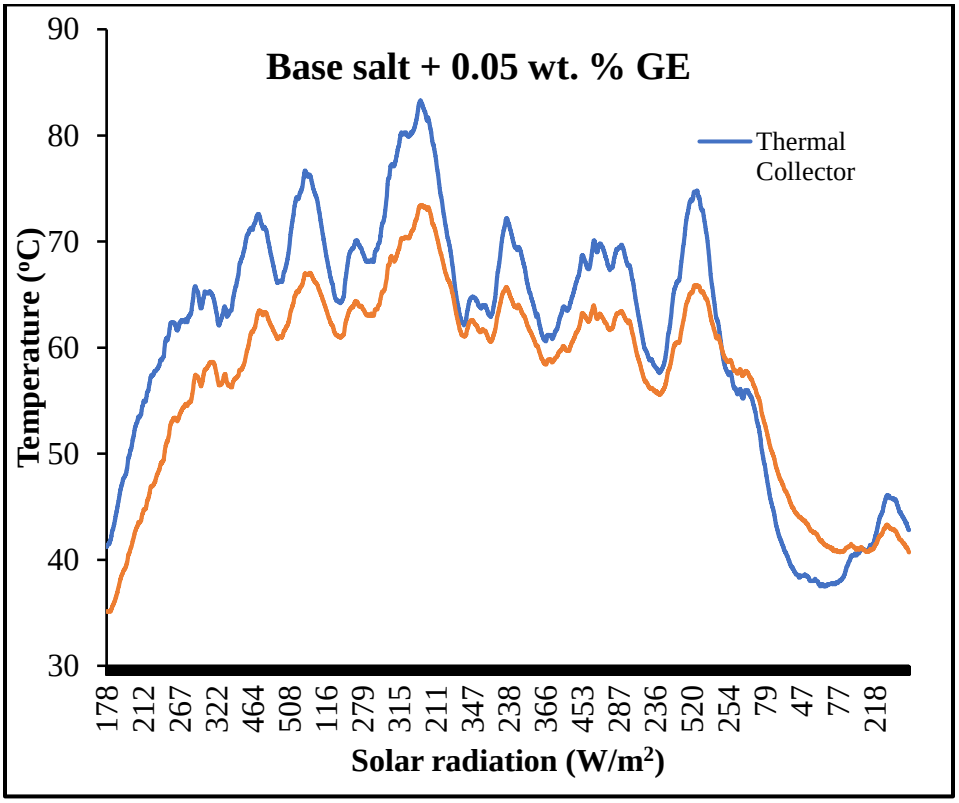

Figure 6-9: Variation of base salt + 0.05 wt. % GE in thermal and PV/Thermal Collector

Figure 6-10 shows temperature variation of base salt with dispersing 0.1 wt. % GE in thermal and PV/thermal collector. In thermal collector, the highest temperature obtained was 83.7 ^{o}C, which is the highest temperature value compared to remaining all dispersion. The result is obvious with higher concentration of GE in base salt. This is due to higher TC of GE and also from uniform dispersion of GE in base salt. The

average temperature of nanosuspension in thermal collector was above 60 ^{o}C. This is increase in HC with increase in dispersion concentration.

In PV/Thermal collector, the highest temperature of nanosuspension was obtained as 80.5 ^{o}C. This value is higher than 0.05 wt. % and lower than 0.01 wt. % nanosuspension. This might be due to formation of small clusters of GE. The average temperature of nanosuspension in PV/thermal collector was above 60 ^{o}C, which is higher than remaining all dispersion. This is due increase in HC with increase in GE concentration of nanosuspension.

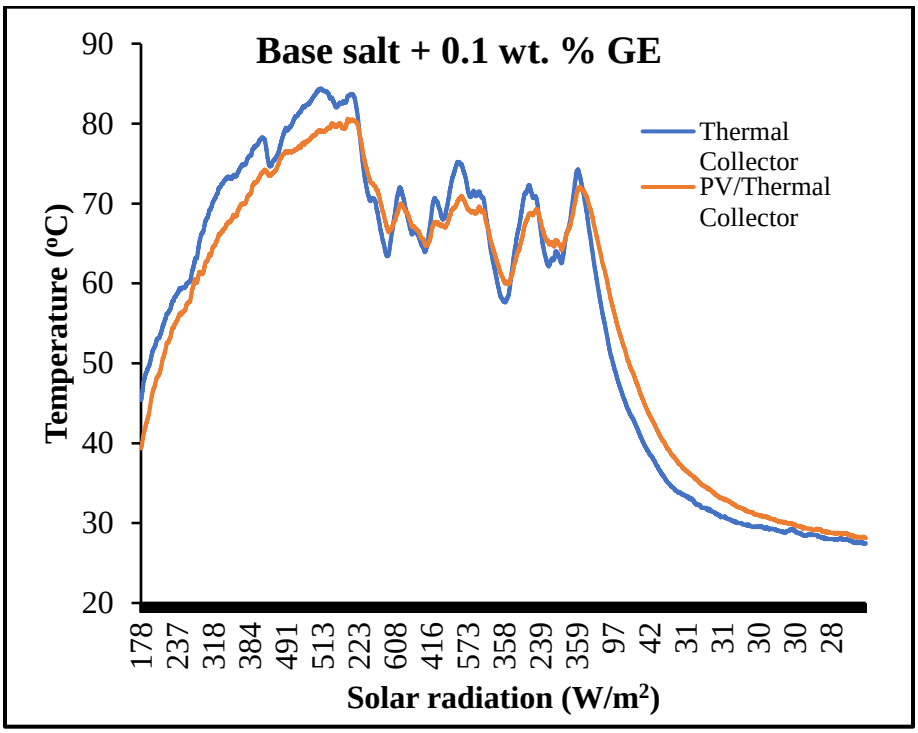

Figure 6-10: Variation of base salt + 0.1 wt. % GE in thermal and PV/Thermal collector

CHAPTER – 7

CONCLUSIONS

7.1 Introduction

A detailed description on solar thermal energy applications, mainly focusing on different TES materials has been presented. The information on TES materials is divided into three sections: liquid storage media, molten salts and paraffins. It was found that the effect of nanomaterials on TC depends on various parameters such as particle size, shape, material, volume fraction, type of fluid and temperature. Also, surfactants, additives and pH manipulation contribute significantly towards the stability of NP in base fluids and hence leading to higher TC of TES material. PCMs offer an alternative solution in TES by using a similar heat transfer infrastructure. Experimental studies showed that with the optimum amount of NP, PCMs have the potential of providing a more efficient means of storage. SHC enhancement with trace amounts of NP was observed in different TES materials. However, the results were not conclusive as the doping of nanomaterials in TES is still in its infancy stage and future work should focus taking into account: i) Effect of nanomaterial, NP size, shape, concentration of nanomaterial, types of TES and operating temperature for enhancing SHC, ii) Long term stability of nanomaterials and iii) Compatibility with construction material. The experimental and numerical studies for solar collectors showed that in some cases, the efficiency could increase remarkably by using TES doped with NP. It was suggested that the TES doped with varying volume fractions of NP should be tested to find the optimum

volume fraction. Many theories and mechanisms were proposed for enhanced thermo-physical properties of NP doped in TES. However, exact mechanisms and theories and for enhanced thermo-physical properties for NP doped in molten salt and paraffins are still in investigation. In addition, there are many challenges associated with NP such as agglomeration, time-dependent segregation, degradation, optimum concentration and cost that need to be addressed before it can be used with TES materials in large scale applications.

7.2 Principal findings

1. Investigating thermal properties of low temperature molten salt doped with three different concentrations of GE has been studied. Dispersing 0.01, 0.05 and 0.1 wt. % of GE in base molten salt led to enhanced HC by 5.065, 7.525 and 13.169%, respectively. This enhancement in HC with addition of GE may be due to reduced inter-layer spacing between molten salts molecules. Conventional theoretical model of HC was in good agreement with experimental result as the error of deviation was $< \pm 14$. Moreover, an enhancement of 1.32 and 2.31% in TC was observed with the addition of 0.05 and 0.1 wt. % GE respectively. This enhanced TC may be due to Brownian motion and percolation network of GE. Further, various theoretical TC models were used to predict the experimental TC values. Maxwell and Hamilton-Crosser models

were found to be in good agreement with experimental results. However, Nan's model did not fit the experimental results.

2. Investigation on rheological and corrosion properties of selected eutectic salt and GE dispersed eutectic salt was also performed. From rheological measurements, it was concluded that with increase in concentration of GE in base salt, there is increase in viscosity, which was due to agglomeration of GE sheets in base salt. Viscosity of base salt and nanosuspension are highly dependent on mass concentration of GE and temperature. At 70 ^{o}C, with addition of 0.01, 0.05 and 0.1 wt. % GE in eutectic salt, it was found that viscosity got enhanced by 124.95%, 208.76% and 547.96%, respectively. At 80 ^{o}C, with similar addition of GE concentration in eutectic salt, it was found that viscosity got enhanced by 62.22%, 91.38% and 424.51%, respectively. At 90 ^{o}C, with similar addition of GE concentration in eutectic salt, it was found that viscosity got declined by 9.13% and enhanced by 74.35 and 381.31%. At 200 ^{o}C, with similar addition of GE concentration in eutectic salt, it was found that viscosity got enhanced by 1.49% and declined by 6.89% and 4.66%. Nanosuspension also shows non-Newtonian behavior and was more sensitive to temperature change than concentration of GE. With increase in temperature, inter and intramolecular interactions

of base salt and nanosuspensions are weakened. This consequently results in decrease in viscosity. Einstein's viscosity model does not agree with experimental results at all temperature of measurements. However, error of deviation decreases with increase in temperature of eutectic salt. This was due to at high temperature eutectic salt approaches to Newtonian fluid.

3. For Cu, corrosion test confirms that rate of corrosion increases with increase in GE concentration in eutectic salt. This was due to temperature of nanosuspension increases with increase in GE concentration. This results in weakening of intermolecular bonds of eutectic salts. For SS304, corrosion test confirms constant rate of corrosion even with increase in GE concentration. Protective oxide layer was formed on the surface of SS304, due to corrosion. This protective layer avoids diffusion growth of oxygen in SS304.

4. FTIR results confirm that no chemical interaction occurred between GE and eutectic salt molecules. Furthermore, XRD result confirms no change in peak with addition of GE in base salt. Thus, there was no change in crystal structure of all nitrate molecules. Kinetic studies of base salt and GE dispersed base salt confirm that addition of GE has not altered decomposition of rate of molten salt.

5. By applying our characterization studies, on fabricated flat plate solar collector. It was observed that GE dispersed molten salt stores more solar thermal energy than base salt and normal water. It can be concluded that GE dispersed molten salt can be used as TES material in solar collectors.

7.3 Limitations

Due to multidisciplinary nature of studies. There are few limitations of research which are stated as below.

1. As graphene 60 nm sheets was procured, cost of graphene is one of our limitation. Morphological deformation of graphene has been assumed as negligible.
2. All experimental investigations are done using precise instrument except low and high temperature corrosion test.
3. In application part, many precautions have been taken while doing hot wielding. While doing hot wielding in industry. Many parallax errors can be reduced.
4. While taking temperature readings in application part. Thermocouples have placed in complete air tight collector tubes. Instead of just covering collector tubes, metal head cap can be used to get more accurate reading of data logger.

5. Research needs to be done for knowing measurement of density in solid state of molten salt.

7.4 Challenges

1. Uniform dispersion of graphene in molten salt is very important factor for thermal performance of nanosuspension. Studies need to be done for uniform dispersion without damaging its morphological structure.
2. Present research has been done to know important properties of nanosuspension like heat capacity, thermal conductivity, thermal stability, uniform dispersion, viscosity and corrosion behavior. Further studies can be done on knowing Reynolds, Prandtl, Nusselt numbers, latent heat capacity and high temperature application test.
3. FTIR and X-ray diffraction has been used to know presence of nitrate salt and its crystal structure. Raman spectroscopy can be used for verification of presence of nitrate molecules.
4. Computational techniques like finite element analysis need to be done before carrying out experimental analysis of application part.

References

[1] Administration USEI. <https://www.eia.gov/energyexplained/?page=us_energy_home> 2017.

[2] Weir JTaT. Renewable Energy Resources. USA and Canada2006.

[3] Kalogirou SA. Solar thermal collectors and applications. Progress in Energy and Combustion Science. 2004;30:231-95.

[4] Khartchenko NV, Kharchenko VM. Advanced Energy Systems. second ed: Taylor & Francis Group; 2014.

[5] Phelan P, Otanicar T, Taylor R, Tyagi H. Trends and Opportunities in Direct-Absorption Solar Thermal Collectors. Journal of Thermal Science and Engineering Applications. 2013;5:021003-.

[6] Renewable Energy Policy Network for the 21st Century. Global Status Report:http://www.ren21.net/wp-content/uploads/2016/10/REN21 GSR2016_FullReporten11.pdf.

[7] Hossain MS, Saidur R, Fayaz H, Rahim NA, Islam MR, Ahamed JU, et al. Review on solar water heater collector and thermal energy performance of circulating pipe. Renewable and Sustainable Energy Reviews. 2011;15:3801-12.

[8] Shukla R, Sumathy K, Erickson P, Gong J. Recent advances in the solar water heating systems: A review. Renewable and Sustainable Energy Reviews. 2013;19:173-90.

[9] Fernández A, Dieste JA. Low and medium temperature solar thermal collector based in innovative materials and improved heat exchange performance. Energy Conversion and Management. 2013;75:118-29.

[10] Paul TC, Morshed AM, Khan JA. Nanoparticle Enhanced Ionic Liquids (NEILS) as Working Fluid for the Next Generation Solar Collector. Procedia Engineering. 2013;56:631-6.

[11] Meng Z, Han D, Wu D, Zhu H, Li Q. Thermal Conductivities, Rheological Behaviors and Photothermal Properties of Ethylene Glycol-based Nanofluids Containing Carbon Black Nanoparticles. Procedia Engineering. 2012;36:521-7.

[12] Nieto de Castro CA, Lourenço MJV, Ribeiro APC, Langa E, Vieira SIC, Goodrich P, et al. Thermal Properties of Ionic Liquids and IoNanofluids of Imidazolium and Pyrrolidinium Liquids†. Journal of Chemical & Engineering Data. 2009;55:653-61.

[13] Choi SUS. Nanofluids: From Vision to Reality Through Research. Journal of Heat Transfer. 2009;131:033106-.

[14] Mahian O, Kianifar A, Kalogirou SA, Pop I, Wongwises S. A review of the applications of nanofluids in solar energy. International Journal of Heat and Mass Transfer. 2013;57:582-94.

[15] Fan L-W, Fang X, Wang X, Zeng Y, Xiao Y-Q, Yu Z-T, et al. Effects of various carbon nanofillers on the thermal conductivity and energy storage properties of paraffin-based nanocomposite phase change materials. Applied Energy. 2013;110:163-72.

[16] Colangelo G, Favale E, Miglietta P, de Risi A. Innovation in flat solar thermal collectors: A review of the last ten years experimental results. Renewable and Sustainable Energy Reviews. 2016;57:1141-59.

[17] Alghoul MA, Sulaiman MY, Azmi BZ, Wahab MA. Review of materials for solar thermal collectors. Anti-Corrosion Methods and Materials. 2005;52:199-206.

[18] Winston R. Principles of solar concentrators of a novel design. Solar Energy. 1974;16:89-95.

[19] Kaiyan H, Hongfei Z, Tao T. A novel multiple curved surfaces compound concentrator. Solar Energy. 2011;85:523-9.

[20] Guiqiang L, Gang P, Yuehong S, Yunyun W, Jie J. Design and investigation of a novel lens-walled compound parabolic concentrator with air gap. Applied Energy. 2014;125:21-7.

[21] Zhang HL, Baeyens J, Degrève J, Cacères G. Concentrated solar power plants: Review and design methodology. Renewable and Sustainable Energy Reviews. 2013;22:466-81.

[22] Behar O, Khellaf A, Mohammedi K. A review of studies on central receiver solar thermal power plants. Renewable and Sustainable Energy Reviews. 2013;23:12-39.

[23] Cheng ZD, He YL, Cui FQ, Xu RJ, Tao YB. Numerical simulation of a parabolic trough solar collector with nonuniform solar flux conditions by coupling FVM and MCRT method. Solar Energy. 2012;86:1770-84.

[24] NREL. SolTrace optical modelling software. SolTrace 2012.

[25] Pavlovic S, #x161, R. a, Stefanovic VP. Ray Tracing Study of Optical Characteristics of the Solar Image in the Receiver for a Thermal Solar Parabolic Dish Collector. Journal of Solar Energy. 2015;2015:10.

[26] Andasol-1. <http://www.nrel.gov/csp/solarpaces/project_detail.cfm/projectID=3>. 2013 [accessed 23.07.14].

[27] Arenales. <http://www.nrel.gov/csp/solarpaces/project_detail.cfm/projectID=241>. 2013 [accessed 23.07.14].

[28] Barlev D, Vidu R, Stroeve P. Innovation in concentrated solar power. Solar Energy Materials and Solar Cells. 2011;95:2703-25.

[29] Dincer I, Rosen MA. Thermal Energy Storage: Systems and Applications, 2nd Edition. 2010.

[30] Wang Z, Yang W, Qiu F, Zhang X, Zhao X. Solar water heating: From theory, application, marketing and research. Renewable and Sustainable Energy Reviews. 2015;41:68-84.

[31] Çomaklı K, Çakır U, Kaya M, Bakirci K. The relation of collector and storage tank size in solar heating systems. Energy Conversion and Management. 2012;63:112-7.

[32] Badescu V. Simulation analysis for the active solar heating system of a passive house. Applied Thermal Engineering. 2005;25:2754-63.

[33] Li Z, Chen C, Luo H, Zhang Y, Xue Y. All-glass vacuum tube collector heat transfer model used in forced-circulation solar water heating system. Solar Energy. 2010;84:1413-21.

[34] Walker A, Mahjouri F, Stiteler R. Evacuated-Tube Heat-Pipe Solar Collectors Applied to the Recirculation Loop in a Federal Building: Preprint: ; National Renewable Energy Lab., Golden, CO (US); 2004.

[35] Chu; J, Cruickshank CA. Solar-Assisted Heat Pump Systems: A Review of Existing Studies and Their Applicability to the Canadian Residential Sector. Journal of Solar Energy Engineering. 2014;136.

[36] Hepbasli A, Kalinci Y. A review of heat pump water heating systems. Renewable and Sustainable Energy Reviews. 2009;13:1211-29.

[37] Omojaro P, Breitkopf C. Direct expansion solar assisted heat pumps: A review of applications and recent research. Renewable and Sustainable Energy Reviews. 2013;22:33-45.

[38] Li YW, Wang RZ, Wu JY, Xu YX. Experimental performance analysis on a direct-expansion solar-assisted heat pump water heater. Applied Thermal Engineering. 2007;27:2858-68.

[39] Chaturvedi SK, Chen DT, Kheireddine A. Thermal performance of a variable capacity direct expansion solar-assisted heat pump. Energy Conversion and Management. 1998;39:181-91.

[40] Chyng JP, Lee CP, Huang BJ. Performance analysis of a solar-assisted heat pump water heater. Solar Energy. 2003;74:33-44.

[41] Amin ZM, Hawlader MNA. A review on solar assisted heat pump systems in Singapore. Renewable and Sustainable Energy Reviews. 2013;26:286-93.

[42] Hawlader MNA, Chou SK, Jahangeer KA, Rahman SMA, Lau K. W E. Solar-assisted heat-pump dryer and water heater. Applied Energy. 2003;74:185-93.

[43] Kuang YH, Sumathy K, Wang RZ. Study on a direct-expansion solar-assisted heat pump water heating system. International Journal of Energy Research. 2003;27:531-48.

[44] Molinaroli L, Joppolo CM, De Antonellis S. Numerical Analysis of the Use of R-407C in Direct Expansion Solar Assisted Heat Pump. Energy Procedia. 2014;48:938-45.

[45] Gorozabel Chata FB, Chaturvedi SK, Almogbel A. Analysis of a direct expansion solar assisted heat pump using different refrigerants. Energy Conversion and Management. 2005;46:2614-24.

[46] Moreno-Rodriguez A, Garcia-Hernando N, González-Gil A, Izquierdo M. Experimental validation of a theoretical model for a direct-expansion solar-assisted heat pump applied to heating. Energy. 2013;60:242-53.

[47] Lee DW, Sharma A. Thermal performances of the active and passive water heating systems based on annual operation. Solar Energy. 2007;81:207-15.

[48] Singh R, Lazarus IJ, Souliotis M. Recent developments in integrated collector storage (ICS) solar water heaters: A review. Renewable and Sustainable Energy Reviews. 2016;54:270-98.

[49] Gertzos KP, Caouris YG. Experimental and computational study of the developed flow field in a flat plate integrated collector storage (ICS) solar device with recirculation. Experimental Thermal and Fluid Science. 2007;31:1133-45.

[50] Souliotis M, Quinlan P, Smyth M, Tripanagnostopoulos Y, Zacharopoulos A, Ramirez M, et al. Heat retaining integrated collector storage solar water heater with asymmetric CPC reflector. Solar Energy. 2011;85:2474-87.

[51] Mohamad AA. Integrated solar collector–storage tank system with thermal diode. Solar Energy. 1997;61:211-8.

[52] Goetzberger A, Rommel M. Prospects for integrated storage collector systems in central Europe. Solar Energy. 1987;39:211-9.

[53] Schmidt C, Goetzberger A. Single-tube integrated collector storage systems with transparent insulation and involute reflector. Solar Energy. 1990;45:93-100.

[54] Kalogirou S. Design, construction, performance evaluation and economic analysis of an integrated collector storage system. Renewable Energy. 1997;12:179-92.

[55] Smyth M, Eames PC, Norton B. A comparative performance rating for an integrated solar collector/storage vessel with inner sleeves to increase heat retention. Solar Energy. 1999;66:291-303.

[56] Helal O, Chaouachi B, Gabsi S. Design and thermal performance of an ICS solar water heater based on three parabolic sections. Solar Energy. 2011;85:2421-32.

[57] Canbazoğlu S, Şahinaslan A, Ekmekyapar A, Aksoy ÝG, Akarsu F. Enhancement of solar thermal energy storage performance using sodium thiosulfate pentahydrate of a conventional solar water-heating system. Energy and Buildings. 2005;37:235-42.

[58] Reddy KS. Thermal Modeling of PCM-Based Solar Integrated Collector Storage Water Heating System. Journal of Solar Energy Engineering. 2007;129:458-64.

[59] Chaabane M, Mhiri H, Bournot P. Thermal performance of an integrated collector storage solar water heater (ICSSWH) with phase change materials (PCM). Energy Conversion and Management. 2014;78:897-903.

[60] Mertol A, Greif R. Review of Thermosyphon Solar Water Heaters. In: Yüncü H, Paykoc E, Yener Y, editors. Solar Energy Utilization: Springer Netherlands; 1987. p. 537-69.

[61] Chuawittayawuth K, Kumar S. Experimental investigation of temperature and flow distribution in a thermosyphon solar water heating system. Renewable Energy. 2002;26:431-48.

[62] Huang J, Pu S, Gao W, Que Y. Experimental investigation on thermal performance of thermosyphon flat-plate solar water heater with a mantle heat exchanger. Energy. 2010;35:3563-8.

[63] Esen M, Esen H. Experimental investigation of a two-phase closed thermosyphon solar water heater. Solar Energy. 2005;79:459-68.

[64] Yamaguchi H, Sawada N, Suzuki H, Ueda H, Zhang XR. Preliminary Study on a Solar Water Heater Using Supercritical Carbon Dioxide as Working Fluid. Journal of Solar Energy Engineering. 2010;132:011010-.

[65] Chien CC, Kung CK, Chang CC, Lee WS, Jwo CS, Chen SL. Theoretical and experimental investigations of a two-phase thermosyphon solar water heater. Energy. 2011;36:415-23.

[66] Budihardjo I, Morrison GL. Performance of water-in-glass evacuated tube solar water heaters. Solar Energy. 2009;83:49-56.

[67] Chen B-R, Chang Y-W, Lee W-S, Chen S-L. Long-term thermal performance of a two-phase thermosyphon solar water heater. Solar Energy. 2009;83:1048-55.

[68] Arab M, Soltanieh M, Shafii MB. Experimental investigation of extra-long pulsating heat pipe application in solar water heaters. Experimental Thermal and Fluid Science. 2012;42:6-15.

[69] Redpath DAG, Eames PC, Lo SNG, Griffiths PW. Experimental investigation of natural convection heat exchange within a physical model of the manifold chamber of a thermosyphon heat-pipe evacuated tube solar water heater. Solar Energy. 2009;83:988-97.

[70] Redpath DAG. Thermosyphon heat-pipe evacuated tube solar water heaters for northern maritime climates. Solar Energy. 2012;86:705-15.

[71] Raisul Islam M, Sumathy K, Ullah Khan S. Solar water heating systems and their market trends. Renewable and Sustainable Energy Reviews. 2013;17:1-25.

[72] Chong KK, Chay KG, Chin KH. Study of a solar water heater using stationary V-trough collector. Renewable Energy. 2012;39:207-15.

[73] Hepbasli A. Exergetic modeling and assessment of solar assisted domestic hot water tank integrated ground-source heat pump systems for residences. Energy and Buildings. 2007;39:1211-7.

[74] Tripanagnostopoulos Y, Souliotis M. ICS solar systems with horizontal (E–W) and vertical (N–S) cylindrical water storage tank. Renewable Energy. 2004;29:73-96.

[75] Tripanagnostopoulos Y, Souliotis M, Nousia T. CPC type integrated collector storage systems. Solar Energy. 2002;72:327-50.

[76] Ng KC, Yap C, Khor TH. Outdoor testing of evacuated-tube heat-pipe solar collectors. Proceedings of the Institution of Mechanical Engineers, Part E: Journal of Process Mechanical Engineering. 2000;214:23-30.

[77] Plante RH. Chapter four - Solar Domestic Hot Water Systems. In: Plante RH, editor. Solar Energy, Photovoltaics, and Domestic Hot Water. Boston: Academic Press; 2014. p. 41-73.

[78] Cruz-Peragon F, Palomar JM, Casanova PJ, Dorado MP, Manzano-Agugliaro F. Characterization of solar flat plate collectors. Renewable and Sustainable Energy Reviews. 2012;16:1709-20.

[79] Chen Z, Furbo S, Perers B, Fan J, Andersen E. Efficiencies of Flat Plate Solar Collectors at Different Flow Rates. Energy Procedia. 2012;30:65-72.

[80] García A, Martin RH, Pérez-García J. Experimental study of heat transfer enhancement in a flat-plate solar water collector with wire-coil inserts. Applied Thermal Engineering. 2013;61:461-8.

[81] Fan J, Furbo S. Buoyancy Effects on Thermal Behavior of a Flat-Plate Solar Collector. Journal of Solar Energy Engineering. 2008;130:021010-.

[82] Del Col D, Padovan A, Bortolato M, Dai Prè M, Zambolin E. Thermal performance of flat plate solar collectors with sheet-and-tube and roll-bond absorbers. Energy. 2013;58:258-69.

[83] Giovannetti F, Föste S, Ehrmann N, Rockendorf G. High transmittance, low emissivity glass covers for flat plate collectors: Applications and performance. Solar Energy. 2014;104:52-9.

[84] Sakhrieh A, Al-Ghandoor A. Experimental investigation of the performance of five types of solar collectors. Energy Conversion and Management. 2013;65:715-20.

[85] Zambolin E, Del Col D. An improved procedure for the experimental characterization of optical efficiency in evacuated tube solar collectors. Renewable Energy. 2012;43:37-46.

[86] Liang R, Ma L, Zhang J, Zhao D. Theoretical and experimental investigation of the filled-type evacuated tube solar collector with U tube. Solar Energy. 2011;85:1735-44.

[87] Tang R, Yang Y, Gao W. Comparative studies on thermal performance of water-in-glass evacuated tube solar water heaters with different collector tilt-angles. Solar Energy. 2011;85:1381-9.

[88] Morrison GL, Tran NH, McKenzie DR, Onley IC, Harding GL, Collins RE. Long term performance of evacuated tubular solar water heaters in Sydney, Australia. Solar Energy. 1984;32:785-91.

[89] Li X, Dai YJ, Li Y, Wang RZ. Comparative study on two novel intermediate temperature CPC solar collectors with the U-shape evacuated tubular absorber. Solar Energy. 2013;93:220-34.

[90] Gudekar AS, Jadhav AS, Panse SV, Joshi JB, Pandit AB. Cost effective design of compound parabolic collector for steam generation. Solar Energy. 2013;90:43-50.

[91] Rabl A. Optical and thermal properties of compound parabolic concentrators. Solar Energy. 1976;18:497-511.

[92] Jadhav AS, Gudekar AS, Patil RG, Kale DM, Panse SV, Joshi JB. Performance analysis of a novel and cost effective CPC system. Energy Conversion and Management. 2013;66:56-65.

[93] Klaus-Jürgen Riffelmann DGaPN. Ultimate Trough: The New Parabolic Trough Collector Generation for Large Scale Solar Thermal Power Plants. 5th International Conference on Energy Sustainability. USA: ASME; 2011.

[94] Amelio M, Ferraro V, Marinelli V, Summaria A. An evaluation of the performance of an integrated solar combined cycle plant provided with air-linear parabolic collectors. Energy. 2014;69:742-8.

[95] Xiao X, Zhang P, Shao DD, Li M. Experimental and numerical heat transfer analysis of a V-cavity absorber for linear parabolic trough solar collector. Energy Conversion and Management. 2014;86:49-59.

[96] Cau G, Cocco D. Comparison of Medium-size Concentrating Solar Power Plants based on Parabolic Trough and Linear Fresnel Collectors. Energy Procedia. 2014;45:101-10.

[97] Giostri A, Binotti M, Silva P, Macchi E, Manzolini G. Comparison of Two Linear Collectors in Solar Thermal Plants: Parabolic Trough Versus Fresnel. Journal of Solar Energy Engineering. 2012;135:011001-.

[98] Hachicha AA, Rodríguez I, Lehmkuhl O, Oliva A. On the CFD&HT of the Flow around a Parabolic Trough Solar Collector under Real Working Conditions. Energy Procedia. 2014;49:1379-90.

[99] Lüpfert E, Pottler K, Ulmer S, Riffelmann K-J, Neumann A, Schiricke B. Parabolic Trough Optical Performance Analysis Techniques. Journal of Solar Energy Engineering. 2006;129:147-52.

[100] Pacheco JE, Gilbert, R.,. Overview of recent results for the solar two test and evaluations program. Renewable and Advanced Energy Systems for the 21st Century: Proceedings of the ASME International Solar Energy Conference 1999; 1999.

[101] Blackmon JB. Parametric determination of heliostat minimum cost per unit area. Solar Energy. 2013;97:342-9.

[102] Coelho B, Varga S, Oliveira A, Mendes A. Optimization of an atmospheric air volumetric central receiver system: Impact of solar multiple, storage capacity and control strategy. Renewable Energy. 2014;63:392-401.

[103] Boerema N, Morrison G, Taylor R, Rosengarten G. Liquid sodium versus Hitec as a heat transfer fluid in solar thermal central receiver systems. Solar Energy. 2012;86:2293-305.

[104] Pitz-Paal R, Morhenne J, Fiebig M. A new concept of a selective solar receiver for high temperature applications. Solar Energy Materials. 1991;24:293-306.

[105] Boerema N, Morrison G, Taylor R, Rosengarten G. High temperature solar thermal central-receiver billboard design. Solar Energy. 2013;97:356-68.

[106] Wei X, Lu Z, Wang Z, Yu W, Zhang H, Yao Z. A new method for the design of the heliostat field layout for solar tower power plant. Renewable Energy. 2010;35:1970-5.

[107] Collado FJ, Guallar J. Two-stages optimised design of the collector field of solar power tower plants. Solar Energy. 2016;135:884-96.

[108] Abu-Hamdeh NH, Alnefaie KA. Design considerations and construction of an experimental prototype of concentrating solar power tower system in Saudi Arabia. Energy Conversion and Management. 2016;117:63-73.

[109] Liao Z, Faghri A. Thermal analysis of a heat pipe solar central receiver for concentrated solar power tower. Applied Thermal Engineering. 2016;102:952-60.

[110] Almsater S, Saman W, Bruno F. Performance enhancement of high temperature latent heat thermal storage systems using heat pipes with and without fins for concentrating solar thermal power plants. Renewable Energy. 2016;89:36-50.

[111] Garcia P, Ferriere A, Bezian J-J. Codes for solar flux calculation dedicated to central receiver system applications: A comparative review. Solar Energy. 2008;82:189-97.

[112] Ho CK, Iverson BD. Review of high-temperature central receiver designs for concentrating solar power. Renewable and Sustainable Energy Reviews. 2014;29:835-46.

[113] Berenguel M, Rubio FR, Valverde A, Lara PJ, Arahal MR, Camacho EF, et al. An artificial vision-based control system for automatic heliostat positioning offset correction in a central receiver solar power plant. Solar Energy. 2004;76:563-75.

[114] Hou Y, Vidu R, Stroeve P. Solar Energy Storage Methods. Industrial & Engineering Chemistry Research. 2011;50:8954-64.

[115] Kuravi S, Trahan J, Goswami DY, Rahman MM, Stefanakos EK. Thermal energy storage technologies and systems for concentrating solar power plants. Progress in Energy and Combustion Science. 2013;39:285-319.

[116] Cabeza LF. Advances in Thermal Energy Storage Systems: Woodhead Publishing; 2014.

[117] Zalba B, Marín JM, Cabeza LF, Mehling H. Review on thermal energy storage with phase change: materials, heat transfer analysis and applications. Applied Thermal Engineering. 2003;23:251-83.

[118] Gil A, Medrano M, Martorell I, Lázaro A, Dolado P, Zalba B, et al. State of the art on high temperature thermal energy storage for power generation. Part 1—Concepts, materials and modellization. Renewable and Sustainable Energy Reviews. 2010;14:31-55.

[119] Hasnain SM. Review on sustainable thermal energy storage technologies, Part I: heat storage materials and techniques. Energy Conversion and Management. 1998;39:1127-38.

[120] Nahar NM. Capital cost and economic viability of thermosyphonic solar water heaters manufactured from alternate materials in India. Renewable Energy. 2002;26:623-35.

[121] Garg HP, Mullick SC, Bhargava AK. Solar Thermal Energy Storage: Springer Netherlands; 1985.

[122] Masuda H, Ebata A, Teramae K, Hishinuma N. Alteration of Thermal Conductivity and Viscosity of Liquid by Dispersing Ultra-Fine Particles

Dispersion of Al₂O₃, SiO₂ and TiO₂ Ultra-Fine Particles. Netsu Bussei. 1993;7:227-33.

[123] Badran AA, Jubran BA. Fuel oil heating by a trickle solar collector. Energy Conversion and Management. 2001;42:1637-45.

[124] Marchã J, Osório T, Pereira MC, Horta P. Development and Test Results of a Calorimetric Technique for Solar Thermal Testing Loops, Enabling Mass Flow and Cp Measurements Independent from Fluid Properties of the HTF Used. Energy Procedia. 2014;49:2125-34.

[125] Choi SUS. Enhancing Thermal Conductivity of Fluids with Nanoparticles. In: D A Siginer and H P Wang, Eds Developments and Applications of Non-Newtonian Flows ASME. 1995;Vol. 66,:pp. 99-105.

[126] Philip J, Shima PD. Thermal properties of nanofluids. Advances in Colloid and Interface Science. 2012;183–184:30-45.

[127] Rashmi W, Khalid M, Ong SS, Saidur R. Preparation, thermo-physical properties and heat transfer enhancement of nanofluids. Materials Research Express. 2014;1:032001.

[128] Hamilton RL, Crosser OK. Thermal Conductivity of Heterogeneous Two-Component Systems. Industrial & Engineering Chemistry Fundamentals. 1962;1:187-91.

[129] Jeffrey DJ. Conduction Through a Random Suspension of Spheres. Proceedings of the Royal Society of London A Mathematical and Physical Sciences. 1973;335:355-67.

[130] Yu W, Choi SUS. The Role of Interfacial Layers in the Enhanced Thermal Conductivity of Nanofluids: A Renovated Maxwell Model. Journal of Nanoparticle Research. 2003;5:167-71.

[131] Wang B-X, Zhou L-P, Peng X-F. A fractal model for predicting the effective thermal conductivity of liquid with suspension of nanoparticles. International Journal of Heat and Mass Transfer. 2003;46:2665-72.

[132] Xue Q-Z. Model for effective thermal conductivity of nanofluids. Physics Letters A. 2003;307:313-7.

[133] Nan CW, Shi Z, Lin Y. A simple model for thermal conductivity of carbon nanotube-based composites. Chemical Physics Letters. 2003;375:666-9.

[134] Xue Q, Xu W-M. A model of thermal conductivity of nanofluids with interfacial shells. Materials Chemistry and Physics. 2005;90:298-301.

[135] Chon CH, Kihm KD, Lee SP, Choi SUS. Empirical correlation finding the role of temperature and particle size for nanofluid (Al2O3) thermal conductivity enhancement. Applied Physics Letters. 2005;87:-.

[136] Prasher R, Bhattacharya P, Phelan PE. Thermal Conductivity of Nanoscale Colloidal Solutions (Nanofluids). Physical Review Letters. 2005;94:025901.

[137] Das SK, Putra N, Thiesen P, Roetzel W. Temperature Dependence of Thermal Conductivity Enhancement for Nanofluids. Journal of Heat Transfer. 2003;125:567-74.

[138] Wang F, Han L, Zhang Z, Fang X, Shi J, Ma W. Surfactant-free ionic liquid-based nanofluids with remarkable thermal conductivity enhancement at very low loading of graphene. Nanoscale research letters. 2012;7:1-7.

[139] Batmunkh M, Tanshen MR, Nine MJ, Myekhlai M, Choi H, Chung H, et al. Thermal Conductivity of TiO2 Nanoparticles Based Aqueous Nanofluids with an Addition of a Modified Silver Particle. Industrial & Engineering Chemistry Research. 2014;53:8445-51.

[140] Yousefi T, Veysi F, Shojaeizadeh E, Zinadini S. An experimental investigation on the effect of Al2O3–H2O nanofluid on the efficiency of flat-plate solar collectors. Renewable Energy. 2012;39:293-8.

[141] Yousefi T, Veisy F, Shojaeizadeh E, Zinadini S. An experimental investigation on the effect of MWCNT-H2O nanofluid on the efficiency of flat-plate solar collectors. Experimental Thermal and Fluid Science. 2012;39:207-12.

[142] Yousefi T, Shojaeizadeh E, Veysi F, Zinadini S. An experimental investigation on the effect of pH variation of MWCNT–H2O nanofluid on the efficiency of a flat-plate solar collector. Solar Energy. 2012;86:771-9.

[143] Khullar V, Tyagi H, Phelan PE, Otanicar TP, Singh H, Taylor RA. Solar Energy Harvesting Using Nanofluids-Based Concentrating Solar

Collector. Journal of Nanotechnology in Engineering and Medicine. 2013;3:031003-.

[144] Otanicar TP, Phelan PE, Prasher RS, Rosengarten G, Taylor RA. Nanofluid-based direct absorption solar collector. Journal of Renewable and Sustainable Energy. 2010;2:-.

[145] Sani E, Mercatelli L, Barison S, Pagura C, Agresti F, Colla L, et al. Potential of carbon nanohorn-based suspensions for solar thermal collectors. Solar Energy Materials and Solar Cells. 2011;95:2994-3000.

[146] Ahmed SF, Khalid M, Rashmi W, Chan A, Shahbaz K. Recent progress in solar thermal energy storage using nanomaterials. Renewable and Sustainable Energy Reviews. 2017;67:450-60.

[147] Eastman JA, Choi US, Li S, Thompson LJ, Lee S. Enhanced Thermal Conductivity through the Development of Nanofluids. MRS Online Proceedings Library. 1996;457:null-null.

[148] Colangelo G, Favale E, de Risi A, Laforgia D. A new solution for reduced sedimentation flat panel solar thermal collector using nanofluids. Applied Energy. 2013;111:80-93.

[149] Sani E, Barison S, Pagura C, Mercatelli L, Sansoni P, Fontani D, et al. Carbon nanohorns-based nanofluids as direct sunlight absorbers. Opt Express. 2010;18:5179-87.

[150] Meng Z, Wu D, Wang L, Zhu H, Li Q. Carbon nanotube glycol nanofluids: Photo-thermal properties, thermal conductivities and rheological behavior. Particuology. 2012;10:614-8.

[151] Nieto de Castro CA, Murshed SMS, Lourenço MJV, Santos FJV, Lopes MLM, França JMP. Enhanced thermal conductivity and specific heat capacity of carbon nanotubes ionanofluids. International Journal of Thermal Sciences. 2012;62:34-9.

[152] Kumaresan V, Velraj R. Experimental investigation of the thermo-physical properties of water–ethylene glycol mixture based CNT nanofluids. Thermochimica Acta. 2012;545:180-6.

[153] He Q, Wang S, Tong M, Liu Y. Experimental study on thermophysical properties of nanofluids as phase-change material (PCM) in low temperature cool storage. Energy Conversion and Management. 2012;64:199-205.

[154] Wang B. Gold-ionic liquid nanofluids with preferably tribological properties and thermal conductivity. Nanoscale Research Letter.Volume 6:10.

[155] Ma W, Yang F, Shi J, Wang F, Zhang Z, Wang S. Silicone based nanofluids containing functionalized graphene nanosheets. Colloids and Surfaces A: Physicochemical and Engineering Aspects. 2013;431:120-6.

[156] Wang B, Wang X, Lou W, Hao J. Thermal conductivity and rheological properties of graphite/oil nanofluids. Colloids and Surfaces A: Physicochemical and Engineering Aspects. 2012;414:125-31.

[157] Zhang GH, Zhao CY. Thermal property investigation of aqueous suspensions of microencapsulated phase change material and carbon

nanotubes as a novel heat transfer fluid. Renewable Energy. 2013;60:433-8.

[158] Taheri Y, Ziapour BM, Alimardani K. Study of an efficient compact solar water heater. Energy Conversion and Management. 2013;70:187-93.

[159] Adeyanju AA. Economic analaysis of combined packed bed energy storage and solar collector system. International Journal of Renewable Energy Research. 2013;3:922-7.

[160] Ziada MA, Abdel Rehim ZS. Thermal analysis of energy storage in packed beds of multilayer storing medium. Energy Sources. 1998;20:209-22.

[161] Steinfeld A, Sanders S, Palumbo R. DESIGN ASPECTS OF SOLAR THERMOCHEMICAL ENGINEERING—A CASE STUDY: TWO-STEP WATER-SPLITTING CYCLE USING THE Fe3O4/FeO REDOX SYSTEM. Solar Energy. 1999;65:43-53.

[162] Abanades S, Villafan-Vidales HI. CO2 and H2O conversion to solar fuels via two-step solar thermochemical looping using iron oxide redox pair. Chemical Engineering Journal. 2011;175:368-75.

[163] Xiao L, Wu S-Y, Li Y-R. Advances in solar hydrogen production via two-step water-splitting thermochemical cycles based on metal redox reactions. Renewable Energy. 2012;41:1-12.

[164] Pielichowska K, Pielichowski K. Phase change materials for thermal energy storage. Progress in Materials Science. 2014;65:67-123.

[165] Mehling H CL. Heat and cold storage with PCM. Springer; 2008.

[166] Sharma S.D., Kitano H., Sagara K. Phase change materials for low temperature solar thermal applications. Res Rep Fac Eng Mie Univ. 2004;29:31-64.

[167] Farid MM, Khudhair AM, Razack SAK, Al-Hallaj S. A review on phase change energy storage: materials and applications. Energy Conversion and Management. 2004;45:1597-615.

[168] Lane G. solar heat storage - latent storage materials. Boca Raton, FL CRC Press, Inc 1983.Vol. I.

[169] Seitz M, Cetin P, Eck M. Thermal Storage Concept for Solar Thermal Power Plants with Direct Steam Generation. Energy Procedia. 2014;49:993-1002.

[170] Coscia K, Elliott T, Mohapatra S, Oztekin A, Neti S. Binary and Ternary Nitrate Solar Heat Transfer Fluids. Journal of Solar Energy Engineering. 2013;135:021011-.

[171] Raade JW, Padowitz D. Development of Molten Salt Heat Transfer Fluid With Low Melting Point and High Thermal Stability. Journal of Solar Energy Engineering. 2011;133:031013-.

[172] Gheribi AE, Torres JA, Chartrand P. Recommended values for the thermal conductivity of molten salts between the melting and boiling points. Solar Energy Materials and Solar Cells. 2014;126:11-25.

[173] Foong CW, Hustad JE, Løvseth J, Nydal OJ. Numerical study of a high temperature latent heat storage (200° - 300°) using eutectic nitrate

salt of sodium nitrate and potassium nitrate. Excerpt from the proceedings of the COMSOL users conference 2010 Paris2010.

[174] Gao D, Deng T. Materials and processes for energy: communicating current research and technological developments. In: Méndez-Vilas A, editor. Energy storage: Preparations and physicochemical properties of solid-liquid Phase change materials for thermal energy storage: Formatex; 2013.

[175] Gomez JC, Calvet N, Starace AK, Glatzmaier GC. Ca(NO3)2—NaNO3—KNO3 Molten Salt Mixtures for Direct Thermal Energy Storage Systems in Parabolic Trough Plants. Journal of Solar Energy Engineering. 2013;135:021016-.

[176] Cordaro JG, Rubin NC, Bradshaw RW. Multicomponent Molten Salt Mixtures Based on Nitrate/Nitrite Anions. Journal of Solar Energy Engineering. 2011;133:011014-.

[177] Olivares RI, Chen C, Wright S. The Thermal Stability of Molten Lithium–Sodium–Potassium Carbonate and the Influence of Additives on the Melting Point. Journal of Solar Energy Engineering. 2012;134:041002-.

[178] Ren N, Wu Y-t, Ma C-f, Sang L-x. Preparation and thermal properties of quaternary mixed nitrate with low melting point. Solar Energy Materials and Solar Cells. 2014;127:6-13.

[179] Huang Z, Gao X, Xu T, Fang Y, Zhang Z. Thermal property measurement and heat storage analysis of LiNO3/KCl – expanded

graphite composite phase change material. Applied Energy. 2014;115:265-71.

[180] Wang T, Mantha D, Reddy RG. Novel low melting point quaternary eutectic system for solar thermal energy storage. Applied Energy. 2013;102:1422-9.

[181] Zhao CY, Wu ZG. Thermal property characterization of a low melting-temperature ternary nitrate salt mixture for thermal energy storage systems. Solar Energy Materials and Solar Cells. 2011;95:3341-6.

[182] Jo B, Banerjee D. Enhanced specific heat capacity of molten salt-based nanomaterials: Effects of nanoparticle dispersion and solvent material. Acta Materialia. 2014;75:80-91.

[183] Shin D, Banerjee D. Enhancement of specific heat capacity of high-temperature silica-nanofluids synthesized in alkali chloride salt eutectics for solar thermal-energy storage applications. International Journal of Heat and Mass Transfer. 2011;54:1064-70.

[184] Wang B-X, Zhou L-P, Peng X-F. Surface and Size Effects on the Specific Heat Capacity of Nanoparticles. Int J Thermophys. 2006;27:139-51.

[185] Wang L, Tan Z, Meng S, Liang D, Li G. Enhancement of Molar Heat Capacity of Nanostructured Al2O3. Journal of Nanoparticle Research. 2001;3:483-7.

[186] Lai C-C, Chang W-C, Hu W-L, Wang ZM, Lu M-C, Chueh Y-L. A solar-thermal energy harvesting scheme: enhanced heat capacity of molten

HITEC salt mixed with Sn/SiOx core-shell nanoparticles. Nanoscale. 2014;6:4555-9.

[187] Ho MX, Pan C. Optimal concentration of alumina nanoparticles in molten Hitec salt to maximize its specific heat capacity. International Journal of Heat and Mass Transfer. 2014;70:174-84.

[188] Tiznobaik H, Shin D. Enhanced specific heat capacity of high-temperature molten salt-based nanofluids. International Journal of Heat and Mass Transfer. 2013;57:542-8.

[189] Dudda B, Shin D. Effect of nanoparticle dispersion on specific heat capacity of a binary nitrate salt eutectic for concentrated solar power applications. International Journal of Thermal Sciences. 2013;69:37-42.

[190] Andreu-Cabedo P, Mondragon R, Hernandez L, Martinez-Cuenca R, Cabedo L, Julia JE. Increment of specific heat capacity of solar salt with SiO(2) nanoparticles. Nanoscale Res Lett. 2014;9:582-.

[191] Chieruzzi M, Cerritelli GF, Miliozzi A, Kenny JM. Effect of nanoparticles on heat capacity of nanofluids based on molten salts as PCM for thermal energy storage. Nanoscale Res Lett. 2013;8:448-.

[192] Khanafer K, Tavakkoli F, Vafai K, AlAmiri A. A critical investigation of the anomalous behavior of molten salt-based nanofluids. International Communications in Heat and Mass Transfer. 2015;69:51-8.

[193] Zhou S-Q, Ni R. Measurement of the specific heat capacity of water-based Al2O3 nanofluid. Applied Physics Letters. 2008;92:093123.

[194] Zhou L-P, Wang B-X, Peng X-F, Du X-Z, Yang Y-P. On the Specific Heat Capacity of CuO Nanofluid. Advances in Mechanical Engineering. 2010;2.

[195] Aybar HŞ, Sharifpur M, Azizian MR, Mehrabi M, Meyer JP. A review of thermal conductivity models for nanofluids. Heat Transfer Engineering. 2015;36:1085-110.

[196] Keblinski P, Phillpot SR, Choi SUS, Eastman JA. Mechanisms of heat flow in suspensions of nano-sized particles (nanofluids). International Journal of Heat and Mass Transfer. 2002;45:855-63.

[197] Maxwell, J.C. A Treatise on Electricity and Magnetism: Clarendon Press, Oxford; 1873.

[198] Sundar LS, Sharma KV, Naik MT, Singh MK. Empirical and theoretical correlations on viscosity of nanofluids: A review. Renewable and Sustainable Energy Reviews. 2013;25:670-86.

[199] Einstein A. Eine neuw Bestimmung der Molekuldimensionen, Ann. Phys. 19 (1906) 289-306; English translation in Investigation on the Theory of Brownian Motion, Dover, New York, 1956.

[200] Soleimani Dorcheh A, Durham RN, Galetz MC. Corrosion behavior of stainless and low-chromium steels and IN625 in molten nitrate salts at 600 °C. Solar Energy Materials and Solar Cells. 2016;144:109-16.

[201] Subari F, Maksom HF, Zawawi A. Corrosion Behavior of Eutectic Molten Salt solution on Stainless Steel 316L. Procedia - Social and Behavioral Sciences. 2015;195:2699-708.

[202] Kruizenga A, Gill D. Corrosion of Iron Stainless Steels in Molten Nitrate Salt. Energy Procedia. 2014;49:878-87.

[203] Federsel K, Wortmann J, Ladenberger M. High-temperature and Corrosion Behavior of Nitrate Nitrite Molten Salt Mixtures Regarding their Application in Concentrating Solar Power Plants. Energy Procedia. 2015;69:618-25.

[204] Vajjha RS, Das DK. A review and analysis on influence of temperature and concentration of nanofluids on thermophysical properties, heat transfer and pumping power. International Journal of Heat and Mass Transfer. 2012;55:4063-78.

[205] Jung S. Numerical and Experimental Investigation of Inorganic Nanomaterials for Thermal Energy Storage (TES) and Concentrated Solar Power (CSP) Applications [Doctoral dissertation]: Texas A&M University; 2012.

[206] Mahbubul IM, Saidur R, Amalina MA. Latest developments on the viscosity of nanofluids. International Journal of Heat and Mass Transfer. 2012;55:874-85.

[207] Raade J, Elkin B. Thermal energy storage with molten salt. Google Patents; 2013.

[208] Ghadimi A, Metselaar IH. The influence of surfactant and ultrasonic processing on improvement of stability, thermal conductivity and viscosity of titania nanofluid. Experimental Thermal and Fluid Science. 2013;51:1-9.

[209] Norwitz G, Chasan DE. Application of Infrared Spectroscopy to the Analysis of Inorganic Nitrates. Test report T68-7-1. 1968;Quality Assurance Directorate, Frankford Arsenal, Philadelphia.

[210] ASTM D130-12, Standard Test Method for Corrosiveness to Copper from Petroleum Products by Copper Strip Test, ASTM International, West Conshohocken, PA, 2012.

[211] Heo Y, Bratescu MA, Aburaya D, Saito N. A phonon thermodynamics approach of gold nanofluids synthesized in solution plasma. Applied Physics Letters. 2014;104:111902.

[212] Angayarkanni SA, Sunny V, Philip J. Effect of Nanoparticle Size, Morphology and Concentration on Specific Heat Capacity and Thermal Conductivity of Nanofluids. Journal of Nanofluids. 2015;4:302-9.

[213] Jang SP, Choi SUS. Role of Brownian motion in the enhanced thermal conductivity of nanofluids. Applied Physics Letters. 2004;84:4316-8.

[214] Shtein M, Nadiv R, Buzaglo M, Kahil K, Regev O. Thermally Conductive Graphene-Polymer Composites: Size, Percolation, and Synergy Effects. Chemistry of Materials. 2015;27:2100-6.

[215] Khanafer K, Vafai K. A critical synthesis of thermophysical characteristics of nanofluids. International Journal of Heat and Mass Transfer. 2011;54:4410-28.

[216] Mehrali M, Sadeghinezhad E, Latibari ST, Kazi SN, Mehrali M, Zubir MNBM, et al. Investigation of thermal conductivity and rheological

properties of nanofluids containing graphene nanoplatelets. Nanoscale Res Lett. 2014;9:1-12.

[217] Mortazavi F, Banerjee D. Review of Molten Salt Nanofluids. 2016:V001T03A11.

[218] Yang Y, Oztekin A, Neti S, Mohapatra S. Particle agglomeration and properties of nanofluids. Journal of Nanoparticle Research. 2012;14:852.

[219] Myers Jr PD, Alam TE, Kamal R, Goswami DY, Stefanakos E. Nitrate salts doped with CuO nanoparticles for thermal energy storage with improved heat transfer. Applied Energy. 2016;165:225-33.

[220] Ruiz ML, Lick ID, Ponzi MI, Rodriguez-Castellón E, Jiménez-López A, Ponzi EN. Combustion of diesel soot in NO/O2 presence. Cesium nitrate and gold catalysts. Applied Catalysis A: General. 2011;392:45-56.

[221] Renganayaki V. Effect of potassium nitrate on the optical and structural properties of L-Histidine Acetate single crystals. International Journal of ChemTech Research. 2011;3:1454-61.

[222] Sulaiman M, Dzulkarnain NA, Rahman AA, Mohamed NS. Sol–gel synthesis and characterization of LiNO3–Al2O3 composite solid electrolyte. Solid State Sciences. 2012;14:127-32.

[223] Song YC, Eom HJ, Jung HJ, Malek MA, Kim HK, Geng H, et al. Investigation of aged Asian dust particles by the combined use of

quantitative ED-EPMA and ATR-FTIR imaging. Atmos Chem Phys. 2013;13:3463-80.

[224] Xiao J, Huang J, Zhu P, Wang C, Li X. Preparation, characterization and thermal properties of binary nitrate salts/expanded graphite as composite phase change material. Thermochimica Acta. 2014;587:52-8.

[225] Smirnov P, Yamagami M, Wakita H, Yamaguchi T. An X-ray diffraction study on concentrated aqueous calcium nitrate solutions at subzero temperatures. Journal of Molecular Liquids. 1997;73:305-16.

[226] Soibam I, Nilima N, Phanjoubam S. Dielectric Studies of Double Sintered Lithium Zinc Nickel Ferrite Prepared by Citrate Precursor Method. American Journal of Materials Science and Engineering. 2014;2:24-7.

[227] Ostreng E, Vajeeston P, Nilsen O, Fjellvag H. Atomic layer deposition of lithium nitride and carbonate using lithium silylamide. RSC Advances. 2012;2:6315-22.

[228] SUN Liang-Wei LX-L, TANG Cong-Ming. Comparative Study on Catalytic Performance of the Production of 2,3-Pentanedione from Lactic Acid Condensation over SiO₂-Supported Alkali Metal Nitrates. Acta Phys -Chim Sin. 2016;32:2327-36.

[229] Veerapandian M, Subbiah R, Lim G-S, Park S-H, Yun K, Lee M-H. Copper-Glucosamine Microcubes: Synthesis, Characterization, and C-Reactive Protein Detection. Langmuir. 2011;27:8934-42.

[230] Teo C-H, Zhu Y, Gao X, Wee AT-S, Sow C-H. Field emission from hybrid CuO and CuCO3 nanosystems. Solid State Communications. 2008;145:241-5.

[231] Vyazovkin S, Clawson JS, Wight CA. Thermal Dissociation Kinetics of Solid and Liquid Ammonium Nitrate. Chemistry of Materials. 2001;13:960-6.

[232] Gimenez P, Fereres S. Effect of Heating Rates and Composition on the Thermal Decomposition of Nitrate Based Molten Salts. Energy Procedia. 2015;69:654-62.